Department of Physics and Astronomy
Heidelberg University

Master thesis in Physics
submitted by

Jakob Henrichs

born in Monschau

2021

Development of a Pulse Shape Analysis for the CONUS Experiment

This master thesis has been carried out by

Jakob Henrichs

at the

Max-Planck-Institut für Kernphysik

at

Heidelberg University

under the supervision of

Prof. Dr. Dr. h.c. Manfred Lindner

Dr. Aurélie Bonhomme

Development of a Pulse Shape Analysis for the CONUS Experiment

Jakob Henrichs

Abstract

The CONUS experiment, using four 1 kg-sized point-contact high-purity germanium detectors (HPGe), aims to detect coherent elastic neutrino-nucleus scattering (CEνNS) in the fully coherent regime. It is located close to the reactor core of the nuclear power plant in Brokdorf, Germany. For the success of the experiment excellent background suppression is crucial. A new opportunity for further background reduction is the analysis of the pulse shape of each event. Depending on whether the incoming particle interacts in the fully depleted bulk region or in an outer layer of the Ge diode, the resulting pulse shapes are different. In this thesis, a technique will be presented to discriminate the different low energy interactions based on a rise time fit of their pulses. It will be shown that the rise time fit analysis can be used down to energies of $\sim$ 200 eV and that an additional background reduction of about 25 % in the region of interest for CEνNS is achievable. For this purpose, a new method will be presented to calculate the efficiencies of a pulse shape cut, including systematic uncertainties. The universality of the rise time fit is shown by demonstrating the feasibility of discriminating multi-site events at high energies.

Zusammenfassung

Das CONUS Experiment nutzt vier 1 kg große Punktkontaktdetektoren aus hochreinem Germanium (HPGe), mit dem Ziel zum ersten Mal kohärente elastische Neutrino-Kern-Streuung (CEνNS) im voll kohärenten Bereich zu messen. Aufgebaut ist CONUS in der Nähe des Reaktorkerns des Kernkraftwerks Brokdorf, Deutschland. Für den Erfolg des Experiments ist eine hervorragende Hintergrundunterdrückung entscheidend. Die Analyse der Pulsformen jedes Ereignisses bietet die neue Möglichkeit einer weiteren Reduktion des Hintergrundes. Abhängig von der Interaktionsposition der einfallenden Teilchen in der Ge-Diode, werden verschiedene Pulsformen erzeugt. Unterschieden wird zwischen Interaktionen in dem völlig verarmten Hauptteil oder in einer äußeren Schicht der Diode. In dieser Arbeit wird eine Analyse präsentiert, welche es erlaubt, die verschiedene niederenergetischen Interaktionen zu trennen. Dazu wird die Anstiegszeit der Pulse gefittet. Es wird gezeigt, dass diese Methode bis zu Energien von $\sim$ 200 eV funktioniert und in dem für die CEνNS Analyse wichtigem Energiebereich eine zusätzliche Reduktion von ca. 25% ermöglicht. Zusätzlich wird eine neue Methode präsentiert, welche es ermöglicht, die Effizienz einschließlich der systematischen Unsicherheiten einer Trennung der Pulsformen zu berechnen. Die Allgemeingültigkeit der Anstiegszeitmethode wird gezeigt, indem die Möglichkeit der Unterscheidung von Ereignissen mit mehreren Energiedepositionen bei hohen Energien demonstriert wird.

Contents

Chapter 1.

Introduction

The neutrino is the only fermion in the standard model (SM) with an electromagnetic charge equal to zero. It can only interact via the weak interaction and its mass is orders of magnitude smaller than the lepton masses [57]. Pauli first proposed the existence of the neutrino in 1930 to explain the energy conservation in the β-decay [48]. After the postulation by Pauli, it took 26 years until the electron-antineutrino was first detected by the Reines and Cowan experiment at a nuclear power plant in 1956 [32]. In 1998, neutrino oscillation was first detected by the Super-Kamiokande experiment [35] and confirmed by the measurements conducted with the SNO experiment in 2002 [3]. As a result of the oscillations, it is known that the neutrino has a non zero mass, in contrast to the SM, which predicts the neutrino as a massless particle. Therefore, neutrinos provide up to now the only solid evidence for physics beyond the standard model (BSM) [7]. Some of the most important questions regarding the properties of the neutrinos are the mass ordering, the absolute mass scale and whether neutrinos are Dirac or Majorana particles [7]. Due to the small cross-section of the interaction with matter, massive detectors are used to measure the properties of the neutrinos. As an example, the Super-Kamiokande detector has a fiducial volume of 22.5 kilotons [35]. In 1974, D. Freedman predicted the existence of a neutrino-nucleus interaction, the coherent elastic neutrino-nucleus scattering (CEνNS) [34]. Due to the coherency of the interaction, the cross-section is orders of magnitudes larger than the one from the other neutrino interactions used for neutrino detection, allowing to build more compact detectors [19]. Detectors aiming to measure this interaction can have a target mass in the kg range. Expected signals however are very small, in the keV range typically. Therefore, the interaction eluded detection for more than 40 years until the COHERENT Collaboration achieved the first detection at a Neutron Spallation Source in 2017 [4]. The CEνNS interaction allows to probe BSM physics [30] and measure SM parameters, like the Weinberg angle, at low energies [44, 45]. Several experiments are currently working towards a first detection in the fully coherent regime at a nuclear power plant [5, 13, 15, 27–29, 31, 51, 54].

The CONUS experiment is one of the experiments working at a nuclear power plant aiming at the first detection of CEνNS in the fully coherent regime. CONUS uses four 1 kg high-purity (HP) germanium (Ge) detectors, enclosed in an elaborated shielding. The experiment is located only at 17.1 m from the reactor core and profits from an electron antineutrino flux of $2.3 \cdot 10^{13}\,\mathrm{s}^{-1}\mathrm{cm}^{-2}$ [19]. In general, to achieve a detection, three main experimental challenges need to be overcome: a strong neutrino source, a low energy threshold and a low background [39]. Up to now, the CONUS experiment was able to set the best current limit for the CEνNS interaction with Ge [17]. However, to achieve the goal of a detection, the experiment's sensitivity must be increased. With the new DAQ

system installed at the experimental site for RUN-5 (begin: May 2021), improvements in terms of the noise threshold are expected. More importantly, the new data acquisition (DAQ) system allows the recording of pulse shapes. Using the pulse shape, a further background reduction is possible through pulse shape discrimination (PSD). In general, PSD can be applied because events occurring in the active volume of the detector have a different pulse shape compared to events occurring in the so-called transition layer [19]. The transition layer is an outer layer of Ge diode, where the charge collection efficiency is below 100% [38]. Background events occur in the active volume and the transition layer, while for the neutrino events, it can be assumed that they only appear in the active volume. As a result, cutting away events produced in the transition layer will allow for additional background reduction, while leaving the neutrino signals untouched. Other experiments working with Ge detectors already showed that a PSD is possible [1, 50]. The goal of this thesis is to develop a pulse shape analysis for the CONUS experiment from the beginning. The PSD analysis can be used to suppress the background further and thus tackle one of the three experimental challenges. In addition, it will help to better understand the creation of the signals and thus help to better understand the behaviour of the detector.
In this thesis, a PSD analysis to distinguish between events created in the transition layer or active volume will be developed. To differentiate between the different events, a function will be fitted to each pulse and one of the fit parameters will be used as a discrimination variable. The analysis will be implemented such that it can be used by the collaboration in the analysis chain. Additionally, a new method will be developed to calculate the PSD-cut efficiencies, including the systematics uncertainties.
The thesis is structured as follows: First, all foundations needed for the understanding of the PSD analysis are presented (chapter 2). Then, the used methods will be introduced (chapter 3), including a detailed analysis of the fit function and tests of different fit functions and methods for PSD. Afterwards, the main results are presented, including an example cut applied to reactor-ON data of the CONUS experiment (chapter 4). Also, the chapter will include a description of the method developed to calculate the cut efficiencies. In the end, the results are summarised, discussed and an outlook into future work is given (chapter 5).

Chapter 2.

Foundations

In this chapter, the foundations for this master thesis will be presented. First, coherent elastic neutrino-nucleus scattering (CEνNS) will be explained (section 2.1) and the CONUS experiment will be introduced (section 2.2). The CONUS experiment aims to measure this interaction at a nuclear power plant. Afterwards, the functionality of the used high-purity (HP) germanium (Ge) detectors will be described (section 2.3). In the end, the different possible types of signals occurring in the Ge detectors will be introduced and the way on which the signals are related to the experiment's background will be explained (section 2.4).

2.1. Coherent Elastic Neutrino-Nucleus Scattering

Coherent elastic neutrino-nucleus scattering (CEνNS) is a standard model (SM) interaction, which was first predicted in 1974 by D. Freedman [34] and was measured for the first time in 2017 by the COHERENT collaboration [4]. It is a flavour-blind neutral current interaction of a neutrino scattering off a nucleus as a whole by the exchange of a Z-boson.

$$\nu + N_{\mathrm{A}} \rightarrow \nu + N_{\mathrm{A}} \tag{2.1}$$

where ν is the neutrino and N_{A} is the target nucleus with the atomic mass A. Due to the coherency of the interaction, the corresponding cross-section is orders of magnitude larger than for other neutrino interactions, like the inverse beta decay (see Fig. 2.1). Even though the cross-section is larger than for other neutrino interactions, the detection is very challenging due to the small recoil energy of the nucleus, which is the only observable quantity [45]. The increase of the cross-section comes from the coherency of the interaction, which depends on the neutrino energy. For the coherency condition to be fulfilled, the wavelength of the momentum exchange (Z-boson) needs to be larger than the size of the nucleus. In terms of neutrino energy E_ν, this translates to the following condition [49]:

$$E_\nu \leq \frac{1}{2R_{\mathrm{A}}} \approx \frac{197}{2.5\sqrt[3]{A}}[\mathrm{MeV}], \tag{2.2}$$

with R_{A} being the radius of the nucleus. For for a Ge target, the interaction is fully coherent for neutrino energies below 20 MeV. If the neutrino energy is larger, the cross-section (see eq. 2.3) is suppressed by the form factor $F(Q^2)$. The form factor is a function of the momentum transfer Q and describes whether the target nucleus is seen as a point-like or extended object. For energies inside the fully coherent regime, the form factor is

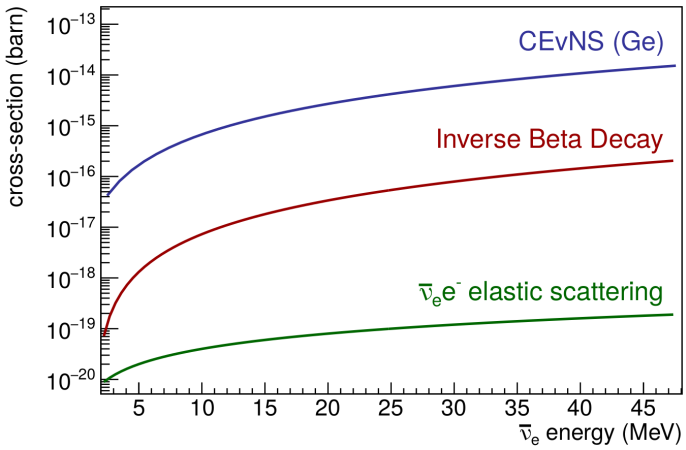

Figure 2.1.: Comparison of the CEνNS cross-section for Ge to the elastic electron antineutrino-electron scattering and the inverse beta decay channel as a function of the neutrino energy. Plot by A. Bonhomme

equal to one and for larger energies, it decreases [17, 45].
The differential cross-section of CEνNS is shown below [39]:

$$\frac{\mathrm{d}\sigma}{\mathrm{d}\Omega} = \frac{G_f^2}{16\pi^2}\left(N - \left(1 - 4\sin^2\theta_\mathrm{W}\right)Z\right)^2 E_\nu^2\,(1+\cos\theta)\,F^2(Q^2) \tag{2.3}$$

with G_f being the Fermi constant, θ_W the Weinberg angle and θ the scattering angle. The cross-section is proportional to the neutrino energy squared E_ν^2 as well as to the neutron number squared ($\sigma \propto E_\nu^2 N^2$). The first proportionality comes from the coherence of the scattering [39] and the latter comes due to the value of the Weinberg angle at low energy, which is approximately $\sin^2\theta_\mathrm{W} \approx 1/4$ [57].
A wide range of interesting physics can be probed and investigated via the detection of the CEνNS interaction. In the following, some examples are listed. A possibility to test the SM, besides measuring the existence of CEνNS, is to determine the Weinberg angle via the measurement of the CEνNS cross-section. The Weinberg angle is a fundamental parameter of the electroweak theory and CEνNS allows measuring this value at a low momentum transfer [44, 45]. A possibility to test physics beyond the standard model (BSM) is to look at the neutrino magnetic moment. If a finite value different from zero is found for a neutrino magnetic moment, this would indicate the existence of new physics [12]. A neutrino magnetic moment would influence the spectral shape of the CEνNS signal and can therefore be measured via this channel [44]. Moreover, new non-standard neutrino quark interactions or new neutral current interactions would change the predicted number of CEνNS events, allowing to probe these BSM models [30, 45]. Due to the form factor appearing in the cross-section, CEνNS also offers the opportunity to investigate the structure of the target nucleus [6]. This can be done by comparing measurements of the cross-section in the fully coherent and incoherent regime. Furthermore, CEνNS is interesting for direct detection dark matter (DM) experiments, like XENONnT. Direct

detection experiments will soon become sensitive enough to measure the so-called neutrino floor. The neutrino floor is an unavoidable background of solar neutrinos, atmospheric neutrinos and neutrinos from the diffuse supernova background, undergoing CEνNS in the DM detectors. Since the CEνNS interaction is producing the same experimental signature inside the detector as potential DM (a nuclear recoil), it is important to know this process precisely [16]. In addition, the knowledge gained by CEνNS experiments can be applied to astrophysical models. For example, during a stellar collapse, about 99% of the energy is released in neutrinos, which perform CEνNS while propagating outwards [39]. Last, a more technical advantage of CEνNS is that due to the larger cross-section, smaller and thus more practical neutrino detectors can be built. Such detectors could be used to monitor nuclear power plants at a large distance from the reactor [39]. The examples above clearly illustrate that it is of large interest to further investigate the CEνNS interaction and measure it with high precision.

Looking at the cross-section (see eq. 2.3), a heavy nucleus with a high neutron number seems favourable for the detection of CEνNS. However, the maximum of the observable quantity, the energy of the nuclear recoil, is inversely proportional to the mass of the nucleus. Therefore, from this point of view, a light nucleus is favoured. The maximal recoil energy T_{max} of the struck nucleus corresponds to a neutrino, reflected by the nucleus and can be calculated with the following formula [30]:

$$T_{\mathrm{max}} = \frac{2E_\nu^2}{m_{\mathrm{nuc}} + 2E_\nu}, \tag{2.4}$$

with m_{nuc} being the mass of the nucleus. From both considerations, cross-section and recoil energy, one finds that nuclei with medium masses are ideal for CEνNS detection. One example for such a nucleus is germanium (Ge) with a proton number of $Z = 32$ and a neutron number of $N = 38 - 42$ [39].

Considering a neutrino with an energy of 10 MeV hitting a Ge target, a maximal recoil energy of $T_{\mathrm{max}} \approx 3$ keV is expected. The recoiling nucleus frees charges inside the Ge detector, which are collected and allow for an energy measurement in the standard HPGe detectors operated at liquid nitrogen temperature. However, only a fraction of the energy is converted into ionisation. Some of the other parts are transformed into phonons and can not be measured by standard HPGe detectors, such as used by the CONUS experiment. This process is called quenching effect and can be described by the quenching factor Q, which is the ratio of the observed ionisation energy E_{ee} and the total deposited nuclear recoil energy E_{nr} [39]. Assuming a quenching factor of Q=0.2 [39], the measurable ionisation energy E_{ee} from a 10 MeV neutrino is $E_{\mathrm{ee}} = 600$ eV. This illustrates, that a very low energy threshold is necessary to be able to measure CEνNS in the fully coherent regime.

Neutrino sources and experimental challenges

The two most promising sources for experiments trying to measure CEνNS are:

1. π decay at rest (π-DAR) sources
2. nuclear reactors

The first type of source was used by the COHERENT collaboration for the first detection of CEνNS in 2017 [4]. COHERENT is located at the Spallation Neutron Source in Oak Ridge (USA), where protons are shot at a mercury target. In the collision, fast neutrons and pions are created. The pions can decay into three neutrinos: $\nu_\mu, \bar{\nu}_\mu, \nu_e$, which have energies of around 30 MeV. Due to the higher energies of the neutrinos, the scattering is not completely in the fully coherent regime [39].
In nuclear power plants $\bar{\nu}_e$ are produced in the β^--decay of the fission products, created in the nuclear fission chain reaction. Per fission, an average of 7.2 $\bar{\nu}_e$ are produced and around $\sim 3 \cdot 10^{19}$ fissions happen per second per GW_{th} (thermal power) [39], leading to an immense flux of neutrinos. The energy of the neutrinos is below 10 MeV, allowing for a detection of CEνNS in the fully coherent regime [30]. Up to this day, no experiment has been able to measure CEνNS at a nuclear power plant. Nevertheless, several experiments are operating or planning to operate at a nuclear power plant with the goal of the first detection in this energy range [5, 13, 15, 27–29, 31, 51, 54]. The CONUS experiment introduced in section 2.2 is one of those experiments and is currently holding the best limit for the detection of CEνNS with a Ge detector at a nuclear power plant [17].
The usage of different neutrino sources to measure CEνNS is complementary [30] and can e.g. help to measure the nuclear form factor.
Three key requirements need to be achieved to detect CEνNS. **First**, a very low energy threshold is necessary. As shown before, the ionisation energy, which can be measured in Ge resulting from a 10 MeV neutrino is very small. **Second**, a high flux of neutrinos is required to gather enough statistics with small compact detectors. **Third**, a stable and low background level is necessary [39]. These three points are visualized in Fig. 2.2.

2.2. The CONUS Experiment

The COherent elastic Neutrino-nUcleus Scattering (CONUS) experiment is a reactor neutrino experiment, aiming at the detection of CEνNS with Ge in the fully coherent regime. It is carried out by the Max-Planck-Institut für Kernphysik (MPIK) in Heidelberg and the Nuclear Power plant in Brokdorf (KBR), Germany. The commercial nuclear power plant, in which the experiment is located, is operated by the Preussen Elektra GmbH [37]. The experimental site is within the containment sphere of the nuclear power plant and can be entered at all times, also during the regular operation of the nuclear

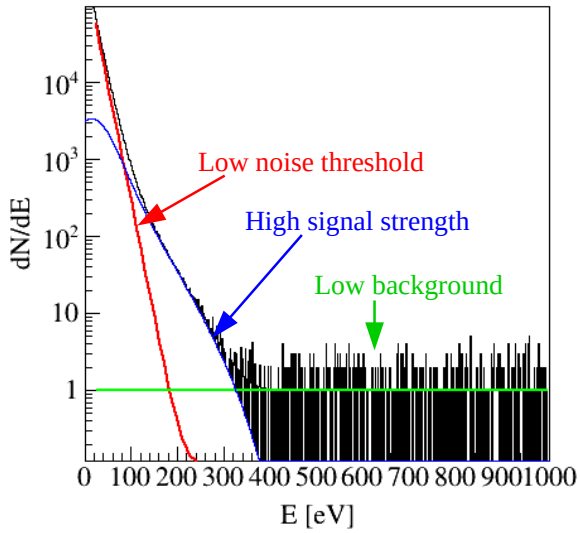

Figure 2.2.: Visualization of the three key experimental challenges needed to be overcome in order to measure CEνNS. The three challenges are: low threshold, strong neutrino source (high signal strength) and low background. Plot by W. Maneschg.

reactor. A schematic overview of the power plant, including the location of the experiment can be found in Fig. 2.3. Due to the short distance of 17.1 m from the reactor core center and the maximum thermal power of 3.9 GW_{th}, a $\bar{\nu}_e$-flux of $2.3 \cdot 10^{13}$ $cm^{-2}\,s^{-1}$ is available at the experimental site [17]. In addition, the experiment is located directly below the spent-fuel-storage-pool and therefore an overburden to shield against cosmic rays of $10 - 45$ m w.e.[1], depending on the azimuth angle is achieved [17]. The reactor has a high duty cycle, as well as a regular outage of up to a month per year, allowing for the collection of reactor-OFF data (non-reactor correlated background) [19]. In December of 2021, the nuclear power plant will be decommissioned, which will allow for a sufficiently long reactor-OFF data measurement [30]. The conditions at the reactor site are by no means laboratory conditions, making the site a challenging environment to operate an experiment in. Examples of difficult conditions are changes in the environmental conditions, no remote control access, and strict earthquake safety requirements for the experimental setups. Also, due to safety reasons, no cryogenic liquids are allowed at the experimental site. Therefore, the Ge detectors are cooled using electric cryocoolers. CONUS uses four 1 kg point contact (PC) high-purity (HP) Ge detectors with an energy threshold $E < 300$ eV_{ee}[2] and an excellent pulser resolution < 85 eV_{ee} [19]. Considering the dead layer of the detectors, a total fiducial volume of 3.73 kg can be calculated [17]. The four detectors employed in the experiment are named CONUS-1 to CONUS-4 and will be denoted in the following as C1 to C4. In addition to the four detectors, an additional detector CONUS-5 (C5) is available

[1] w.e. is the abbreviation for water equivalent.
[2] The notation for the unit is a convention to differ between nuclear recoil keV_{nr} and ionisation keV_{ee} energy.

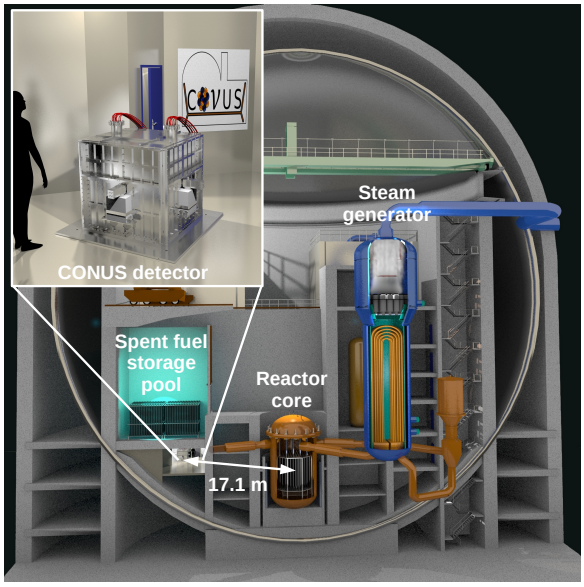

Figure 2.3.: Schematic view of the nuclear power plant (KBR) and the position of the CONUS experiment. Courtesy of construction office of MPIK.

at the Low-Level Laboratory (LLL) (overburden: 15 m w.e. [19]) of the MPIK to conduct research and development. The detector is similar to C1-C4 and has a performance that is not significantly worse, but it had a longer exposure to cosmic rays above ground [19]. Before installing the CONUS experiment on-site, a measurement campaign to investigate the reactor-correlated neutron background was carried out. The campaign started in December 2016 and was performed in cooperation with the Physikalisch-Technische Bundesanstalt (PTB). Afterwards, in the second half of 2017, the CONUS experimental setup was assembled and tested at the LLL. In the beginning of 2018, the experiment was set up at the reactor site, which took $\sim$ 4 weeks and in the subsequent 2 month, the experiment was commissioned. Data collection started in April 2018 with an outage of the power plant. Later in 2018, a dedicated campaign to measure the external γ-rays, which are partly correlated to the reactor power, was conducted [39].
Since the start of data-collection optimizations were possible, for example, a more stable temperature condition through an AC unit and a tent, which encloses the detector (cold house) is achieved [19]. In addition, for RUN-5 the DAQ system was upgraded for all four detectors. Now, the V1782 germanium module built by CAEN is used [26]. The new DAQ system is capable of recording the pulse shape of each event, allowing for pulse shape studies. That was not possible with the previously used system.

Background suppression: As explained in the previous section, one of the key requirements to be able to measure CEνNS is to have a low and well-understood background. To suppress the different types of background at the experimental site, the CONUS experiment has an elaborated shield. This shield is inspired by the GIOVE detector, which is a material screening detector at LLL [41] and has an onion-like design. In Fig. 2.4, the

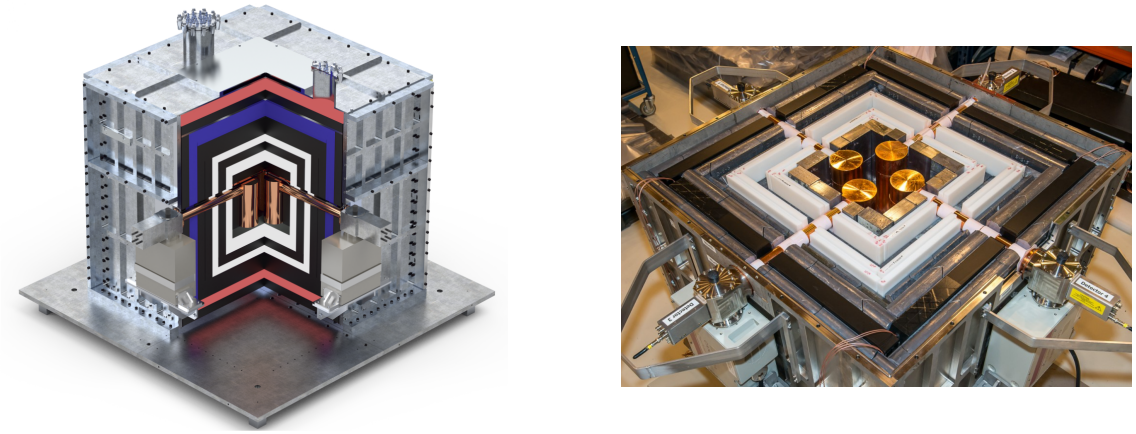

Figure 2.4.: The left figure shows the configuration of the CONUS shield. The silver outside layer is steel, the black layers are lead, the red layers are PE, the white layers are borated PE and the blue layer is the active muon veto. The four detectors are inside the Cu cryostats in the middle of the shield and are connected to the cryocooler (outside) via Cu cool fingers. Courtesy by construction office of MPIK. The photo on the right shows a picture of the half-opened CONUS shield. Courtesy of Ralf Lackner (MPIK).

structure of the CONUS shield can be seen, as well as a picture of the experiment with a half-opened shield and employed germanium detectors. The complete shield has a volume of 1.65 m^3 and weights 11 tons [17]. Therefore, the experiment is extremely compact. The shield consists of a 25 cm thick layer of lead to shield the environmental γ ray background. The innermost lead layer has a very high radiopurity to avoid radioactive decays inside the lead close to the detectors. Moreover, the shield includes layers of borated polyethylene (PE) (10 cm) and on the top and bottom, an additional layer of PE (5 cm) is added. The borated and non borated PE can moderate and capture neutrons. The neutrons mainly come from μ interactions inside the lead shielding and the surrounding concrete. Since the experiment is operated at shallow depth, a high flux of cosmic muons is present. To suppress the muon background, an active muon veto is included in the shielding. The muon veto consists of organic plastic scintillators equipped with photomultiplier tubes (PMTs). Additionally, these organic plastic scintillators work as a moderator for neutrons. In the middle of the shield, the chamber for the detectors C1-C4 is located. The complete shielding is included in a steel cage, which is constantly flushed with air to mitigate radon. The air used for flushing comes from breathing air bottles, which are stored long enough at the KBR, such that the radon can decay. In general, and especially close to the Ge diodes, only materials with a high radiopurity were used to avoid contaminations. More information about the shielding can be found in [38, 39]. The shield without the muon veto is called passive shield, while the shield with the muon veto is called active shield.
As mentioned before, in order to get good knowledge about the reactor-correlated background components, dedicated measurements were performed. The knowledge is very important because the correlated background only appears if the reactor is running and is correlated

to the thermal power, the same as CEνNS signals would be. One of the reactor-correlated backgrounds are neutrons, which are produced in the fission reactions inside the reactor core. Similar to the potential CEνNS signal, these neutrons can produce nuclear recoils inside the Ge. The second reactor-correlated background are γ-rays from the decays of N_{16}, produced by neutrons inside the cooling water of the reactor core. Therefore, this isotope can be transported through the cooling pipe system relatively close to the experimental site. In both measurements, it was found that the remaining reactor-correlated background inside the shield is negligible compared to the overall background [38].
Another background is the cosmic activation of the Ge and the copper (Cu). These materials can be activated through spallation by the hadronic part of cosmic showers at the earth's surface. The cosmic showers are created by particles (mostly protons) from e.g. the sun or extragalactic sources hitting the upper atmosphere. In this process, electromagnetic and hadronic showers are created. The produced isotopes inside the Ge or Cu have half-lives of several years and therefore, can be a problematic background during the lifetime of a CEνNS experiment. To shield this hadronic component at least $\sim$ 10 m w.e. of overburden are necessary, which is fulfilled at the CONUS experimental site [39]. In order to minimize the activation during the production process, the materials were stored underground as much as possible. In total, the Ge only was activated for 98 d and the Cu for 102 d. Additionally, the activation history is precisely documented, which allows for a calculation of the activity at any time [19].
In total, a background rate of the order of 10 counts $\mathrm{day}^{-1}\,\mathrm{kg}^{-1}$ in the sub-$\mathrm{keV}_{\mathrm{ee}}$ [19] range is achieved. The background is modelled by a Monte-Carlo (MC) simulation and is well understood. In addition, measurements showed that it is stable [19, 39]. All in all, a reduction factor of the background without and with the shield of 10^4 is achieved. A background spectrum without, with the passive shield and with the active shield can be found in Fig. 2.5. A more detailed description of the experimental setup and the background suppression can be found in [19, 39].
The pulse shape discrimination technique presented in this work provides the possibility for a further background reduction.

First results: In February 2021, the first spectral fit result of the CONUS experiment was published in a peer-reviewed journal. For the analysis, a total of 248.7 kg $\cdot$ d reactor-ON and 54.8 kg $\cdot$ d reactor-OFF data from RUN-1 and RUN-2 was used [17]. With this data set a 90%-confidence level (C.L.) limit for the CEνNS (SM) interaction as a function of the quenching parameter k was determined. The result is shown in Fig. 2.6. The parameter k comes from the modified Lindhard theory, which describes the energy dependence of the quenching factor and roughly corresponds to the quenching factor at 1 $\mathrm{keV}_{\mathrm{nr}}$ [17]. It was decided to calculate the limit as a function of the k-parameter because the quenching effect has the largest influence on the amplitude of the expected CEνNS signal above a given energy threshold, and the value at low energies was not well known. Therefore, the CONUS collaboration conducted a dedicated measurement to determine the quenching

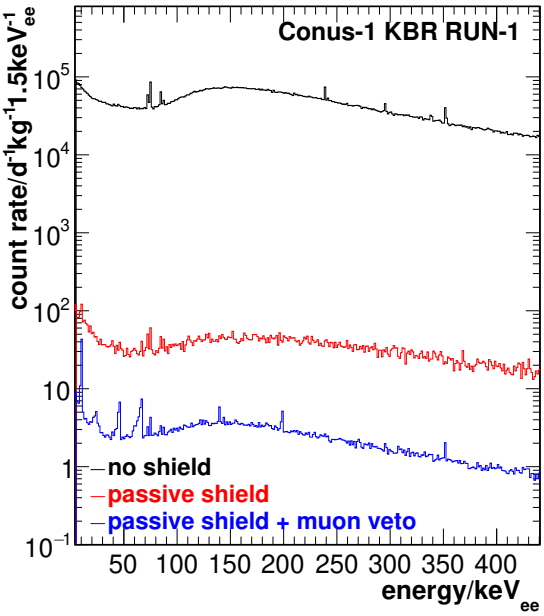

Figure 2.5.: CONUS Background spectrum without any shield (black), with the passive shield (red) and the active shield (blue). Plot is taken from [18]

.

factor for Ge. The first results give a k parameter of $k = 0.164 \pm 0.004$ [20] and they were presented in September 2021. Using this k parameter value, a limit for the CEνNS rate of < 0.4 cts/kg/d can be determined [20]. This limit is a factor of 17 away from the predicted standard model value. Currently, this is the best limit for CEνNS in the fully coherent regime obtained from an experiment at a reactor site [17].

2.3. Germanium Detectors

In this section, germanium detectors will be introduced. First, it is explained how germanium detectors work (section 2.3.1). Afterwards, it is discussed how a signal is generated and processed (section 2.3.2).

2.3.1. Functionality of a Germanium Detector

For the CONUS experiment, low threshold p-type point-contact (PPC) high-purity (HP) germanium (Ge) detectors are employed [19]. These detectors are semiconductors and allow for a measurement of electric charges ionized by particle interactions inside the Ge crystal. In the following, the basic principle of semiconductor detectors will be explained. A more detailed discussion of semiconductors for the application in spectrometry can be found in [36].
Regarding their conductivity, solids can be separated into three categories: isolators,

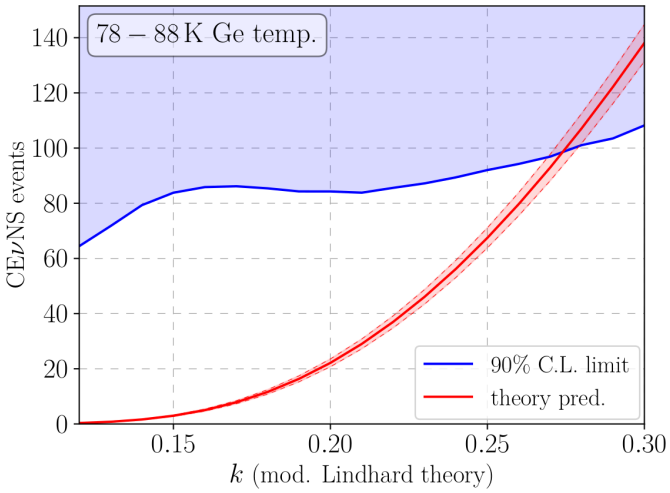

Figure 2.6.: Limits for CEνNS from the CONUS experiment as a function of the quenching parameter k. From this measurement, a quenching parameter of $k > 0.27$ can be excluded. The figure is taken from [17].

semiconductors and metals. They differ in the structure of the energy bands. The energy bands are formed from the energy levels of the single atoms inside a solid. Each energy band can only be populated by a certain number of electrons. The fully populated energy band with the highest energy is called the valence band. In order to move through the material, electrons have to jump from the valence band into the next higher energy band with free occupancy. This band is called the conduction band. If an electron is excited into the conduction band, it creates a hole in the valence band. The hole can move through the material and can be seen as a 'positive charge carrier'. Both the electron and the hole contribute to the conductivity of the material. Between the energy bands are forbidden regions for the electrons, called band gaps. The size of the band gaps are different for the three types of solids [36].

For an isolator, the band gap is of the order of $E_g \approx 10$ eV [36], meaning that the energy from thermal excitation is not enough to raise an electron from the valence to the conduction band. Therefore, no current will flow if an electric field is applied to the material [36]. In the case of a metal, the valence band is not fully populated, resulting in a continuous connection of the valence and conduction band. That means no band gap exists and the electrons can easily be thermally excited into the conduction band, leading to a good conductivity of the material [36]. For a semiconductor, the valence band is fully populated, but the energy of the band gap is smaller than for an isolator. For example, Ge has a band gap of $E_g = 0.67$ eV at a temperature of $T = 77$ K [39], which is achievable for thermal excitations of the electrons into the conduction band [36].

The number of free charge carriers in a semiconductor can be increased by doping. In this process, single atoms from different elements are implemented into the crystal. If the implemented element has a valence electron more than the semiconductor material, the additional electron will be accessible as a free charge carrier after the atom is integrated

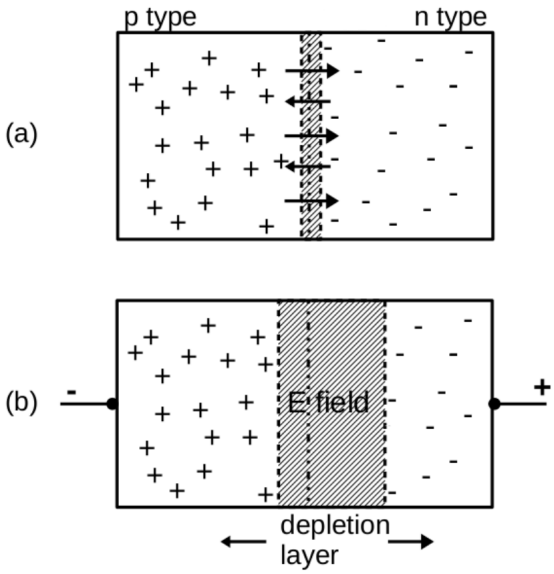

Figure 2.7.: In figure (a) a pn-junction without external voltage is shown and in figure (b) a pn-junction with external voltage applied in reverse bias is shown. Plot taken from [39].

into the crystal structure. These atoms are called donor atoms and the resulting semiconductor is a n-type material. For Ge, lithium (Li) can be used as donor atom [39]. If an element with one valence electron less is introduced into the crystal, a hole is formed. Such atoms are called acceptors and the resulting semiconductor is a p-type material. For Ge, boron (B) can be used as an acceptor [39]. If the concentration of acceptor or donor atoms is very high, the different types of semiconductors are called p+ and n+, respectively. Due to natural impurities, Ge semiconductors can be categorized into p- and n-type materials [36].

To be able to use a semiconductor as a particle detector, a high voltage (HV) needs to be applied to collect the free charges created in an interaction. Applying a high voltage to the Ge semiconductor will result in a current called leakage current. That makes the intrinsic semiconductor unsuitable to use as a detector. However, a detector can be built by creating a pn-junction. For a pn-junction, a n-type and p-type semiconductor are brought into contact. Through diffusion, some excess holes from the p-type material may diffuse into the n-type material and some excess electrons from the n-type material diffuse into the p-type material. Through this process, recombination of excess charge carriers happens, forming at the interface a region without free charge carriers, called the depletion region. The region can be extended by applying a high voltage in reverse bias [36]. A schematic view of a pn-junction can be seen in Fig. 2.7. Charge carriers created in this depleted region through interactions are collected by the cathode and anode. The depletion region is the active part of the detector and the HV is chosen such that this region extends over the whole Ge volume. In conclusion, the pn-junction reduces the leakage current and thus makes a suitable ionisation detector [36].

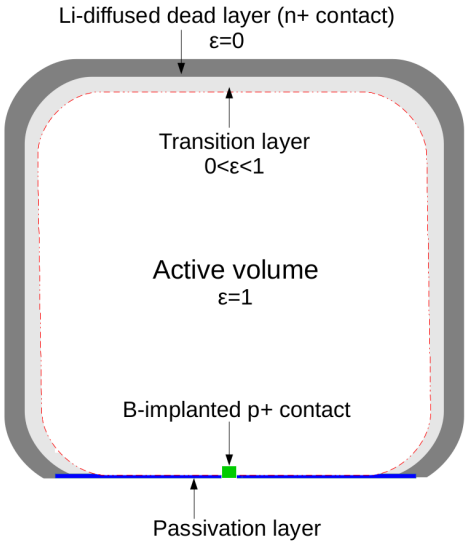

Figure 2.8.: Schematic view of a PPC HPGe detector as used in the CONUS experiment. The dead layer has a thickness of the order of 1 mm, the transition layer of the order of 0.2 mm and the passivation layer of the order of 100 nm [39]. The HV is applied between the p+ and n+ contact. Plot taken from [19].

Using Ge as a semiconductor detector for high-resolution spectroscopy is ideal due to the available intrinsic high purity material. A high purity material allows to fully deplete the detector with a HV that can be provided realistically and it minimizes the risk of charge trapping. Thus a high charge collection efficiency can be achieved. Moreover, the energy needed to create electron-hole pairs inside Ge is small. That leads to a large number of free charge carriers per interaction and a better energy resolution. Due to the small band gap, the Ge detectors are normally operated at temperatures around 77 K (liquid nitrogen temperature, normally used for cooling) to reduce the leakage current due to thermal excitation [39].

For the CONUS detectors, a p-type point contact configuration is used. A schematic view of such a detector can be seen in Fig. 2.8. The n+ contact is on the outside of the p-type material, forming the bulk part of the detector, except for the bottom side. On the bottom side, the point-like p+ contact (used for readout) is located. The p+ contact is made by B implantation and has only a diameter of a few millimetres. Between the p+ and n+ contact is the so-called passivation layer as isolation between the two contacts [19]. The n+ layer is created by Li diffusion and has a thickness of the order of 1 mm [39]. On the contrary, the passivation layer has a thickness of the order of 100 nm [39]. The outer layer of the detector, the n+ contact, is called ”dead layer”. The dead layer has a charge collection efficiency of $\epsilon = 0$ and therefore, interactions inside this layer are not seen by the detector. In contrast, the active volume (fully depleted region) has a charge collection efficiency of $\epsilon = 1$. In between these two parts of the detector is the ’transition layer’. This layer has a charge collection efficiency of $0 < \epsilon < 1$ and increases gradually from 0 at the dead layer to 1 at the active volume. The transition layer is created due to the diffusion of

lithium atoms from the dead layer into the active volume and has a thickness of the order 0.2 mm [39]. If an interaction happens in this layer, the resulting pulse looks different from the active volume events. These pulses are called 'slow pulses' and are explained in more detail in section 2.4.2.
The complete Ge diode is enclosed in a vacuum cryostat, connected via a cooling finger to an electric cryocooler, able to cool down the diode to liquid nitrogen temperatures [19].

2.3.2. Signal Creation and Processing

This section describes the process from creating a signal inside the Ge detector until its processing in the data acquisition (DAQ) system.

Signal creation: In the interaction of a particle with the detector, energy is deposited inside the Ge crystal. If the deposited energy is large enough, an electron can be moved from the valence band into the conduction band, leaving behind a hole in the valence band. The number of electron-hole pairs N_{eh} created in an interaction can be calculated with the average energy needed to create an electron-hole pair ϵ [36]:

$$N_{\text{eh}} = \frac{E_{\text{dep}}}{\epsilon}, \tag{2.5}$$

with the deposited energy E_{DEP}. It means that the created charge in this interaction is proportional to the deposited energy. For Ge, the average energy needed for electron-hole creation is $\epsilon = 2.96$ eV at a temperature of 77 K [36]. Without the presence of an electric field, the electrons in the conduction band will de-excite and recombine with the hole in the valence band. However, if an electric field is present, the holes and electrons will drift towards the p+ and n+ electrodes of the diode, respectively. The drift of the charge carriers induces a charge at the electrode, which can be measured. If the charge carriers reach the electrodes, they do not further contribute to the signal [22]. To understand the structure of the resulting pulse, we need to understand the time development of the induced charge. The induced charge Q and induced current I created by a moving charge q at a certain time t can be calculated with the Shockley-Ramo theorem [40]:

$$Q(t) = -qW\left(\mathbf{x}(t)\right), \tag{2.6}$$

$$I(t) = q\mathbf{v} \cdot \mathbf{E}(\mathbf{x}(t)), \tag{2.7}$$

where $\mathbf{x}(t)$ is the trajectory of the moving charge inside the detector, $W(\mathbf{x})$ is the weighting potential, $\mathbf{v}$ is the velocity of the moving charge and $\mathbf{E}(\mathbf{x}) = -\nabla W(\mathbf{x})$ is the weighting field. The weighting potential is a dimensionless form of the electric potential, calculated by setting the considered electrode to unit potential, all other electrodes to zero potential, and removing all charges from inside the detector [40]. In the case of the PPC Ge detectors, the p+ contact is set to unit potential and the n+ contact to zero potential. The induced

charge at the readout electrode, induced by the electron (e) and hole (h) cluster is [22]:

$$Q(t) = -q^e \cdot W\left(\mathbf{x}(t)\right) - q^h \cdot W\left(\mathbf{x}(t)\right). \tag{2.8}$$

That means that the induced charge will increase until all charges are collected at the electrodes. At this time, the total induced charge is equal to the collected charge at the readout electrode (q^h). This observation can be confirmed by inserting unity for the weighting potential at the readout electrode and zero at the other electrode into eq. 2.8 [22]. Under the assumption that no charge is lost during the drift process, the total measured induced charge is directly proportional to the created charge and thus to the deposited energy. However, some charges can be lost during the drift due to impurities or defects of the crystal. There are two different mechanisms of charge loss. In the first case, electrons and holes are trapped together, leading to recombination. Such a trap is called "recombination centre". In the second case, the charge carriers are trapped until they are released through thermal excitation. This trap is called "charge traps" [22]. If charge loss appears, the collected charge is not proportional to the deposited energy anymore. Therefore, for good energy reconstruction and resolution, detectors with high purity and very few defects are necessary. For the CONUS Ge detectors, a net impurity concentration of around 10^{12} Ge atoms per impurity is achieved [39]

The charge collection time depends on the velocity of the charge carriers and the position where they are created. For low electric fields, the drift velocity depends on the electric field strength. If the electric field is increased, the drift velocity increases as well. The increase is roughly linearly until the drift velocity reaches a saturation velocity at high electric fields and becomes independent of the electric field [36]. For holes and electrons, the saturation velocity is $v \sim 10^7\ \mathrm{cm\,s^{-1}}$ and is reached at an electric field strength of $\sim 1000\ \mathrm{V\,cm^{-1}}$ [36]. In addition, also the drift direction relative to the crystal axes influences the drift velocity [22]. Under the assumption that the saturation velocity is reached and for a one-dimensional case, the charge collection time $t^{e/h}$ can be calculated as [36]:

$$t^h = x_0/v \text{ and } t^e = (x_{\mathrm{n+}} - x_0)/v, \tag{2.9}$$

where x_0 is the interaction position, $x_{\mathrm{n+}}$ is the position of the n+ contact and the position of the p+ contact is set to zero.

The charge collection times for holes (t^h) and electrons (t^e) are different and depend on the position of the interaction. Therefore, in general, the shape of the induced charge signal depends on the interaction position. For the CONUS PPC detectors, the weighting potential is sharply peaked at the readout electrode (p+ contact). In the rest of the detector, the potential is rather small. A plot of the simulated weighting potential of C1 can be seen in Fig. 2.9. Since the induced charge is proportional to the weighting potential, mainly the charges moving to areas with high potential will contribute to the signal. The

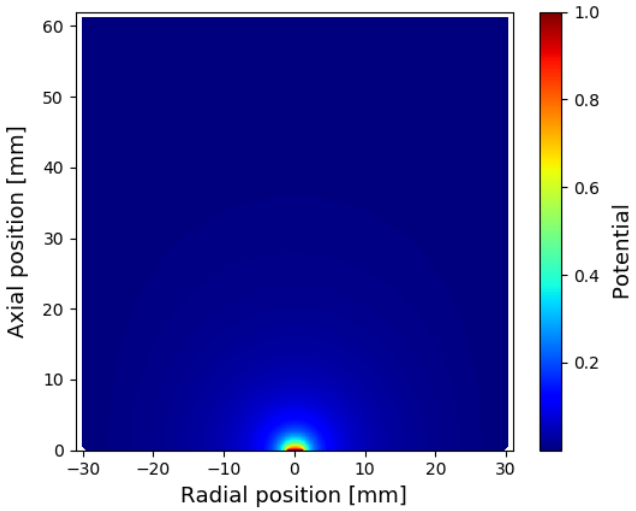

Figure 2.9.: Simulated weighting potential of the C1 detector. The plot is kindly provided by J. Hakenmüller and J. Hempfling.

created hole drifts to the p+ contact and thus will always drift through regions with a high weighting potential. The electrons drift to the n+ contact and will mostly experience a very low potential. Only if the interaction takes place close to the readout electrode, the electrons will also see the high weighting potential. In conclusion, for most of the interactions in a p-type detector (like in CONUS), the contribution from holes will be the dominant part of the signal and the electrons will contribute little to nothing. Moreover, the position dependence of the signal will be rather weak because the major part of the signal is created close to the readout point.

Signal processing: The induced charge, collected at the readout point, is transformed into a voltage by a charge sensitive preamplifier (CSP), coming directly after the detector in the electronics readout chain. A representation of the CONUS signal detection and amplification electronics chain can be found in [19]. The voltage created by the CSP is directly proportional to the induced charge and, therefore, to the deposited energy. Events are characterized by an increase relative to the lowest voltage level of the CSP, called the baseline [39]. The baseline is not flat but is characterized by noise fluctuations. In order for the CSP to continuously collect charges, the previous collected charges need to leak away. Otherwise, the CSP will reach the maximal amount of charges it can accumulate (dynamic range) and thus cannot detect further events [36]. A commonly used type of preamplifier for HPGe detectors is the resistive feedback preamplifier (RC preamplifier). Such a preamplifier has an additional resistor built in parallel to the charge collection capacitor. That allows the capacitor to discharge, resulting in an exponential decay of the pulse back to the baseline. The CONUS detectors have a transistor reset preamplifier (TRP). The TRP adds up all events coming in until the dynamic range is reached. If this is the case, a transistor reset circuit brings the voltage level back to the baseline. A

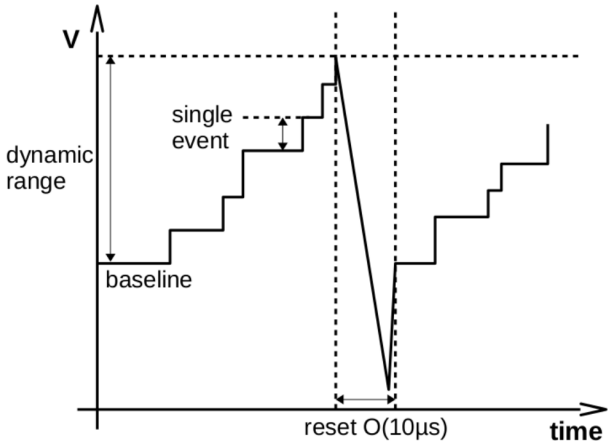

Figure 2.10.: Schematic view of the signal created by a transistor reset preamplifier (TRP). The plot is taken from [39].

schematic view of this process is shown in Fig. 2.10. During the reset, no pulses should be recorded to avoid spurious events. Therefore, the reset time will be vetoed and add up to the dead time[3] of the detector. In general, the reset takes $\mathcal{O}(10\ \mu s)$ [39], however, the TRP veto time window has been chosen to be longer (for RUN-5: $\mathcal{O}(800\ \mu s)$) to ensure that a stable baseline is recovered. Comparing both preamplifiers, the TRP has two main advantages. First, the RC preamplifier has an intrinsic noise, coming from the resistor and adding up to the overall noise budget. In contrast, the TRP does not have this noise and is therefore preferred for low threshold measurements. Secondly, the TRP does not lock up in the case of a high count rate. The RC preamplifier instead will lock up for high count rates. That will happen if the time between two pulses is so short that the first pulse does not decay far enough, such that the second pulse reaches the dynamic range [36]. For the CONUS experiment, the count rates from physical events are rather low, but high count rates are necessary to study the noise in detail [39]. To minimize thermal noise, the TRP is close to the Ge diode inside the cryostat and therefore cooled down to cryogenic temperatures [39].

After the preamplifier, the signal is feed into the DAQ, where it is amplified and the energy is extracted. For the CONUS experiment, the signal is split after the preamplifier and processed by two different DAQ systems. In the experiment's first data runs (RUN-1 to RUN-4), only one DAQ, the Canberra Lynx Digital Signal Analyzer (in the following named Lynx), was used. This DAQ system extracts the signal energy via shaping filters and gives as an output the energy and timestamp of each event [39]. For the last data run (RUN-5, begin: May 2021), an additional DAQ system, the Ge module V1782 from CAEN [26] (in the following named CAEN) is added. With this DAQ, not only the time and energy information can be extracted but also the shape of the recorded signal. That enables a pulse shape analysis. In addition to the module V1782, the module V1725 from

[3]The dead time is the time of the measurement, where no events can be recorded. That can, e.g., happen due to TRP resets.

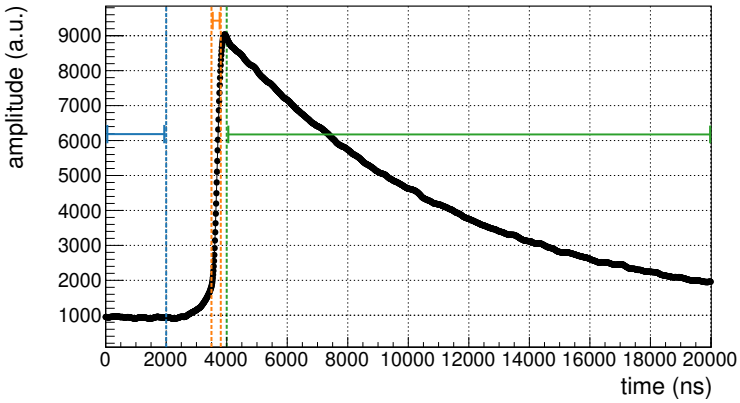

Figure 2.11.: Example pulse recorded with the CAEN and the C1 detector. The blue region marks the part of the pulse, where the baseline is visible, the rise time of the pulse is marked with orange and the green region marks the exponential decay of the pulse. The shown pulse has an energy of $E = 28.9$ keV.

CAEN [25] is added for RUN-5. The module V1725 records the timestamp of the TRP reset and of the μ-veto, allowing for an offline TRP reset veto cut and μ-veto cut. The input channels of the CAEN are AC coupled creating an exponential decay for the input signal back to the baseline. The exponential decay is created for each single event and the decay constant is determined by the electronic components of the AC filter inside the CAEN. For energy reconstruction, a shaping algorithm based on the Jordanov trapezoidal filter [42] is used. The algorithm produces a trapezoid, where the height of the flat top is proportional to the height of the input pulse and, therefore, proportional to the energy of the event. In order to extract the energy, the height of the trapezoid is measured in the flat top region and saved in ADC channels. The number of ADC channels is fixed and corresponds to the dynamic range of the DAQ. For the conversion of the energy in eV, a calibration needs to be performed, relating the channel number to an energy in eV. Changing settings of the CAEN, monitoring the data acquisition and collecting the data is done with the CoMPASS software [24]. CoMPASS enables the user to change a variety of different settings. An explanation of all the different settings is beyond the scope of this work. However, two interesting settings for recording the pulse shapes are the recorded time window Δt_{window} and the recorded time before the pulse $t_{\text{pre-trig}}$. The first setting sets the length of the time window around the pulse. As a standard, a value of $\Delta t_{\text{window}} = 20000$ ns is chosen. A discussion of different window sizes can be found in appendix A.2. Using this time window a part of the baseline, the complete increase and a major part of the exponential decay are visible. For the second setting, which sets the time recorded before the trigger, a standard value of $t_{\text{pre-trig}} = 5000$ ns is chosen. A plot of an example pulse recorded with the CAEN is shown in Fig. 2.11.

2.4. Pulse Shapes of the CONUS Detectors

In this section, characteristics and features of the pulses measured with the CONUS detectors will be discussed (section 2.4.1) and the different signal types will be classified (section 2.4.2). Afterwards, the different possible particle interactions in Ge are explained and what kind of signals they produce will be discussed (section 2.4.3). In the end, it will be explained why the pulse shape discrimination can be used in the CONUS experiment for additional background suppression (section 2.4.4).

2.4.1. Characteristics and Features

In this section, the most important characteristics of the recorded pulses are introduced. In addition, two features appearing in the recorded pulses are discussed. An example of a recorded pulse with the C1 detector can be seen in Fig. 2.11.

Rise time: The rise time is defined as the time needed for the pulse to rise from 10% to 90% of its height [36]. The quantity is energy independent because the time structure of the pulse purely depends on the electric field inside the detector through which the charges are drifting (see section 2.3.2). Instead, the deposited energy or created charge q is only a scaling factor for the pulse (see eq. 2.6). That means, with increasing energy, the rise time stays the same, but the slope of the rising edge and the amplitude of the pulse is changing. The rise time of the recorded pulse shown in Fig. 2.11 is marked in orange.

Exponential decay: In order for the next pulse to be processed correctly by the DAQ system, the exponential decay created by the AC coupling of the DAQ system brings the pulse back to the baseline. Since the decay is created by the DAQ system, the decay constant is equal for all recorded pulses. The time range where the shown pulse in Fig. 2.11 decays exponentially is marked in green.

Baseline: The baseline is the lowest voltage level coming from the preamplifier without any increase due to physics events [39]. In the recorded data, the baseline can be seen in the first few 100 ns of the pulse. The time range where the baseline of the pulse shown in Fig. 2.11 is visible is marked in blue.

Next, two features will be discussed, appearing not in all events or detectors. For investigating these features, mean pulses are used. In this work, a 'mean pulse' will always be a pulse, calculated by taking the mean of all pulses of a certain type (for example: all pulses with an energy between 29-30 keV). A plot showing different mean pulses can be found in Fig. 2.12. The plot shows three mean pulses coming from a Th-228 measurement with the C1 detector (green/red/violet). A short explanation of the most frequently used

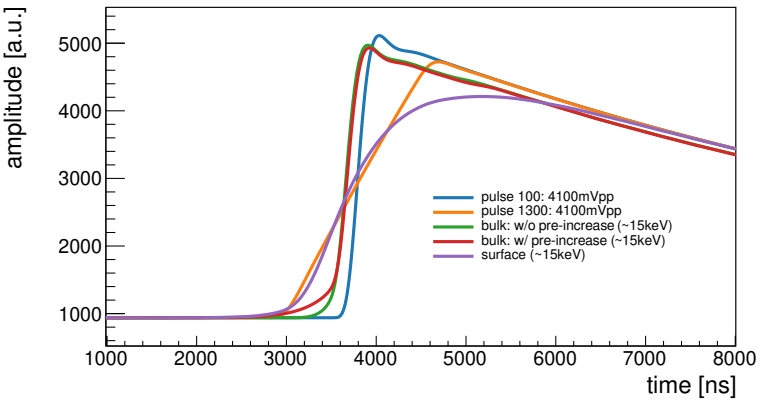

Figure 2.12.: Different mean pulses for the C1 detector. For the mean pulse 'pulse 100' ('pulse 1300') the pulser measurement with an input rise time for the pulser of 100 ns (1300 ns) was used (pulse 100: blue, pulse 1300: orange). For the other three mean pulses, physical events are used, with energies around $E \approx 15$ keV. The used populations for the calculation are the slow pulse population (violet), the normal pulse population with a pre-increase (red) and the normal pulse population without a pre-increase (green).

measurements can be found in Appendix A.1. These pulses are calculated using normal and slow pulses (the difference between normal and slow pulses will be explained in section 2.4.2), while the normal pulses are further split into two populations, showing a different behaviour in the functional form of the pulse. All three populations are obtained by applying the rise time fit to the data (the rise time fit will be explained in section 3.1.3).

Bump: At the highest point of the normal pulses, a small 'bump' is visible. The bump appears only in the detectors C1 and C4. To check if this feature comes from the electronics or the Ge diode, a measurement with a pulser was conducted. The pulser can be used to test the electronics chain independent from the Ge crystal by sending generated pulses through the electronics chain. In order to test if the bump comes from the electronics, pulses with different rise times were sent through the electronic chain and were recorded with the DAQ. The Tektronix AFG 3252 [52] was used for the measurement, operated in the *Pulse* mode. In this mode, the generated pulses have a linear increase and the rise time of the leading edge of this increase can be chosen. Two different rise times for the pulses were selected, for the measurement: 100 ns (*pulse 100*) to mimic normal pulses and 1300 ns (*pulse 1300*) to mimic slow pulses. For this measurement, the C1 detector was used. The resulting mean pulses of these measurements are also shown in Fig. 2.12. In this figure, it is visible that the pulses with a leading edge of 100 ns have the same bump as the normal pulses coming from the Ge crystal. In conclusion, the bump seen on top of the normal pulses is an effect coming from the electronics chain of the detector and not from the Ge crystal.

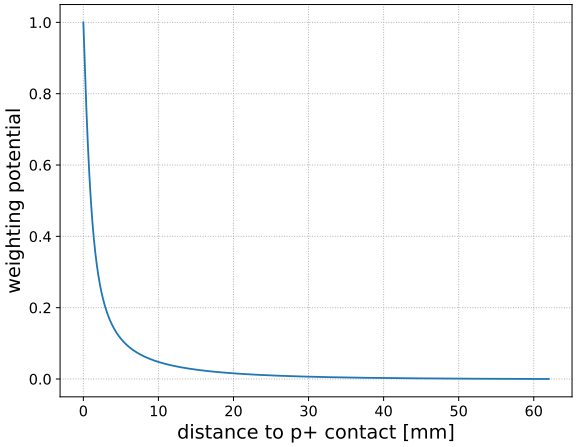

Figure 2.13.: Simulated 1D weighting potential of the C1 detector. Plot made by J. Hakenmüller and J. Hempfling

Pre-increase: The second feature can be seen by comparing the two normal pulses from Fig. 2.12. It can be seen that one of them (red) has a small increase before the main increase of the pulse (pre-increase), while the other pulse (green) stays mostly flat in this part. The feature appears in all four detectors (C1-C4). Since the normal pulse from the pulser does not show a pre-increase, we can conclude that the effect must come from the Ge crystal. The pre-increase could come from the interaction position inside the Ge diode. To investigate this possibility, a simple one-dimensional example calculation of the pulses can be performed. Equation 2.8 can be used for the calculation and a one-dimensional version of the weighting potential is needed. The weighting potential for C1 (see Fig. 2.13) is kindly provided by J. Hakenmüller and J. Hempfling and comes from an electric field simulation. The time-dependent position of the holes $x_\mathrm{h}(t)$ and electrons $x_\mathrm{e}(t)$ inside the Ge diode is calculated assuming that both charge carriers reach their saturation velocity of $v \sim 10^7\ \mathrm{cm\,s^{-1}}$ [36]

$$x_\mathrm{h}(t) = x_0 - vt \text{ and } x_\mathrm{e}(t) = x_0 + vt \tag{2.10}$$

with x_0 being the interaction position. In the calculation, the x-axis is chosen such that the p+ contact is at $x = 0$ mm. Combing all this into eq. 2.8 pulse shapes can be calculated. Figure 2.14 shows the result of these calculation with starting positions at different interaction points. The pulses are shifted in time such that the increase overlays (replicating the effect of the pre-trigger of the DAQ). All pulses are created with a charge of the charge carrier clusters equal to $|q^\mathrm{e}| = |q^\mathrm{h}| = 1$. From Fig. 2.14 we can conclude that interactions close to the p+ contact (small x_0 value) will create pulses with a weaker or close to no pre-increase, depending on their distance to the read-out contact. The interactions happening farther away from the p+ contact (larger x_0 value) will create pulses with a pre-increase, similar for different positions inside the diode.
Also, in Fig. 2.14, it can be seen that the pulses differ shortly before they reach their

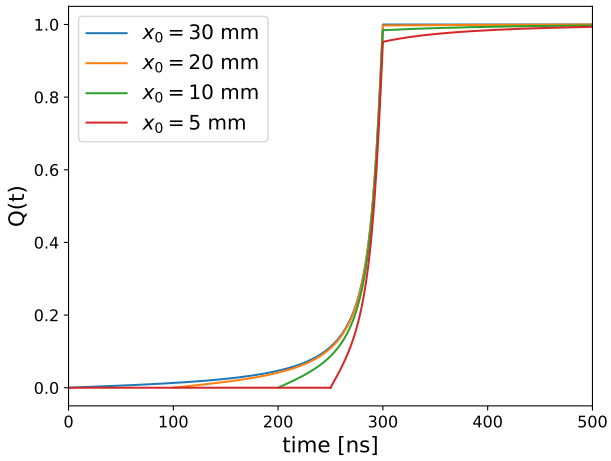

Figure 2.14.: Calculated pulses using eq. 2.8 and the weighting potential from Fig. 2.13. For the calculation, different interaction positions are chosen. The x_0 gives the interaction position, which is the distance from the p+ contact. The calculation is done in one dimension only.

maximum. Responsible for the effect is, that for events close to the p+ contact, the electrons shortly drift through an area with a high weighting potential. Therefore, the electrons will contribute to the signal as well. In contrast, for events happening further away from the contact, only the holes drift through areas of high weighting potential and contribute to the pulses.
In conclusion, we could show based on a simple simulation that this pre-increase is an effect coming from the interaction position of the event inside the Ge diode.

2.4.2. Classification

In the following, the different signal types occurring in the detector will be introduced and classified. A signal can be assigned to more than one category. For example, the single-site events are also either normal or slow pulses.

Normal pulses: Signals produced by interactions inside the active volume of the detector are categorised as normal pulses. The pulse shape can be slightly different depending on where the interaction happens in the detector, but the major part of the pulse is expected to be similar for all normal pulses. To be more precise, pulses with and without a pre-increase (see section 2.4.1) are expected. The rise time of the normal pulses is relatively short and of the order of $\mathcal{O}(200 - 300$ ns). An example of a normal pulse can be seen in Fig. 2.15 a).

Slow pulses: Interactions happening inside the transition layer of the Ge diode are called 'slow pulses'. In this case, the created holes need to diffuse out of the transition layer, before drifting towards the p+ contact. Due to this process, the rise time of the

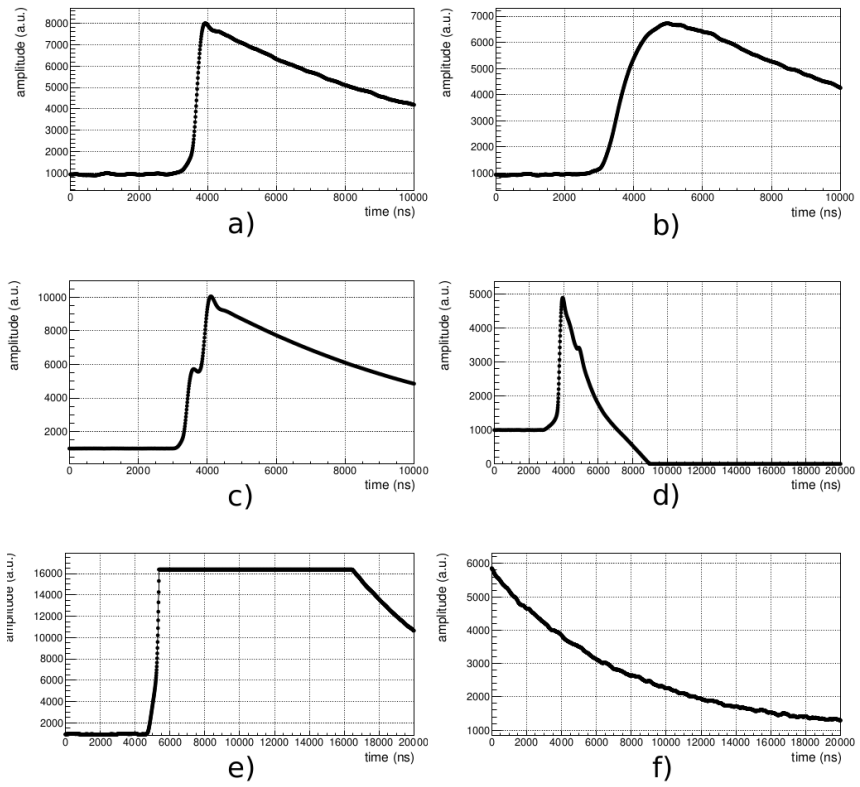

Figure 2.15.: Different signal types (section 2.4.2). The pulses are all recorded with the C1 detector. Figure a) shows a normal pulse, figure b) shows a slow pulse, figure c) shows a MSE, figure d) shows a TRP reset event, figure e) shows a saturation event and figure f) shows an exponential decay event.

pulse will be longer than for normal pulses. 'Slow' refers to the larger rise time compared to the normal pulses. In addition, the Li atoms inside the transition layer can trap charges, leading to an incomplete charge collection. Therefore, the energy of a slow pulse event is not reconstructed correctly and is smaller than the deposited energy [19, 39]. The rise time for slow pulses is of the order of $\mathcal{O}(1000 - 2000$ ns). An example of a slow pulse can be seen in Fig. 2.15 b).

Single-site events: All events where only one energy deposition is detected are classified as single-site events (SSE). That means all normal pulses and slow pulses with only one energy deposition are SSE. If the distance between two energy depositions is smaller than the spatial resolution of the detector, they will also be classified as SSE.

Multi-site events: In a multi-site event (MSE), multiple energy depositions are detected inside the detector within a single event. If the event is classified as a MSE, the distance between the two energy depositions is larger than the spatial resolution of the detector. An example of an interaction creating MSE is Compton scattering, where the same γ can scatter multiple times inside the crystal. In Fig. 2.15 c), an example for a recorded MSE is

shown. A MSE can consist of multiple normal, multiple slow pulses and from the mixture of normal and slow pulses.

Unphysical events: All events that did not arise from physical interactions or have features that make a correct energy reconstruction impossible are classified as unphysical. A first example of an unphysical event is a saturation event. In a saturation event, the voltage created by the preamplifier is larger than the dynamic range of the DAQ or preamplifier. Therefore, the system saturates and the pulse becomes artificially flat at the point of saturation. Saturation makes the energy reconstruction for the event impossible. An example of a saturation event can be seen in Fig. 2.15 e). The DAQ system can identify the majority of these events and flag them. Using the flags, it is possible to cut away most of these events. A second example are pile-up events. In the case of pile up, the time difference between two events is so short, that the energy of the second event cannot be reconstructed correctly [39]. Most of these events can also be identified by the DAQ system, such that they can be cut. Another type of unphysical signals are events happening during the TRP reset. An example of how such an event can look like is shown in Fig. 2.15 d). Due to the reset of the preamplifier, the recorded signal gets distorted, making a correct energy reconstruction impossible. Moreover, the time of the TRP reset is recorded, making it possible to cut such events. The last example are events where only the exponential decay of the pulse is visible (see Fig. 2.15 f)). In this case, it clearly makes no sense to reconstruct the energy. Overall, this kind of events need to be filtered out, otherwise, they can falsely contribute to the spectrum. A possibility to cut the events with an exponential decay is discussed in section 3.2.4 (quality cuts).

2.4.3. Sources of Different Pulse Shapes

In the following, the interactions of different particles with Ge and the resulting pulse shapes will be introduced. That is necessary to understand why pulse shape discrimination (PSD) can be employed for background reduction.

Electromagnetic radiation: In general, the intensity of incoming γ-rays follows the Beer-Lambert law when travelling through matter. The Beer-Lambert law is [36]:

$$I(x) = I_0 e^{-\mu(E)x}, \tag{2.11}$$

with $\mu(E)$ being the attenuation coefficient, E being the energy of the incoming γ-ray, x is the length over which the attenuation takes place and I_0 is the starting intensity. The value of the attenuation coefficient depends on the energy of the incoming particle. A plot of the energy dependence of the mass attenuation coefficient for γ-rays in Ge can be found in Fig. 2.16. For the conversion to the attenuation coefficient from eq. 2.11, the mass attenuation coefficient has to be multiplied by the density of the absorber material [36].

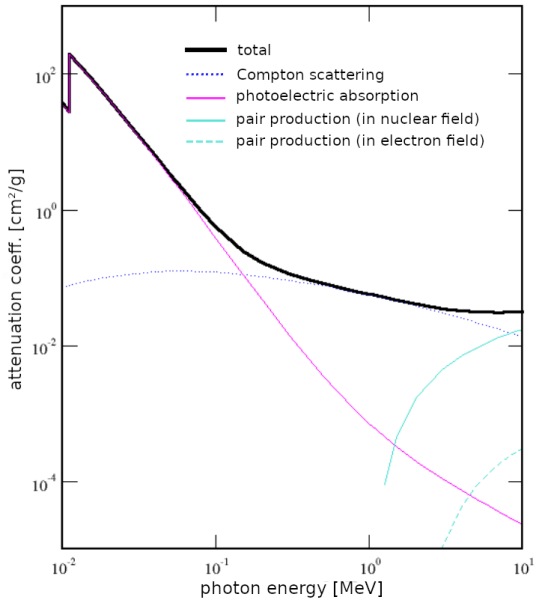

Figure 2.16.: Mass attenuation coefficient $\mu(E)$ for γ-rays in Ge. Taken from [14].

There are three main interactions of γ-rays with matter (summarized in Tab. 2.1).

Photoelectric absorption: During photoelectric absorption, the photon is absorbed by an electron in the shell of the atom. The electron is kicked out of the shell, having the energy of the photon minus the binding energy. In principle, the nucleus performs a small recoil, but the energy going into the recoil is small, such that it can be neglected for all practical reasons. The vacancy left in the electron shell is filled by an electron falling down from a higher shell. During this process, a characteristic X-ray is emitted (X-ray fluorescence). Alternatively, the energy from the electron filling the vacancy can be transferred to another electron in the shell, which leaves the atom (Auger cascade) [36]. Electrons on the K-shell are most likely to be ejected from the atom if the photon energy is high enough. Due to the fact that different electronic shells become available at different energies, it results in the characteristic form of the attenuation coefficient for photoelectric absorption. Going towards higher energies, a jump in the attenuation coefficient appears if a binding energy of the next atomic shell is reached and thus becomes available [36]. In the case of X-ray fluorescence, the ejected X-ray will undergo photoelectric absorption again until the complete energy is deposited. If the event occurs close to the surface or in a small detector, the X-ray can scatter out of the detector [36]. Overall, it can be assumed that the complete energy is deposited inside the detector and that the resulting event is a SSE. The photoelectric absorption is dominant for energies below $E \lesssim 100$ keV [14]

Compton scattering: Compton scattering is dominant for energies from 100 keV to several MeV [14]. If a γ-ray performs Compton scattering, part of its energy is transferred to an electron. The amount of transferred energy depends on the scattering angle and the γ-ray can scatter multiple times until the complete energy is deposited or until leaving the detector. Therefore, due to Compton scattering, SSE and MSE are expected. If

Table 2.1.: Summary of the different electromagnetic interactions and their resulting pulse type.

	dominant energy range	resulting pulse type
photoelectric absorption	$\lesssim 100$ keV	SSE
Compton scattering	~ 100 keV – several MeV	SSE and MSE
pair production	$\gtrsim$ several MeV	FEP: MSE SEP: MSE DEP: SSE

the complete energy is deposited inside the detector, the event contributes to the full energy peak (FEP) and if only part of the energy is deposited, it appears in the Compton continuum below the peak [36, 39].

Pair production: In this process, the incoming γ-ray creates an electron-positron pair inside the detector. The interaction can only happen in the Coulomb field of an atomic nucleus or an electron. If the interaction occurs in the vicinity of a nucleus, the energetic threshold is at least twice the electron's rest mass $E \geq 1022$ keV. For the interaction in the Coulomb field of an electron, the threshold is at least four times the electron's rest mass [36]. In both cases, the energy of the created electron and positron is half the energy of the incoming γ-ray. After the positron is slowed down in the detector material, it will recombine with an electron. During this process, two photons with an energy of $E = 511$ keV are emitted back-to-back. Since the time needed for the positron to slow down is very short ($\mathcal{O}(1$ ns$)$) relative to the charge collection time, the recombination after the pair production can be seen as immediate [36]. The two photons created during recombination can deposit their energy or escape the detector, leading to three observable peaks. First, if both photons deposit their energy inside the detector, the event contributes to the FEP. Events contributing to the FEP have a high probability of being MSE because the interaction produces a localized energy deposition from the electron and positron and at least one energy deposition from each recombination photon [22]. For events in the second peak, one of the two photons escapes the detector without scattering, resulting in an energy reduced by 511 keV relative to the FEP. The resulting peak is called single escape peak (SEP). Again, the event is with a high probability a MSE [22]. If both photons leave the detector without scattering, the event contributes to the double escape peak (DEP). The DEP is located at an energy of 1022 keV below the FEP. In contrast to the first two peaks, the DEP events have a high probability of being SSE because only the localized energy deposition of the electron and positron contributes to the pulse [22]. Pair production is the dominant interaction for energies higher than several MeV [14].

The mean free path λ of γ-rays inside Ge depends on their energy. For photons with an energy of $\mathcal{O}(1$ MeV$)$, the mean free path is several cm and for an energy of $E \approx 100$ keV, it is $\mathcal{O}(0.1$ cm$)$ [39]. From the mean free path, it can be deduced that depending on their energy, γ-rays will interact more or less in the transition layer or active volume, producing

slow and normal pulses. Since the mean free path gets smaller for lower energies, it is expected that the fraction of slow pulses increases for lower energies.

Neutrinos: There are several different possible interactions of neutrinos with matter. However, for this thesis, we will concentrate on CEνNS. If a neutrino scatters off a nucleus, the nucleus performs a small recoil. The recoil creates free charges inside the Ge, leading to a measurable pulse. Even though the cross-section of CEνNS is orders of magnitude larger than the cross-section of other neutrino interactions, it is still very small in comparison to the one of other particles. Therefore, it is expected that neutrinos only interact once in the detector and produce SSE. In addition, due to the small cross-section, it can be assumed that the neutrinos are interacting homogeneously throughout the whole detector. Together with the fact that the active volume makes up around 91-95% of the crystal, depending on the detector [19], we can assume that neutrinos are producing ***normal pulses*** (SSE) predominantly.

Neutrons: For the CONUS experiment, there are three important interactions of neutrons with matter: neutron capture, elastic and inelastic scattering. Depending on the energy of the neutron, a different interaction is dominant. At the CONUS experimental site, neutrons with energies of 10^{-9} MeV up to several MeV are present [39].
Neutron capture is dominant for energies between $10^{-9} - 4 \cdot 10^{-7}$ MeV. In the process, a neutron is absorbed by the nucleus, leaving the nucleus in an excited state. During de-excitation of the nucleus, mono-energetic γ-rays are ejected. These γ-rays can have energies up to several MeV and the ground state of the nucleus after neutron capture can be meta-stable. The decay of these meta-stable nuclei inside the Ge can be seen in the background spectrum. In principle, the nucleus performs a recoil during neutron capture, but the recoil can be neglected because of the neutrons' low energy. Additionally, the emission of the γ-rays creates a recoil of the Ge nucleus. However, taking the quenching effect (see section 2.1) into account and assuming a threshold of 300 eV, one finds that the recoils are not visible. Events from γ-rays created by the capture of μ-induced neutrons inside the detector can be cut due to the muon-veto. Furthermore, neutrons coming from the reactor are negligible inside the shield [38, 39].
Elastic scattering is dominant up to energies of $\sim$ 1 MeV and is the second possible interaction. The process leads to a recoil of the Ge nucleus. In contrast to neutrinos, the cross-section of this interaction is larger and therefore, it is assumed that the neutron scatters multiple times in the detector [39].
The last important process is the inelastic scattering of neutrons of the Ge nuclei and is dominant for energies larger than 1 MeV. Again, the process produces a recoil of the nucleus, but additional γ-rays are created. If the additional γ-rays leave the detector, the deposited energy from the recoil is large enough to contribute to the low energy part of the spectrum. In the case where the γ-rays are detected, the recoil together with the γ-ray will create a characteristic tail above the corresponding γ-ray peak [39].

All three interactions produce nuclear recoils and can mimic a CEνNS interaction. In addition, the mean free path of neutrons in Ge is large enough, such that mostly ***normal pulses*** will be expected. Therefore, it is essential to have a good understanding of the neutron background.

Electrons: Electrons with an energy of 1 MeV are stopped within a few mm in Ge and for electrons with energies of 100 keV, the mean free path is already several orders of magnitude smaller [39]. Therefore, it can be assumed that electrons deposit their total energy in the outer layers of the detector and that they will produce ***normal and slow pulses***. The energy loss happens via bremsstrahlung or ionisation [53].

α-particles: Since α-particles are shielded by the copper cryostat of the CONUS detectors, the decay needs to happen inside the cryostat for the α-particles to reach the Ge diode. A possible source of α-particles inside the cryostat is ^{210}Pb (see section 2.4.4). In the ^{210}Pb decay chain, α-particles with an energy of $E = 5.2$ MeV (outside of the possible CONUS energy range) are produced [39]. These particles are absorbed in Ge within < 20 μm [39]. Therefore, they are shielded by the dead layer of the diode ($\mathcal{O}(1$ mm$)$). However, they can penetrate the passivation layer ($\mathcal{O}(100$ nm$)$) and reach the active volume [39]. As a result, α-particles will produce ***normal pulses*** close to the p+ contact.

2.4.4. Potential Background Suppression

In section 2.4.3, it is shown that different particles will produce different kinds of signals in the detector. For CEνNS neutrinos, the assumption is that they interact homogeneously and therefore mainly produce normal pulses, while electrons and γ-rays will produce normal and slow pulses. Consequently, this means that a PSD, able to differentiate between normal and slow pulses, can cut events generated by electrons and γ-rays while neutrino events stay untouched. Therefore, a background reduction with a PSD-cut is possible in principle.
If the potential impact of a PSD-cut on the CONUS background is rewarding, depends on the physical composition of the background. In Fig. 2.17, the Monte-Carlo (MC) model of the CONUS background below $E = 14$ keV$_{\text{ee}}$ is shown. The MC model shows that the dominant background comes from the decay of ^{210}Pb and from μ-induced neutrons produced inside the shield [39]. The background coming from μ-induced neutrons cannot be suppressed by a PSD-cut because neutrons mainly produce normal pulses. However, a reduction of the background coming from the decay of ^{210}Pb is possible. The lead isotope decays via β-decay into ^{210}Bi producing β-electrons. In addition, Auger electrons and γ-rays with energies below $E < 65$ keV are emitted. ^{210}Bi also decays via β-decay [39]. To minimize background from ^{210}Pb, lead with a very high purity was used from the innermost lead shielding close to the cryostat. From this layer, only the decay of ^{210}Bi

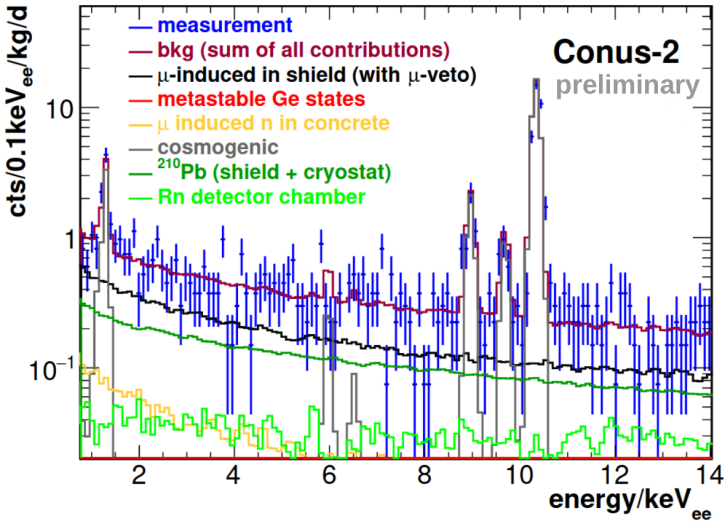

Figure 2.17.: MC model for the background of the CONUS experiment and the different dominant contributions. It can be seen that the two backgrounds contributing most come from μ-induced neutrons and from the decay of ^{210}Pb inside the shield and cryostat. Plot taken from [18].

is energetic enough to reach the detector. Instead, the decay radiation from ^{210}Pb will not reach the Ge diode. However, the 46.5 keV line from the decay of ^{210}Pb is visible in the spectra of all four detectors, implying that additional contamination with ^{210}Pb inside the cryostat is present [39]. The electrons and low energy γ-rays produced in the decay of ^{210}Pb will mostly interact in the outer layers of the diode. Therefore, they produce a non-negligible amount of slow pulses, which can be rejected by a PSD-cut.
As a result, the PSD as an additional background suppression is promising for the CONUS experiment since it has the potential to suppress one of the two dominant backgrounds.

Chapter 3.

Methods

In this chapter, different techniques to discriminate between normal and slow pulses will be introduced and discussed (section 3.1). After an overview of the different methods, a more detailed analysis of the best working method, the rise time fit, is presented (section 3.2). For the complete chapter, detector C1 is used as a benchmark detector.

3.1. Different Methods for Pulse Shape Discrimination

In this section, different methods to distinguish between normal and slow pulses are presented. First, the A/E method is explained (section 3.1.1), followed by the integral ratio method (section 3.1.3). Afterwards, the rise time fit is introduced (section 3.1.2). Moreover, a overview of the three most frequently used measurements can be found in appendix A.1.

3.1.1. A/E Method

The A/E method is based on the findings of [46] and it was shown by [8] that using these findings, a SSE and MSE discrimination is possible. The GERDA Collaboration further developed the method and applied it for background suppression [22, 23]. The idea behind this method is to compare the energy per charge cluster in the Ge diode to the total energy of the event [22]. For a SSE, the total energy E is contained in one charge cluster and the height A of the single peak of the detector current pulse is proportional to the deposited energy. In contrast, for a MSE, the energy will be distributed over several charge clusters, leading to multiple overlapping pulses and a detector current pulse with multiple peaks. The energy of each charge cluster can be calculated from the height of each peak of the detector current pulse [22]. Since for MSE, the energy is distributed over several peaks, the amplitude A of the largest peak of the detector current pulse will be smaller than for SSE. The ratio A/E is therefore smaller for MSE than for SSE and thus can be used as discriminating variable [22, 23]. A derivative of the pulse coming from the preamplifier can be used to reconstruct the detector current pulse [23]. In Fig. 3.1, a visualization of this idea is shown. For simplicity, the exponential decay of the pulses is neglected in the visualization. If the exponential decay is included, a small deformation appears in the peak of the reconstructed detector current pulse, but the conclusion stays the same. In the following, two PSD methods arising from the considerations above will be introduced.

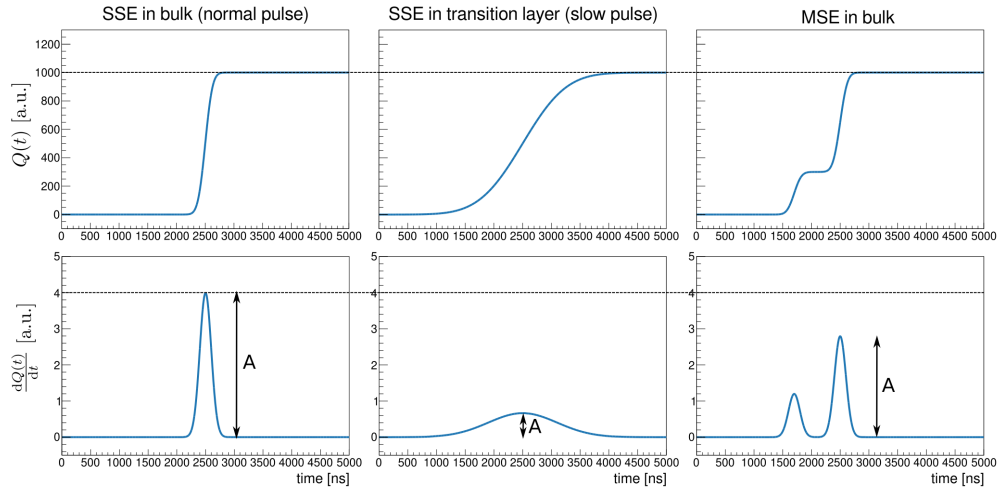

Figure 3.1.: Visualization of the A/E method and how it can be used to distinguish between SSE in the bulk ('normal pulses'), SSE in the transition layer ('slow pulses') and MSE in the bulk. The upper plots show the charge pulse and the lower plots show their derivative, i.e. current pulse. While the pulse amplitude is the same for all three pulses, the amplitude A of the derivative is the largest for the normal pulse. The plot is inspired by [22].

A/E method (amplitude based):

The GERDA Collaboration showed that this method could be used to discriminate MSE and SSE successfully [22, 23]. Moreover, Fig. 3.1 shows that the height A also varies for normal and slow pulses, making it in theory possible to use this method for slow and normal pulse discrimination.

The principle of this method can also be described qualitatively. We assume that the pulse coming from the preamplifier can be described by an error function:

$$f(t) = \frac{A_0}{2}\left[1 + \mathrm{erf}\left(\frac{t - t_0}{\sqrt{2}\tau}\right)\right], \tag{3.1}$$

with t_0 being the shift along the time axis, τ proportional to the pulses' rise time and A_0 the pulse height. If the pulse reaches its maximum, all charges created in the interaction are collected and thus, the pulse height is proportional to the energy of the event. Calculating the amplitude of the derivative of eq. 3.1, which is called A, gives the following expression:

$$A = \frac{A_0}{\sqrt{2\pi}\tau} \tag{3.2}$$

Equation 3.2 shows that if the rise time of the pulse increases, like is the case for slow pulses, the amplitude A of the derivative of the pulse decreases. This makes it possible for the A/E method to be used for discriminating normal and slow pulses.

The method was implemented and applied to CONUS data. In the following, a short explanation of the implementation is given. First, the recorded pulses are differentiated to

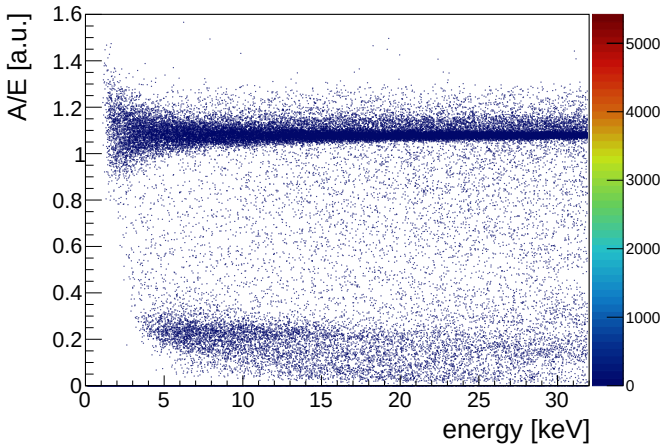

Figure 3.2.: Application of the A/E method to a Th-228 measurement conducted with the C1 detector. The colour bar indicates the number of events per bin.

reconstruct the detector current pulse. Then, a function to find all peaks of this derivative is applied and the found peaks are fitted by Gaussian functions. If no peaks are found, the fit parameters for this event will be set to zero. The resulting fit parameters of the Gaussian fit to the peak with the highest amplitude are saved and can be used to calculate the ratio A/E. A plot showing A/E vs. the energy for a Th-228 measurement with the C1 detector can be found in Fig. 3.2. For the calculation of the A/E values, the reconstructed energy in ADC channels is used. In this plot, two populations are clearly visible, one population is at a value of $A/E \approx 1$ and the second population is at a smaller A/E value ($A/E \approx 0.2$). We expect that the higher population ($A/E \approx 1$) mainly consist of normal pulses, while the lower population consist mainly of slow pulses, since slow pulses have a smaller amplitude A compared to normal pulses (compare eq. 3.2). A visual inspection of the pulses in the different populations supports this expectation. In conclusion, this means that the method could be used for slow and normal pulse discrimination.
However, in Fig. 3.2, a significant disadvantage of this method is visible: it does not work for sub-keV energies. The reason for this will be discussed later in this section.

Sigma method (rise time based):
A second sub-method of the A/E approach arising from the considerations above consists in using the width of the fitted Gaussian as the discriminating variable. The derivative of the pulse, which is assumed to be described by eq. 3.1 is:

$$f(t) = \frac{A_0}{\sqrt{2\pi}\tau} \exp\left(-\frac{(t-t_0)^2}{2\tau^2}\right) \tag{3.3}$$

If the derivative is fitted with a Gaussian distribution, the width σ will be equal to the τ parameter of the pulse and thus proportional to the rise time. As a result, the width of this peak should be smaller for normal pulses compared to slow pulses. Again, if the

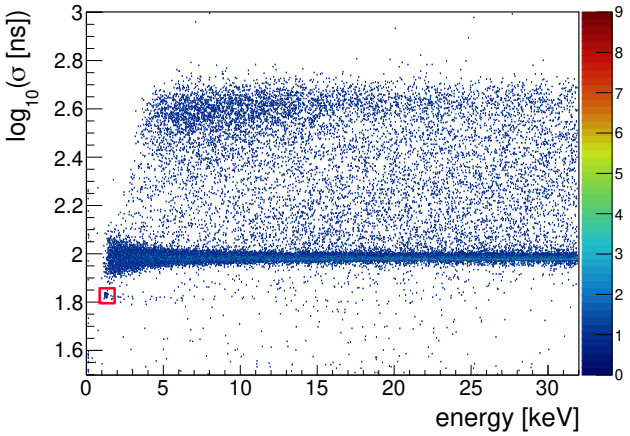

Figure 3.3.: Application of the sigma method to a Th-228 measurement conducted with the C1 detector. The small blob (marked by the red rectangle) consists purely of unphysical events. The colour bar indicates the number of events per bin. The range of the colour bar is different compared to Fig. 3.2 because the failed fits, which are saved in the 0th bin, are cut away for this plot.

exponential decay is included, the relation would change slightly, but the conclusion stays the same.

The method is similar to the rise time fit described in section 3.1.3. However, for the rise time fit, the rise time will be extracted directly from the pulse and not from its derivative. Figure 3.3 shows a plot of the width σ plotted against the energy of each event. In this figure, two main populations are visible, one at larger σ values and the second one at lower values of σ. It is expected that the lower population consists of normal pulses and the higher population consist of slow pulses. A visual inspection of the pulses in the different populations confirm this. Between the two populations, pulses with a rise time between the two populations and some slow pulses with a higher rise time are found. That the slow pulses with a higher rise time are located here is an effect of the fit routine. In the fit routine, noisy peaks are sometimes wrongly fitted by multiple peaks, leading to a smaller σ values than expected for the slow pulse. The small blob (marked by the red rectangle) visible in Fig. 3.3 consist purely of unphysical events. All in all, this method could also be used for normal and slow pulse discrimination. However, the same major disadvantage as for the A/E method is visible in Fig. 3.3.

Disadvantages:

The major disadvantage of the two methods described above is that they do not work at sub-keV energies. An explanation for this can be found for both methods by looking at eq. 3.2. Equation 3.2 shows that the amplitude of the derivative A decreases if the amplitude of the original pulse A_0 decreases. Since A_0 is proportional to the energy of the event, the amplitude A will decrease with the energy. If the amplitude is similar to the noise height, peaks are not found and the two above described methods do not work anymore.

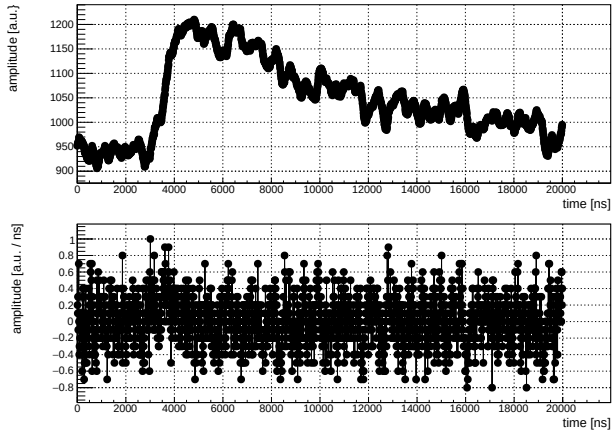

Figure 3.4.: Example pulse for an energy of $E \approx 1$ keV (top plot) and its derivative (bottom plot). This illustrates why the A/E and sigma method fails at low energies. Both methods rely on the fit of the derivative, but at small energies, the peak in the derivative cannot be distinguished from noise.

The effect happens earlier for the slow pulses than for the normal pulses because A is anti-proportional to the rise time parameter τ (see eq. 3.2). As a result, the two methods can only be used to discriminate normal and slow pulses down to energies of around $E \approx 4$ keV. Since for the CEνNS analysis of the CONUS experiment, the region of interest (ROI) is around 300 eV, these methods cannot be applied in the ROI. Therefore, these methods will not be investigated further in this work. In Fig. 3.4, an example pulse and derivative are shown for an energy $E \approx 1$ keV, where the A/E and sigma method failed. It can be seen that the pulse is still clearly visible, even if the derivative is not. This shows that a method fitting the pulse directly, as the rise time fit, potentially works at these energies.

3.1.2. Integral Ratio Method

The idea behind the method is to compare the integral over a certain region of the pulses for different events. Due to the different shapes of the normal and slow pulses, the integral should give different values if appropriate regions are chosen. In addition, the integral over the complete pulse is used as a normalization. If the beginning of the integral is the time t_A and the end of the integral is at the time t_B, the discriminating variable R can be written as:

$$R = \frac{\int_{t_\mathrm{A}}^{t_\mathrm{B}} f(t)\mathrm{d}t}{\int_{0\ \mathrm{ns}}^{20000\ \mathrm{ns}} f(t)\mathrm{d}t} \tag{3.4}$$

with $f(t)$ describing the pulse. A visualization of this method can be seen in Fig. 3.5. Since the integral A is normalized by the total area of the pulse, the values for R should be between zero and one.

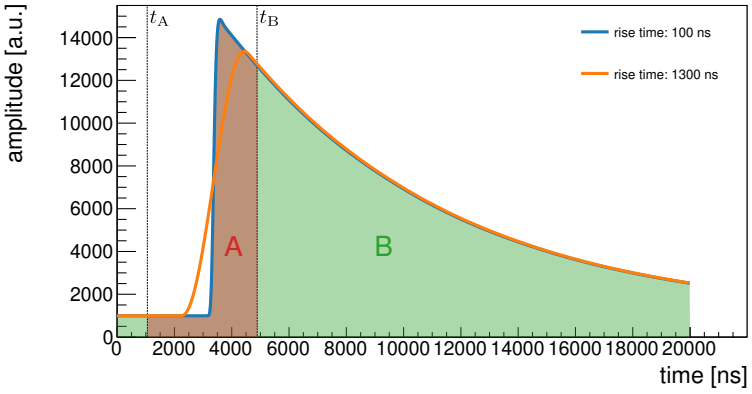

Figure 3.5.: Visualization of the integral ratio method. The blue curve is a normal pulse and the orange curve is a slow pulse of an event with the same energy, recreated with the pulser. The method is visualized with the blue curve, while the orange curve is just for comparison. The calculated ratio for the blue curve is $R = \frac{A}{B}$ and the start and endpoint of the integral A are chosen arbitrarily.

Pulser data: First, the starting point of the integral is fixed to $t_A = 0$ ns and a scan over t_B, between 1000 ns and 6000 ns, was performed. Larger times for the endpoint are not interesting because the exponential decay for normal and slow pulses is quite similar. The scan was performed for an energy of $E \approx 32$ keV and was conducted to find a value, such that the difference between the values of R for slow and normal pulses is maximal. For the scan, a pulser measurement with forced trigger[1] and with the C5 detector was used, allowing to artificially generate slow and normal pulses. The best discrimination of R was found for a value $t_B = 3370$ ns, corresponding to the crossing point of the normal and slow pulse (see Fig. 3.5). After the scan, the found value for t_B was used to apply the method to all energy points measured with C5 and the result is shown in Fig. 3.6. It can be seen that R has a discrimination power for normal and slow pulses, especially for higher energies. However, for energies below $E \simeq 5000$ ADC (~ 5.5 keV), the two populations start to mix and below $E \simeq 1000$ ADC (~ 1 keV), the two populations cannot be distinguished by eye anymore. In general, the separation of the normal and slow pulse population is for all energies not large.

Also, it is interesting that the values of R decrease with increasing energies. It is expected that the value of R is constant for all energies, assuming that the pulses scale with a global scaling factor. In the implementation of the method, the baseline is not subtracted from the pulse and thus the complete pulse cannot be scaled by a global factor. As a result, the relative contribution of the baseline increases for low energies, leading to a non-constant behaviour of R. A smaller R value for larger energies can be explained by the fact that only the first part of the pulse is used for the partial integral. If we go to higher energies, the major increase of the pulse happens after the crossing point. As a result, the integral

[1] The idea of this measurement is explained in detail in section 4.4, but the pulser was used in Pulse mode.

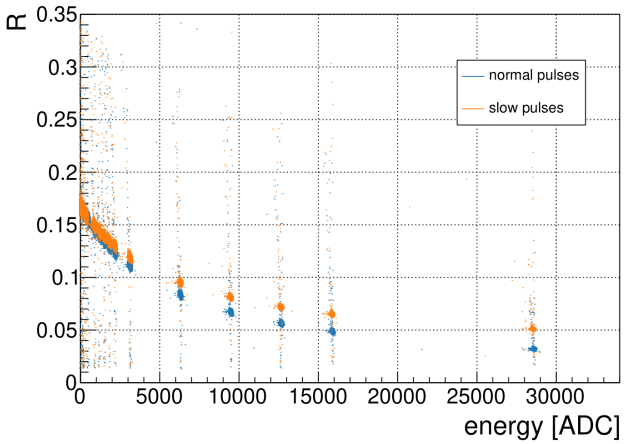

Figure 3.6.: Parameter R plotted vs. the energy of each event. The blue points are measured with a rise time for the pulser of 100 ns and the orange ones with 1300 ns. The energy range goes up to $\sim$ 39 keV.

in the numerator, only going to the crossing point, is not changing as much as the integral in the denominator, going over the whole pulse.

Reactor-ON data: Also, the method is applied to a reactor-ON data from the C1 detector before the application of the μ-veto. Before this is possible, the integral start and endpoint has been adjusted, by considering the physical mean pulses presented in Fig. 3.7. The difference between the mean normal and slow pulse is bigger for the times after the crossing point and thus, this region will be used for the calculation of R. As a result, the starting point of the integral is at $t_A = 3650$ ns (crossing point) and the endpoint is chosen to be $t_B = 6000$ ns. The integral ratio method was applied with the new parameters to reactor-ON data and the resulting plot can be found in Fig. 3.8. A main band and a population below the band is visible. The main band should consist of normal pulses, while the events below should be slow pulses. Furthermore, the number of events below the main band for high energies is compatible with the number of slow pulses found by the rise time fit (see section 3.1.3).

In contrast to the R variable in Fig. 3.6, it is visible in Fig. 3.8 that the R value gets larger for higher energies. An explanation for this is that the integral is calculated over the part of the pulses, which increases the most for higher energies. Therefore, the mean increase in this interval is higher than the mean increase over the whole pulse (for the entire pulse, also the baseline is included, which does not increase for higher energies).

The result shows that a discrimination between normal and slow pulses based on the integral ratio method can be achieved. However, the discriminating power of R is not very large, the R parameter has no physical meaning and the method can not distinguish between pulses with and without a pre-increase. In conclusion, we decided not to use this method for the CONUS analysis.

Noise rejection: Another idea for an application of this method is based on the fact that

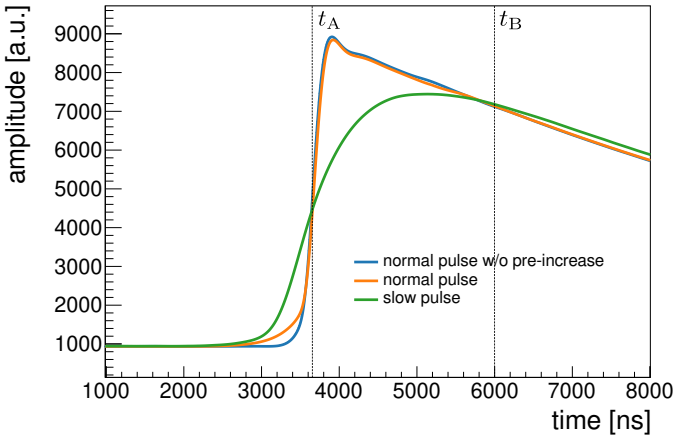

Figure 3.7.: Three mean pulses to illustrate the chosen start and endpoint of the integral ratio method for physical data. Two of them have the form of a normal pulse, one with (orange) and the other without (blue) a pre-increase. The third mean pulse shows the form of a slow pulse (green).

the R parameter has a theoretical lower limit and thus could be used for noise suppression. The lower limit can be calculated under the assumption that the noise fluctuates perfectly random around a mean value μ. With this assumption, the integral over a certain time period can be substituted by this mean value μ multiplied with the time period, leading to the following form of the R parameter for a purely noise event:

$$R_{\text{noise}}^{\text{theo}} = \frac{\mu\,(t_{\text{B}} - t_{\text{A}})}{\mu\,(\Delta T_{\text{acq}})} = \frac{(t_{\text{B}} - t_{\text{A}})}{\Delta T_{\text{acq}}}, \tag{3.5}$$

with $\Delta T_{\text{acq}} = 20000$ ns. For perfect random noise, one would expect a Gaussian distribution of R values with the mean $R_{\text{noise}}^{\text{theo}}$.
For the calculation of the R parameter, we will write the integral over a specific time interval as the mean value in this interval μ multiplied with the time interval [56]:

$$\int_{t_1}^{t_2} f(t)\mathrm{d}t = \mu\,(t_2 - t_1) \tag{3.6}$$

Using this relation, the formula of the R parameter of a pulse event is:

$$R_{\text{pulse}} = \frac{\mu_1\,(t_{\text{B}} - t_{\text{A}})}{\mu_2\,(20000\text{ ns} - 0\text{ ns})}, \tag{3.7}$$

with μ_1 and μ_2 being the mean values in the different intervals used for the calculation. The formula looks very similar to the theoretical noise value (eq. 3.5), with the difference that $\mu_1 \neq \mu_2$. Combing the formula for the R_{pulse} value and the one for the theoretical noise value, we find the following relation:

$$R_{\text{pulse}} = \frac{\mu_1}{\mu_2} R_{\text{noise}}^{\text{theo}}. \tag{3.8}$$

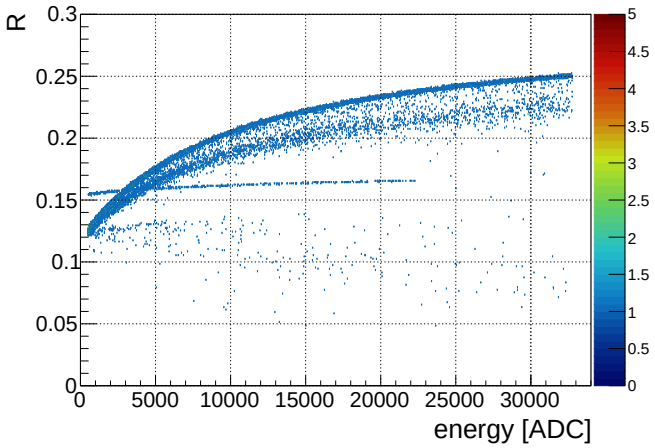

Figure 3.8.: Parameter R plotted against the energy of each event for reactor-ON data before the application of the μ-veto. For the beginning of the integral t_A = 3650 ns and for the ending t_B = 6000 ns was used. Both curved populations can be related to normal (upper) and slow (lower) pulses. The horizontal line between values of $0.15 \leq R \leq 0.17$ comes from events where only an exponential decay is visible (see Fig. 2.15 f). The population below values of $R \leq 0.14$ arise from "wrongly triggered" events (events with a longer pre-trigger, see section 3.2.4 t_0 parameter). The energy range goes up to ~ 33 keV$_{ee}$. The colour bar indicates the number of events per bin.

Next, we can study the relationship between the R_{pulse} parameter of a pulse event and the theoretical noise value for the parameter case with $t_A \neq 0$. In this case, the μ_1 value is only calculated in a region where the pulse has its maximum, leading to a higher value of μ_1 compared to μ_2. The latter value is calculated over the complete pulse and thus, the baseline will decrease the value relative to μ_1. From these considerations, we can conclude $\mu_1 > \mu_2$, meaning that the theoretical noise value will be a lower boundary for the physical R_{pulse} distribution. In Fig. 3.9 distributions for different pulser amplitudes and a noise distribution recorded with a random trigger are shown. It is clearly observable that the noise distribution is centred around the theoretical value $R_{\text{noise}}^{\text{theo}} = 0.1175$, while all measurements with pulses lie above this value. By setting a cut at the theoretical value $R_{\text{noise}}^{\text{theo}}$ and discarding all events with a lower R value, it is expected to reject about half of the noise.

The noise cut described above can be applied to reactor-ON data. In Fig. 3.10, the R distribution for the reactor-ON data, including the noise cut ($R_{\text{noise}}^{\text{theo}} = 0.1175$), is shown. With the noise cut, 7.5% of all events in the noise peak can be rejected. The noise cut rejects events for all bins within the noise peak. Furthermore, events in the physical region are discarded by the cut, as well. In total, 1.3% of the physical events (events with $E \gtrsim 0.2$ keV) are cut (signal loss). Therefore, more noise compared to signal is discarded. The rejected physical events are primarily events with a longer pre-trigger, meaning that the trigger was not working correctly and the time before the pulse is larger. That makes sense because, in this case, the used interval will not fit the pulse any longer. In addition,

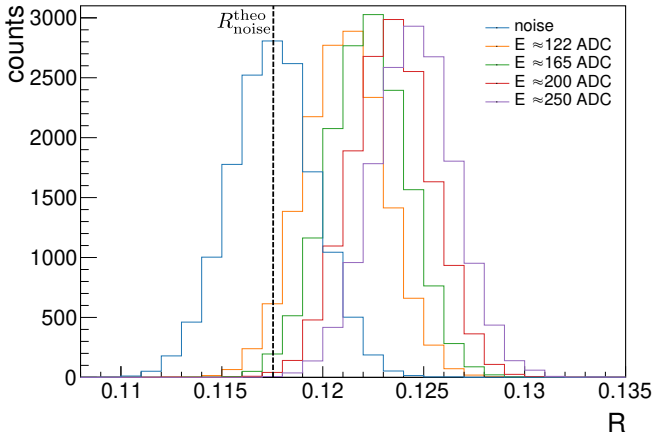

Figure 3.9.: R distributions for different measurements with different pulser amplitudes and a R distribution for random triggered noise. All pulser measurements are performed with rise times compatible with normal pulses and for C1. It can be seen that the noise peak is centred around the theoretical value ($R^{\text{theo}}_{\text{noise}} = 0.1175$), while all other peaks lie above this value.

it is interesting to note that the noise peak is not centred around $R^{\text{theo}}_{\text{noise}}$, in contrast to the noise peak for the random trigger measurement. Due to the shift of the R distribution, only a reduction of 7.5% of the noise events is possible and not 50% as in the study case with the pulser. The shift can be explained by the trigger. For a normal measurement, the DAQ uses an onboard trigger algorithm. Only if the noise has a large enough over or under fluctuation, the trigger will fire. Therefore, the basic assumption of perfectly random noise around the baseline is not valid. These fluctuations lead to R values larger than the theoretical value, resulting in a noise peak shift. Contrarily, for the noise peak measurement, a random trigger was used. With the random trigger, the assumption of random fluctuations is appropriate for the recorded noise, leading to a R distribution centred around the theoretical value.
All cut noise events have energies below $E \simeq 200$ ADC (~ 0.2 keV). However, the trigger efficiency of the CAEN is quite small at these energies, such that the energy region around and below $E \simeq 200$ ADC probably will not be included in the analysis. In addition, the noise reduction of this method is not really large. Therefore, we decided to not focus on further studies regarding the shown noise cut.

In summary, it was shown that the integral ratio method could be used for normal and slow pulse discrimination. Furthermore, it was demonstrated that it is possible to use this method for noise rejection. The noise rejection is especially good if the recorded noise fluctuations are purely random. The integral ratio method will not be further used in this thesis.

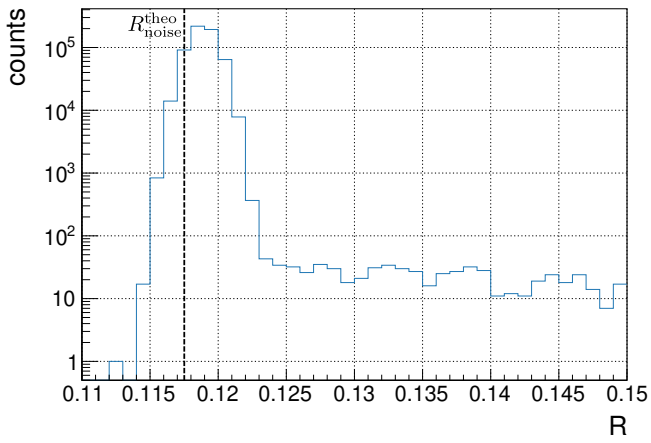

Figure 3.10.: R distribution for reactor-ON data measured with C1. The dashed line is the theoretical lower limit of the R values.

3.1.3. Rise Time Fit

The last technique for pulse shape discrimination presented in this work uses a fit with an appropriate function to describe each pulse and one fit parameter is used as a discriminating variable. As the fit function, a combination of a hyperbolic tangent and an exponential function is chosen, based on the function used by the Texono experiment [50, 55]. The fit function is given by:

$$f(t) = A_0 \left[\tanh\left(\frac{t - t_0}{\tau} \right) + 1 \right] \exp\left(-\tau_c \left(t - t_0 \right) \right) + P_0. \tag{3.9}$$

The fit function has five free fit parameters, which are: A_0, t_0, τ, τ_c, P_0. A_0 is an energy estimate and P_0 is an estimate for the baseline level of the fitted pulse. The parameters t_0 and τ_c are DAQ dependant, with t_0 being proportional to the pre-trigger and τ_c describing the exponential decay of the pulse. Of physical relevance is the τ parameter, being proportional to the rise time of the pulse. The parameter will be used in the rest of this thesis as the discriminating parameter. For a normal pulse, a smaller rise time parameter than for the slow pulse is expected. In Fig. 3.11, a plot of the fit function for different τ values can be found for illustration. A more detailed discussion of the different fit parameters can be found in section 3.2.4.

As a standard figure for the pulse shape discrimination, the logarithm of the rise time parameter is plotted against the energy of the event. An example of a low energy Th-228 measurement with the C1 detector is shown in Fig. 3.12a. In this plot, two distinct separated populations are visible. As expected, for normal and slow pulses, one population has a high τ value around 630 ns and the other one has a lower value around 130 ns. The lower population is split into two sub-populations since a main population between $2.12\ \log_{10}(\text{ns}) < \log_{10}(\tau) < 2.17\ \log_{10}(\text{ns})$ and a smaller population between $2\ \log_{10}(\text{ns}) < \log_{10}(\tau) < 2.12\ \log_{10}(\text{ns})$ is visible. The mean pulses for each population

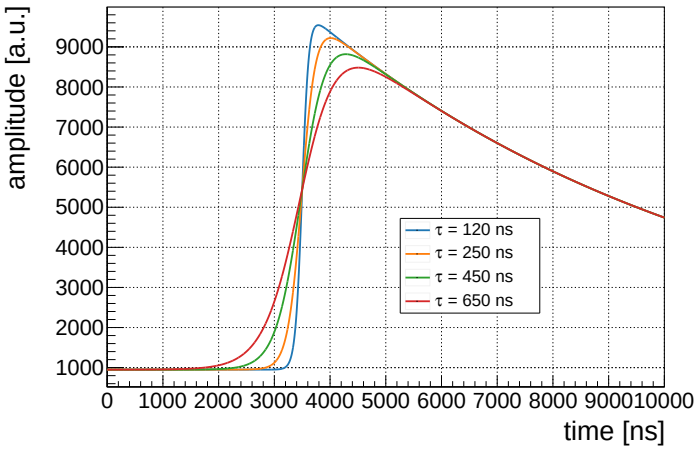

Figure 3.11.: Rise time fit function with different values of τ. The smallest and highest values shown for τ are typical values for normal and slow pulses of the C1 detector, respectively. For the other fit parameters the following values were chosen:$A_0 = 4500$ a.u., $t_0 = 3500$ ns, $\tau_c = 0.000133$ 1/ns, $P_0 = 950$ a.u.. These values are similar to the values of the physical pulses.

can be found in Fig. 3.12b. For the calculation of these mean pulses, the energy region of $E \approx 24 - 25$ keV was used. The mean pulse from the upper population shows the form of a slow pulse, while the two mean pulses from the lower populations show the form of a normal pulse. From the visual inspection, it seems like the upper population consists mainly of slow and the two lower populations consist mainly of normal pulses. A comparison of the different populations to MC simulation will follow in section 4.3. The only difference between the two normal pulse sub-populations is the pre-increase (see section 2.4.1). In the following, the subpopulation with larger τ values and pre-increase will be called higher population and the subpopulation without the pre-increase will be called lower population.
The rise time fit shows the best discrimination power between normal and slow pulses, compared to the other techniques introduced in this section. Moreover, the method allows distinguishing features of the normal pulses. As a result, we will continue in this work with the rise time fit. A detailed evaluation of this technique will follow in section 3.2.

3.2. Rise Time Fit

In this section, the performance of the rise time fit method will be studied in more detail. Different fit functions are presented and compared (section 3.2.1), the influence of smoothing (section 3.2.2) on the fit results is described and the possibility to fix one fit parameter is discussed (section 3.2.3). In addition, the different fit parameters are analysed in more detail (section 3.2.4).

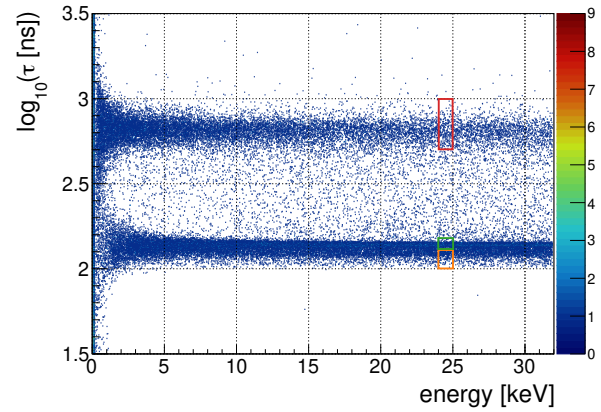

(a)

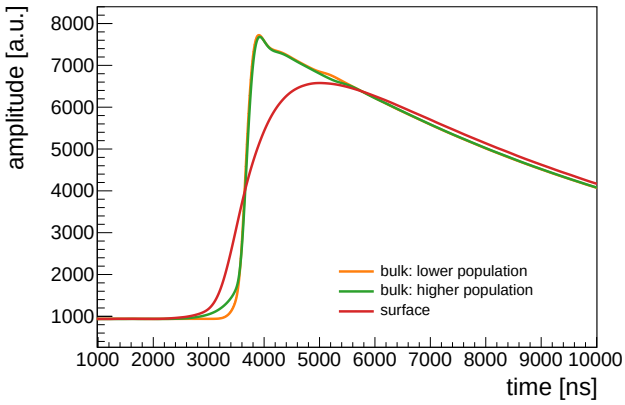

(b)

Figure 3.12.: Figure a) shows the result of a Th-228 measurement performed with the C1 detector at KBR. The logarithm of the rise time parameter τ (y-axis) is plotted against the energy (x-axis) and the colour bar indicates the number of events per bin. In addition, the coloured rectangles mark the regions used to calculate the mean pulses, shown in figure b). The colour of the mean pulses corresponds to the colour of the rectangles.

3.2.1. Different Fit Functions

A limitation of the fit function presented as the third method in section 3.1.3 is that it is not able to describe all features of the pulses. This becomes clearly visible when looking at the fit result of high energy events. An example of a high energy normal and slow pulse with the corresponding best fit function can be found in Fig. 3.13. Both pulses are taken from a high energy measurement with C1 at KBR. Looking at the normal pulse, two main features not described by the fit can be seen. These two features are the 'bump' at the highest point of the pulse and the pre-increase. Both features are already described in section 2.4.1. In contrast, the slow pulses seems to have a different functional form than a hyperbolic tangent. Therefore, other fit functions were tested with the goal to describe the form of the normal pulses (without the features) and of the slow pulses simultaneously.

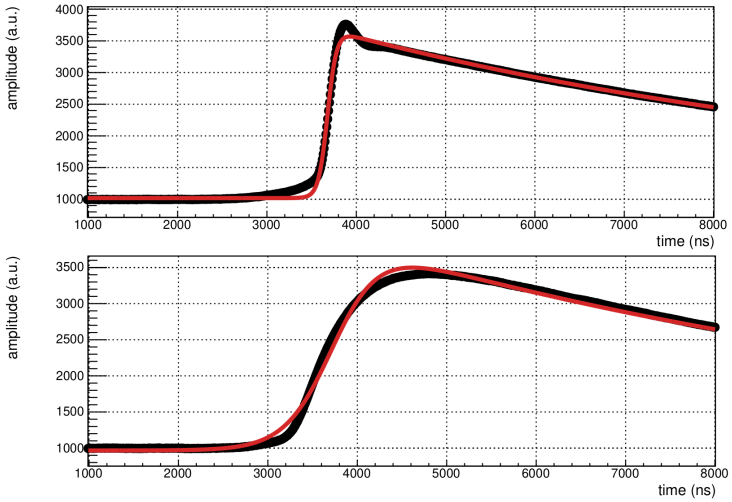

Figure 3.13.: Two high energy examples for a normal and slow pulses with the corresponding fit function. The upper figure shows a normal pulse and the lower figure shows a slow pulse. The black data points describe the recorded pulse and the red curve represents the corresponding best fit. Both pulses are recorded with the C1 detector.

The normal pulse features are not included in the new functions because they do not appear in all detectors (bump) and not for every event (pre-increase). In total, three different functions were tested against the normal function with a hyperbolic tangent. For the three functions, only the part describing the physically interesting part, the rise of the pulse, is changed. The description for the exponential decay and baseline stays the same. All functions are tested on the same data set to allow a better cross-function comparison. As the test data set, a LLL background measurement conducted with the C5 detector was chosen. In the following, each fit function and its performances on the physical data will be presented shortly. As notation, the original fit function with the hyperbolic tangent will be called the 'hyperbolic tangent function'.

Error function

The fit function, including an error function (in the following called 'error function'), has a similar form compared to the hyperbolic tangent function. The full error function is shown below:

$$f(t) = \frac{A_0}{2}\left[1 + \mathrm{erf}\left[\frac{t - t_0}{\sqrt{2}\tau}\right]\right] \exp\left(-\tau_c\left(t - t_0\right)\right) + P_0. \tag{3.10}$$

Similar to the hyperbolic tangent function, the error function has five free fit parameters. The meaning of the different parameters are the same as for the hyperbolic tangent function and are described in section 3.1.3. An example for a normal and slow pulse fitted with the error function can be found in Fig. 3.14. This function does not describe

Table 3.1.: The table shows the run time and the percentage of failed fits for the tested fit function.

fit function	run time (per 10MB)	percentage of failed fits [%]
hyperbolic tangent function	57 s	0.007
error function	1 min 8 s	0.015
skew normal function	1 h 28 min	2.3
lognormal function	2 min	0.017

correctly the form of the slow pulses and looks similar to the hyperbolic tangent function. Also, for the normal pulse, no significant differences between the two functions are found. Looking at the rise time vs. energy distribution of the fit with the error function (Fig. 3.15b), a small shift towards lower values for both populations is visible in contrast to the result of the hyperbolic tangent function (Fig. 3.15a). But overall, no significant improvement regarding the discrimination power of normal and slow pulses is found. Therefore, additional practical criteria were introduced to determine the performance and decide which function should be used. These criteria are: the run time of the fit and the percentage of failed fits. As a failed fit, an event is classified if the fit did not converge after ten tries and the percentage of failed fits gives an idea of how well the function performs in total on a physics dataset. The run time is a rough estimate of the time needed on the cluster to fit a certain amount of data. A data subset of roughly 150000 events, corresponding to ~ 1 GB of data was used to determine these values. The values for the run time and the failed fit percentage can be found in Tab. 3.1. Both criteria are better for the hyperbolic tangent function compared to the error function. In addition, both functions show equally good results for the fit of normal and slow pulses. Consequentially, the hyperbolic tangent function has been preferred over the error function.

Lognormal function

For this function, the cumulative distribution function (CDF) of the lognormal distribution is used. In the following, the function will be called the 'lognormal function'. The complete fit function is shown below:

$$f(t) = A_0 \left[\frac{1}{2} + \frac{1}{2} \operatorname{erf} \left[\frac{\ln t - t_0}{\sqrt{2}\tau} \right] \right] \exp\left(-\tau_c \left(t - \exp\left(t_0 \right) \right) \right) + P_0,\ t > 0 \tag{3.11}$$

Again, this function has five free fit parameters that have the same meanings as described in section 3.1.3. In this function, the t_0 parameter in the error function is defined as a logarithmic value and therefore, in the exponential part of the function, the exponential value of t_0 needs to be taken. An example of the function fitted to a normal and slow pulse can be found in Fig. 3.14. The example plots show that the lognormal and the hyperbolic tangent function describe the normal pulses equally good. Only minor

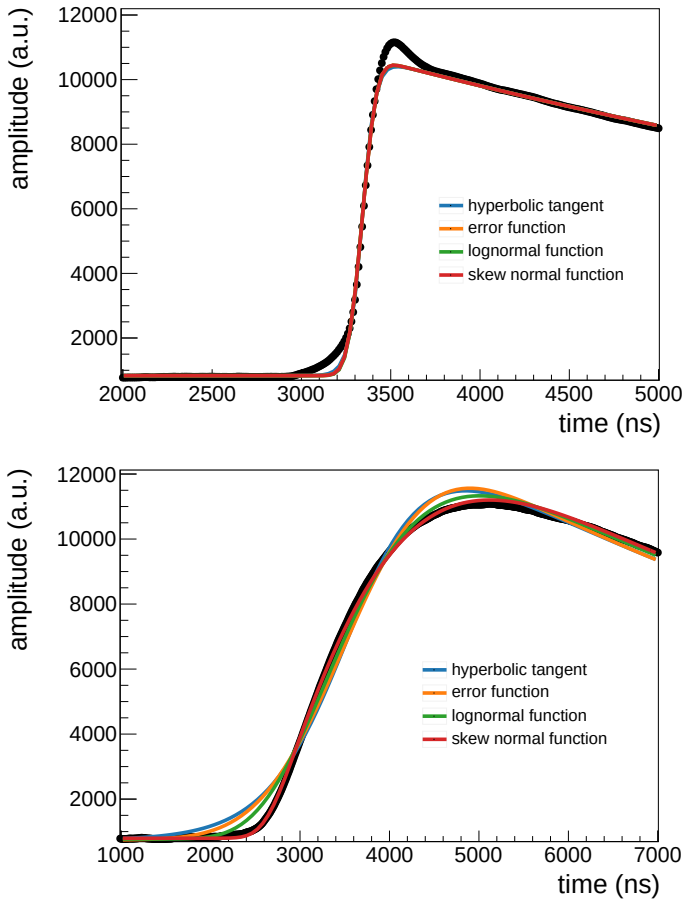

Figure 3.14.: Example fit of different functions to a normal and slow pulse. Both example pulses are taken from a background measurement with C5. Upper plot: The different fit functions compared to a normal pulse are shown. The normal pulse has an energy of $E = 119\,\mathrm{keV}$. Lower plot: The different fit functions compared to a slow pulse are shown. The slow pulse has an energy of $E = 164\,\mathrm{keV}$.

deviations between the two functions were observed. In contrast, the slow pulse is slightly better described with the lognormal function. However, no significantly improvement regarding the discrimination power of normal and slow pulses was found. A rise time vs. energy distribution for the lognormal function can be found in Fig. 3.15c. The percentage of failed fits and the run time can be found in Tab. 3.1. Again, both values are not as good compared to the hyperbolic tangent function. As a result, the lognormal function will not be used instead of the hyperbolic tangent function.

Skew normal function

For the last function, the CDF of the skew normal distribution is chosen. In the following, the function will be called 'skew normal function'. The complete fit function, including

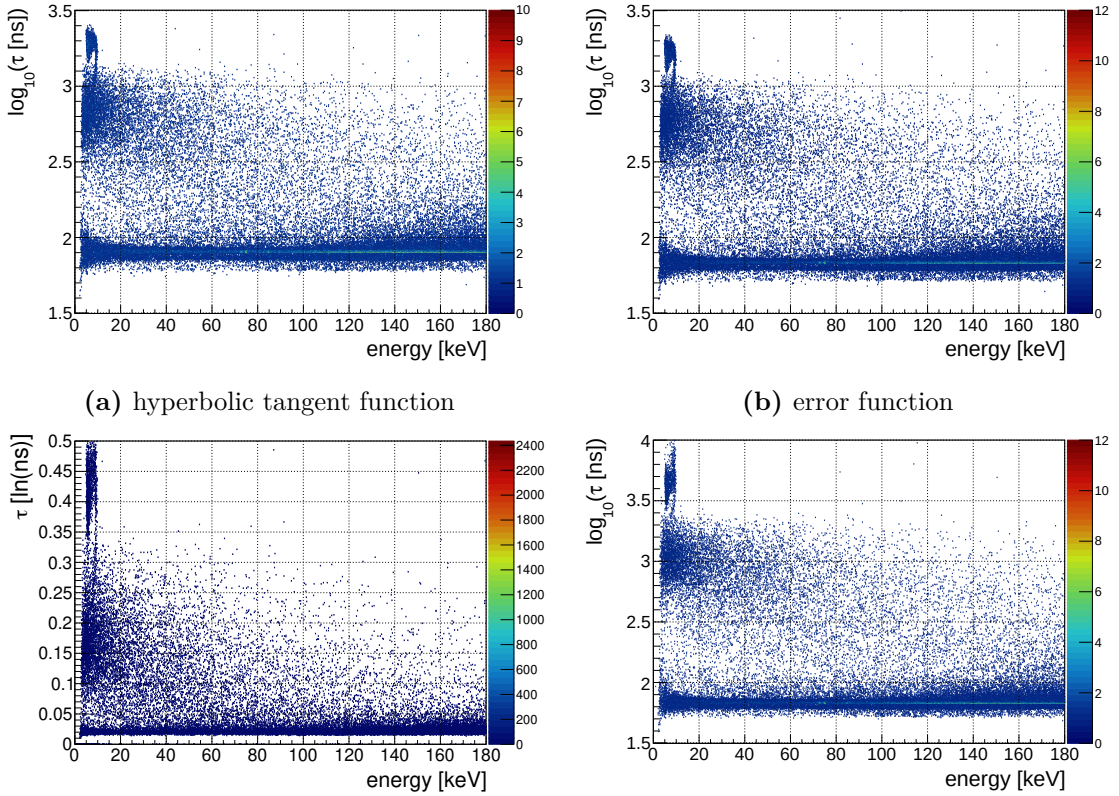

(a) hyperbolic tangent function

(b) error function

(c) lognormal function

(d) skew normal function

Figure 3.15.: Rise time parameter vs. energy plots for the different fit functions compared in section 3.2.1. The "blob" visible in every plot at τ values above the slow pulse population and for energies below $E \lesssim 20$ keV consist mainly of TRP events. The colour bar indicates for each plot the number of events per bin. For figure c), more events are visible because the failed fits are included at $\tau = 0$ ns.

the exponential decay, is shown below:

$$f(t) = A_0 \left[\frac{1}{2} \left(1 + \mathrm{erf} \left[\frac{t - t_0}{\sqrt{2}\tau} \right] \right) - 2T \left[\frac{t - t_0}{\tau}, \alpha \right] \right] \exp\left(-\tau_c \left(t - t_0\right)\right) + P_0, \tag{3.12}$$

with T being Owen's T function [47]. The function has six free fit parameters. Five of the parameters have the same meaning as described in section 3.1.3 and the parameter α represents the skewness of the function. For $\alpha = 0$, the skew normal function reduces to the error function. An example of the function fitted to a normal and a slow pulse can be found in Fig. 3.14. These figures show that the function can describe the normal pulse equally well compared to the other functions discussed above. That makes sense since the fit function reduces to the error function if the α parameter is set to zero. In contrast to the other functions, the slow pulses are described way better by this function. Due to the better description of the slow pulses, a better discrimination of normal and slow

pulses is achieved. A plot showing the rise time parameter τ vs. the energy can be seen in Fig. 3.15d. In this figure, it is visible that the slow pulse population is shifted to a larger and the normal pulse population to a lower τ value compared to the hyperbolic tangent function (see Fig. 3.15a). However, a major disadvantage of the skew normal function is the percentage of failed fits and the run time, both can be found in Tab. 3.1. In both cases, the value of the criteria is way larger compared to the other functions and thus unpractical. As a result, we decided not to continue using this fit function, even though it describes the form of slow pulses better.

In this section, we compared three different fit functions with the hyperbolic tangent function. It was shown that with the skew normal function, a better description of the slow pulses could be achieved, resulting in a better discrimination power of τ. However, the skew normal function has drawbacks regarding the run time and percentage of failed fits. As a result, the hyperbolic tangent function will be used for the PSD. The function already provides a satisfactory discrimination power and shows the best performance regarding the two practical criteria. In the following, this function will be called 'rise time fit function'.

3.2.2. Influence of Smoothing

An idea to reduce the influence of noise on the fit is to apply some kind of smoothing. Especially at low energies, a reduced influence of the noise could help fit the pulses better and increase the discriminating power of τ. As a smoothing technique, a low pass frequency filter was applied. First, the discrete Fourier transform [33] of the pulse was taken. In the frequency space, a low pass filter is applied and afterwards, the inverse discrete Fourier transform is taken. A low pass filter was chosen because it was assumed the noise has a higher frequency (frequency of the dominant noise above order kHz) than the pulse itself. Therefore, theoretically, by cutting away the high frequencies, we should reduce the noise of the pulse. From the Nyquist–Shannon sampling theorem, we can calculate the maximal frequency f_{max} we can see in the pulses given the sampling rate of the CAEN R_{sampling}. The theorem states that [33]

$$f_{\text{max}} = \frac{R_{\text{sampling}}}{2}. \tag{3.13}$$

With a sampling rate of 1 sample every 10 ns [26], a maximal frequency of $f_{\text{max}} = 50$ MHz can be seen in the recorded pulses. In order to start seeing an improvement by eye due to the smoothing, the cut frequency of the low pass filter needs to be about $\mathcal{O}(1\text{ MHz})$. An example pulse recorded with the CAEN and the resulting smoothed pulse can be seen in Fig. 3.16. For the shown pulse, the cut frequency of the low pass filter was set to $f_{\text{cut}} = 250$ kHz. Figure 3.16 shows a significant disadvantage of smoothing. It can be seen that the slope of the smooth pulse is different from the slope of the original pulse, meaning that the smoothing changes the rise time of the pulse. For the example

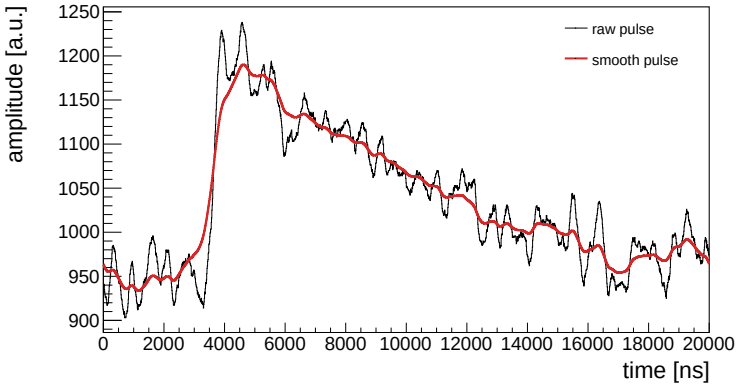

Figure 3.16.: Example pulse from a Th-228 measurement with and without smoothing, recorded with the C1 detector. The pulse has an energy of $E \approx 930$ eV. The black pulse is the original pulse coming out of the DAQ and the red pulse is the smoothed version.

of the smoothed pulse, an aggressive cut frequency was chosen to better illustrate this disadvantage. Subsequently, a cut frequency of $f_{\text{cut}} = 500$ kHz will be used. In order to see the influence of the effect, we applied the rise time fit to a small subset of a Th-228 measurement, once using original (raw) and once using smooth pulses. As the subset, all pulses of the measurement with an energy between $E = 700-1000$ ADC ($E \approx 0.7-1$ keV) are chosen. The energy range is selected because the noise has a large influence on the pulse and the normal and slow pulse population can be distinguished by eye. The resulting $\log_{10}(\tau)$-distributions for both cases are shown in Fig. 3.17. It is clearly visible that for the smooth pulses, the normal and slow pulse populations are closer together compared to raw pulses. That can be explained by an increase in the rise time due to smoothing. An increase in the rise time can be explained by the low pass filter. High frequencies are not only responsible for the noise but also for the "sharp edges" of the pulse. Cutting away the high frequencies will reduce the noise and the "sharp edges", leading to higher rise times. For the PSD, that is a large disadvantage because it lowers the discriminating power of the τ-parameter. Therefore, no smoothing will be applied to the pulses in the analysis chain.

3.2.3. Fixed τ_c Parameter

In this section, the idea to fix the τ_c parameter in the rise time fit function at low energies to a predefined value will be discussed. If the parameter is fixed at low energies, it can help the fit to find and correctly fit the low energy pulses. In general, this idea is possible due to the fact that the exponential decay of the pulse comes from the AC coupling of the CAEN and should be equal for all pulses. Subsequent, the τ_c parameter, the decay constant should be equal for all energies and does not have a physical meaning. Figure 3.18 shows the τ_c-distribution for a Th-228 measurement in the energy range up to $E \approx 32$ keV

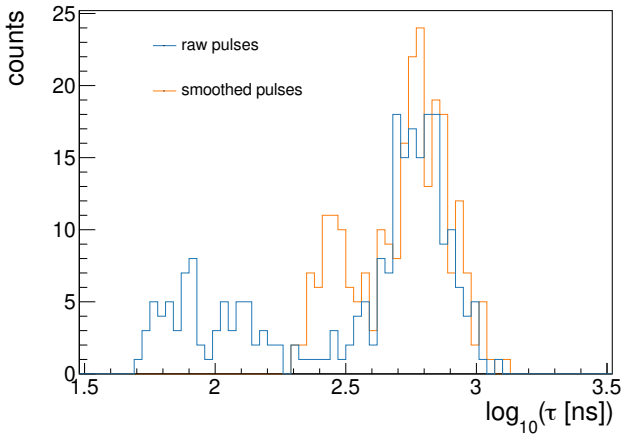

Figure 3.17.: Two $\log_{10}(\tau)$-distributions estimated with and without smoothing. For the blue distribution, original (raw) pulses are used for the fitting and for the orange distribution, smooth pulses are used. For smoothing, a cut frequency of the low pass filter of $f_{\text{cut}} = 500$ kHz was used. The pulses come from a Th-228 measurement, recorded with C1 and all events have an energy between $E = 700 - 1000$ ADC ($E \approx 0.7 - 1$ keV).

performed with the C1 detector. It is clearly visible that the distribution has two peaks in contradiction to the assumption of an equal exponential decay for all events. Looking at the same measurement in the τ_c-$\log_{10}(\tau)$ space (see Fig. 3.18), we see that the left peak of the τ_c-distribution comes mostly from slow pulses, while the right peak comes from normal pulses. Also, it can be seen that the two sub-peaks in the right peak of the τ_c-distribution are correlated with the rise time. The left sub-peak mainly comes from events with shorter rise time, meaning from events with no pre-increase, while the left sub-peak comes mainly from normal pulses with pre-increase.

Next, it needs to be checked if the difference in τ_c corresponds to an effect of the fit routine or to a physical effect from the data. To check the latter hypotheses, a mean normal and a mean slow pulse can be laid on top of each other. For calculating the mean pulses, boundaries for the slow and normal pulse population are estimated by eye from the $\log_{10}(\tau)$-distribution. A plot with the superimposed mean pulses can be seen in Fig. 3.19. The normal pulse is shifted slightly (+5 a.u. up and +208 ns to the right), such that the two exponential decays overlay. It is clearly visible that the two exponential decays are quite similar, as expected. In conclusion, that means the two different peaks are an artefact from the fit itself. An explanation could be that the fitting function is unable to describe completely the form of the slow pulses well. Due to the misfit, an adjustment of the other fit parameters is necessary, leading to a slightly different τ_c value. Since the fit describes the functional form of the normal pulse best, we expect that the τ_c value of the normal pulse is closest to the 'original' value from the CAEN. Moreover, the normal pulse should survive the PSD-cut, making it more important to get precise fit parameters for this pulse type. Therefore, the τ_c will be fixed at low energies to the value estimated from normal pulses at high energies.

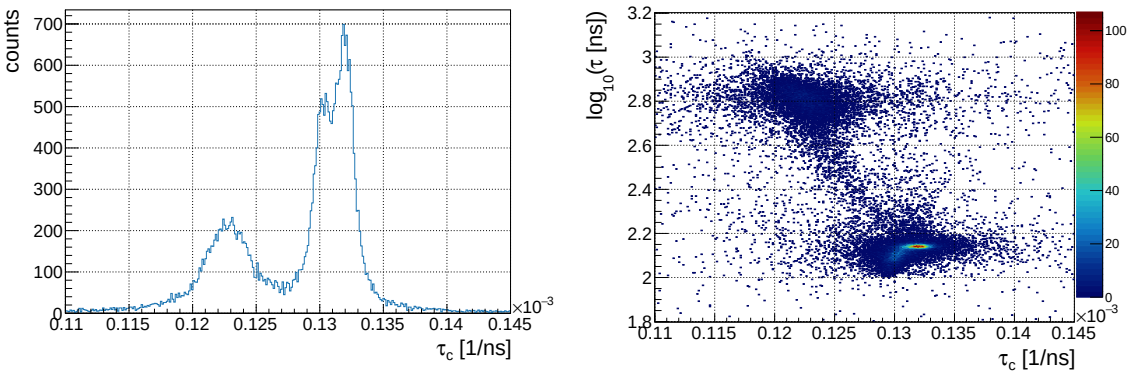

Figure 3.18.: The left plot shows the τ_c-distribution for a Th-228 measurement performed with the C1 detector. The right plot shows for the same measurement a τ_c vs. $\log_{10}(\tau)$ plot. From this plot, it can be seen that the left peak in the upper plot comes from slow pulses, while the right peak comes from normal pulses. The colour bar indicates for the right plot the number of events per bin.

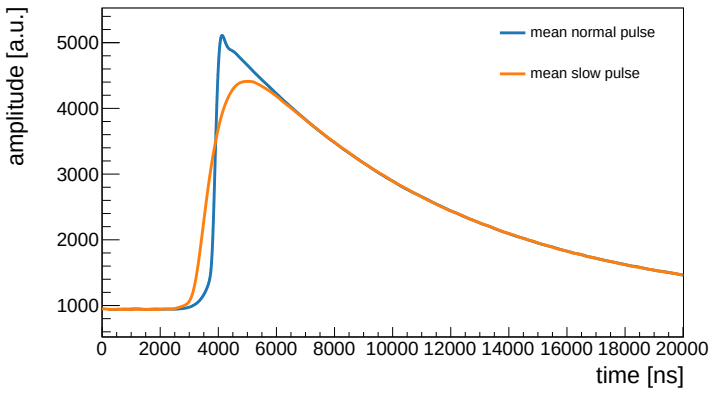

Figure 3.19.: Comparison of the exponential decay for a mean normal ($2.13 \leq \log_{10}(\tau) \leq 2.16$) and a mean slow pulse ($2.75 \leq \log_{10}(\tau) \leq 2.85$). The pulses are taken from a Th-228 measurement conducted with C1.

Furthermore, it needs to be checked how the discriminating power of the rise time parameter is affected if the τ_c parameter is fixed. To do so, the $\log_{10}(\tau)$-distribution for a Th-228 measurement with a fixed τ_c is compared to the same measurement fitted with a free τ_c parameter. The result is shown in Fig. 3.20. The normal pulse peak (left) looks very similar for the fixed and free parameter case, while the slow pulse peak (right) moved a little bit towards higher τ values for the fixed case. No significant reduction of the discriminating power of the rise time is visible when using a fixed τ_c value at low energies. It makes sense that the slow pulse peak changes a bit because all slow pulses are fitted with the fixed τ_c value obtained from the normal pulse population. The change in the $\log_{10}(\tau)$-distribution is minimal and as a result, no discontinuity will be seen in the $\log_{10}(\tau)$ vs. E plot at the boundary between free and fixed τ_c (for example, see Fig. 3.12a, where the boundary is at $E = 7.8$ keV).

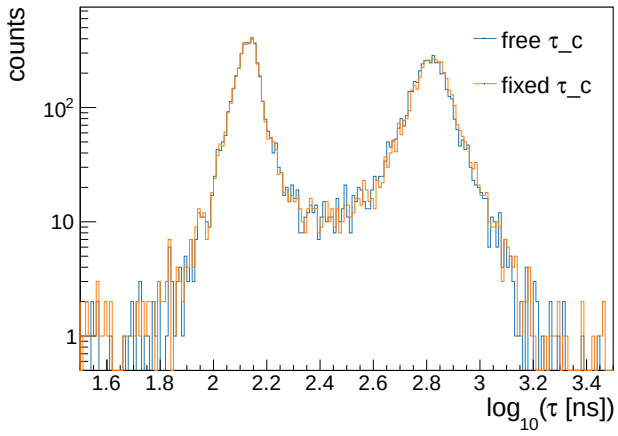

Figure 3.20.: Comparison of a $\log_{10}(\tau)$-distribution with a free and fixed τ_c parameter. The blue distribution is obtained by using τ_c as a free fit parameter, while for the orange distribution, τ_c was fixed. For both distributions, a Th-228 measurement performed with C1 was used.

Table 3.2.: Values used as fixed value for the τ_c parameter. They are obtained in the energy region $E \approx 15 - 31$ keV of a reactor-ON spectrum, fitted with τ_c as a free parameter.

detector	τ_c [1/ns]
C1	0.000131
C2	0.000131
C3	0.000125
C4	0.000132

Next, the values used to fix the τ_c parameters need to be estimated. For this, the reactor-ON data is used. The energy range used for the τ_c estimation is $E \approx 15 - 32$ keV and the τ_c value is estimated by fitting a Gaussian distribution to the normal pulse peak of the τ_c-distribution. In Tab. 3.2, the corresponding values for all four detectors are given. The errors of the estimated values are negligible. In addition, these values were compared to τ_c values estimated in the same way from a Th-228 measurement. For all detectors, except C2, the values are the same. In the case of C2, the value from the Th-228 measurement is $\tau_c = 0.000130$ 1/ns, which agrees at the percent level with the value obtained from the reactor-ON data and was considered negligible. The residual difference between the detectors could arise from differences in the electronic components of the CAEN or could be an effect of the performance of the rise time fit on the slightly different pulse shapes for each detector. The stability of the τ_c values over time is investigated in section 4.1.
The energy region in which the τ_c parameter is used as a fixed parameter is estimated from the reactor-ON spectrum. For low energies, the two populations visible in the τ_c-distribution start to mix. The approximated starting of this mixing is chosen as the boundary point between a fixed and free τ_c parameter. For all four detectors, the value was selected to be $E = 8000$ ADC ($E \approx 7.8$ keV).

In conclusion, for events with an energy below $E = 8000$ ADC, the pulse is fitted with τ_c as a fixed parameter. The τ_c parameter is fixed to the value shown in Tab. 3.2, depending on the detector. The idea behind fixing this parameter is to use information obtained at high energies to help the fit converge and correctly fit the pulses at low energies.

3.2.4. Analysis of the Different Fit Parameters

In this section, the different fit parameters will be explained in more detail. Moreover, the features arising in the distributions of the parameters coming from the fit to physical data will be discussed. In the end, the possibility of applying quality cuts to the fit parameters, except the τ parameter, will be evaluated. For this section, 'low energy' will refer to an energy range from 0 ADC to 8000 ADC ($\sim 0 - 7.8$ keV) and the range from $8000 - 32000$ ADC ($\sim 7.8 - 31$ keV) will be called 'high energy'. The separation into these regions comes from the boundary, where the τ_c parameter changes from a free to a fixed parameter.

Rise time: τ
The τ parameter is an estimate for the rise time of the pulse. As the rise time, the time difference between the point of 10% and 90% of the pulse's maximal height is defined [36]. We can calculate the relation of the τ parameter to the rise time for a simplified version of the fit function. For the simplified version, we neglect the exponential decay (or set $\tau_c = 0$), which results in the following function:

$$f(t) = A_0 \left[\tanh\left(\frac{t - t_0}{\tau} \right) + 1 \right]. \tag{3.14}$$

Also, the P_0 parameter is set to zero, because the baseline is assumed to be zero for the definition of the rise time. With this function, we found that the relation between the τ parameter and the rise time of the function is the following:

$$\tau = \frac{t_{90} - t_{10}}{2\,\mathrm{artanh}(0.8)}, \tag{3.15}$$

where t_{90} (t_{10}) is the time when the function is at 90% (10%) of its maximal height. The calculation for this relationship can be found in the appendix C.1. In this simplified case, the τ parameter is directly proportional to the rise time of the function. It is interesting to note that this relation is independent of the pulse's height, meaning that the τ parameter is independent of the energy of the event. The actual pulses have an exponential decay and thus are more similar to the complete fit function (see eq. 3.9). For the complete fit function, a correction will be introduced in the relation, which scales with the strength of the τ_c parameter. Unfortunately, it is not trivial to calculate the relation for the complete fit function.

Table 3.3.: Estimate of the typical ranges of the rise times at energies around ~ 15 keV for the four different detectors. These values are obtained by a rough estimation of the ranges of the normal and slow pulse population from a $\log_{10}(\tau)$-distribution.

detector	normal pulse: τ [ns]	slow pulse: τ [ns]
C1	100 - 150	450 - 1000
C2	140 - 195	355 - 800
C3	145 - 215	445 - 1000
C4	125 - 190	355 - 1120

Also, the τ parameter is at the point $t = t_0$ related to the slope of the pulse. The relation can be calculated for the complete fit function and is:

$$f'(t_0) = A_0(\frac{1}{\tau} - \tau_c) \tag{3.16}$$

Again, the calculation of the relation can be found in the appendix C.1. In the case of the simplified function, the τ_c parameter is set to zero and the relation reduces to an anti-proportional behaviour between the slope and the τ parameter. It makes sense that the relation depends on the pulse's height A_0 because either the time interval of the increase or the slope needs to change for different pulse heights and the rise time-τ relation is height independent already. In addition, the relation shows that the correction introduced by the exponential decay is relatively small. For realistic values of $\tau = 150$ ns and $\tau_c = 0.000131$ 1/ns, the correction due to the exponential decay is of the order of 2%. Example plots showing $\log_{10}(\tau)$-distributions can be seen in Fig. 4.6 and examples for $\log_{10}(\tau)$ vs. energy plots can be seen in Fig. 3.15a and 3.12a. Typically, two peaks can be seen in the $\log_{10}(\tau)$-distribution, one at lower and one at higher τ values. These two peaks can be assigned to normal and slow pulses, respectively. Both peaks are clearly separated at higher energies, while they start to fuse to one peak at lower energy. The typical rise times of normal and slow pulses at energies around $\sim$ 15 keV for the four different detectors are shown in Tab. 3.3

Artefacts can appear in the $\log_{10}(\tau)$-distribution. These artefacts usually are clearly visible and can be assigned to unphysical pulses. An example of an artefact can be seen in Fig. 3.15a at an energy of $E = 5 - 10$ keV. The artefact in Fig. 3.15a comes from events happening during the TRP reset and thus can be rejected by the TRP veto.

Energy estimate: A_0

The A_0 parameter is an estimate of the energy of the pulse. In the case of the simplified fit function (see eq. 3.14), the maximum of the pulse is proportional to the A_0 parameter:

$$f_{\max} = 2A_0, \tag{3.17}$$

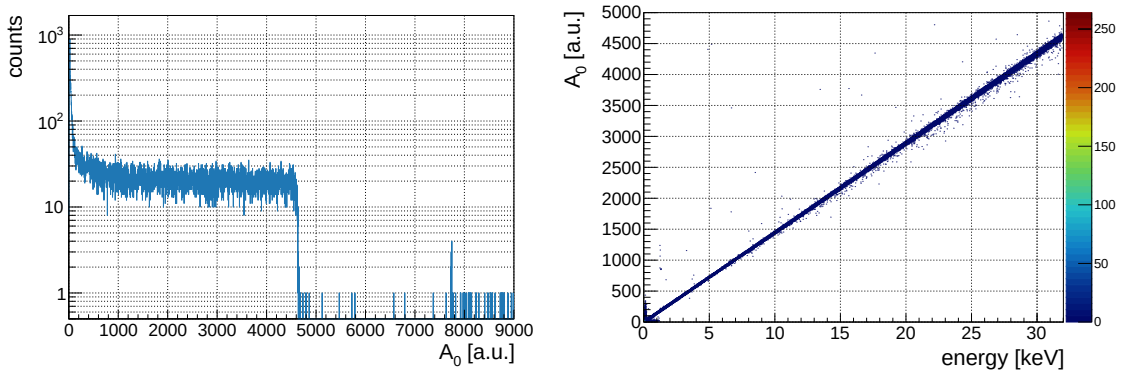

(a) **(b)**

Figure 3.21.: In figure a), the A_0-distribution for a Th-228 measurement with the C1 detector is shown. In figure b) the same measurement is shown in an A_0 vs. energy plot. The colour bar indicates the number of events per bin.

with the baseline set to zero. However, including the exponential decay makes this relation more complex. The relation can be derived by calculating the derivative of the fit function and setting the result equal to zero. More details can be found in the appendix C.1. The relation for the complete fit function is:

$$f_{\max} = f(t_{\max}) = A_0(2 - \tau\tau_c)\left(\frac{\tau\tau_c}{2 - \tau\tau_c}\right)^{\frac{\tau\tau_c}{2}} + P_0, \tag{3.18}$$

$$t_{\max} = t_0 - \tau \log\left(\sqrt{\frac{\tau\tau_c}{2 - \tau\tau_c}}\right). \tag{3.19}$$

Equation 3.18 shows that a correction term reduces the maximal pulse height relative to the A_0 parameter. The correction term is a function of the rise time parameter τ and the exponential decay parameter τ_c. As a result, the A_0 parameter is not an estimate for the maximal point of the pulse but for the height the pulse would have reached if the exponential decay parameter was zero or very small. Meaning, the A_0 parameter estimates the reached pulse height if the complete charge would be collected before the exponential decay starts. Therefore, A_0 is proportional to the total created charge and thus is an energy estimate. The effect that pulses with a longer rise time have a smaller amplitude due to the exponential decay is called ballistic deficit [36] and can lead to problems in the energy reconstruction. However, the trapezoidal filter used by the CAEN effectively eliminates this effect if the flat top of the trapezoidal filter is large enough [42]. That explains why the mean slow pulse in Fig. 3.12b has a different amplitude than the normal mean pulse, even though they were calculated from the same energy range. Also, the ballistic deficit plays no role if the deficit is constant for all energies (for example, only considering normal pulses) because the spectrum is calibrated with physical lines.
The time when the pulse reaches its maximum is shown in eq. 3.19. In this equation, it is shown that the position does not depend on the energy of the event but only on the rise

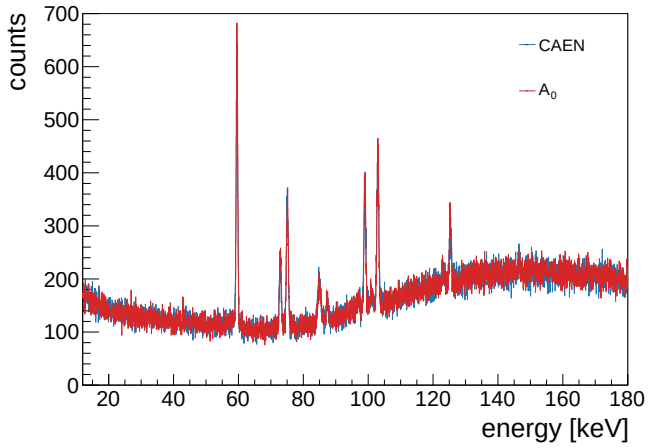

Figure 3.22.: Comparison of the Am-241 energy spectrum created by the CAEN (blue) with the energy spectrum created by the fit with the A_0 parameter (red). Both spectra are calibrated with the Am-241 lines at 59.54 keV, 98.97 keV and 102.98 keV [9]. For the measurement, the C5 detector was used and the measurement was conducted in the LLL.

time parameter τ, the exponential decay parameter τ_c and the shift of the pulse along the time axis t_0.

In Fig. 3.21a, an A_0-distribution for a Th-228 measurement is shown. Due to a lack of physical lines in the recorded energy range of the Th-228 spectrum, only a continuum is expected. The continuum is visible for the A_0 parameter, too. It can be seen that for values larger than the continuum, single events are visible in the A_0-distribution. The events have values larger than $A_0 > 4700$ a.u.. Looking at these events, we found that they are saturation events and a few events happening during the exponential decay of a previous pulse. In addition, a strong increase at low A_0 values is visible, which is dominated by noise from energies below 200 eV. The same A_0-distribution is shown in Fig. 3.21b as a function of the energy of each event. No artefact is seen in the plot at the energy of $E \approx 7.8$ keV, where the τ_c parameter is fixed. Since the parameter is an estimate for the height, the pulse would have reached without the exponential decay, this is what we would expect.

In Fig. 3.22, another A_0 spectrum is shown. For the measurement, an Am-241 source was used and the energy range goes up to $E = 180$ keV. Also, the measurement was done in the LLL at MPIK with the C5 detector without any shielding. That explains why background lines next to the Am-241 lines are visible in the spectrum. The A_0 spectrum is superimposed with the energy spectrum created by the CAEN. Comparing both, it is visible that they match quite good. The maximal deviation of two peaks is of the order of 50 eV and lies completely in the range of the error coming from the calibration of the two spectra. Again, this shows that the A_0 parameter is an estimate of the energy of an event. In addition, the resolution (FWHM) of some peaks is a little bit, but significantly better (smaller FWHM) for the spectrum created with the

A_0 ($E = 59.54$ keV, FWHM $= 0.294 \pm 0.004$ keV) parameter compared to the spectrum created by the CAEN ($E = 59.54$ keV, FWHM $= 0.325 \pm 0.005$ keV). A reason for this improvement of the resolution is not found yet. However, before the A_0 parameter can be used as the default energy-reconstruction parameter, more investigations and consistency checks are necessary. Below an energy of 12 keV, the spectrum is not shown in the plot because TRP reset artefacts are visible.

Pre-trigger: t_0

The t_0 parameter is proportional to the time recorded before the actual pulse appears, meaning t_0 is proportional to the pre-trigger. Since the pre-trigger is a setting from the DAQ, we would expect that t_0 is equal for all pulses. The trigger fires at the zero crossing of the second derivative of the pulse. With this information, we can calculate the time when the trigger fired for a certain pulse by taking the second derivative of the fit function and setting it to zero. For the simplified fit function (see eq. 3.14), the calculation is straightforward and the second derivative is:

$$\frac{\mathrm{d}^2}{\mathrm{d}t^2} f(t) = \frac{2A_0 \left(1 - \tanh^2\left(\frac{t-t_0}{\tau}\right)\right) \tanh\left(\frac{t-t_0}{\tau}\right)}{\tau^2} \tag{3.20}$$

Since the hyperbolic tangent becomes zero if the argument is zero, the second derivative is zero for $t = t_0$. The result shows that the trigger time is equal to t_0 for the simplified fit function; therefore, t_0 should be an estimate for the pre-trigger. In addition, the trigger time does not depend on other parameters, meaning that the t_0 parameter should be equal for normal and slow pulses. However, for the complete fit function (see eq. 3.9), the relation between the trigger time and t_0 is more complicated. The time is calculated in the same way and the resulting relation is:

$$t = t_0 - \tau \log\left(-\frac{\sqrt{-\tau^2\tau_\mathrm{c}^2 + 2\tau\tau_\mathrm{c} + 1} + 1}{\tau\tau_\mathrm{c} - 2}\right). \tag{3.21}$$

The second derivative of the complete fit function can be found in eq. C.2. In the limit where $\tau_\mathrm{c} = 0$, we obtain the relation for the simplified fit function again. The pre-trigger (trigger time) is fixed for all pulses by the CAEN. If we calculate the t_0 parameter for different rise times but the same trigger times, we get different values for t_0. The relation shows that if the trigger time is fixed, a higher value of t_0 is expected for larger rise times (slow pulses). As a result, two different peaks for normal and slow pulses are expected in the t_0-distribution.

In Fig. 3.23, a t_0 vs. energy plot is shown. The plot shows two clearly distinguishable populations. The upper population consists of slow pulses and the lower population consist of normal pulses. In the slow pulse population (higher t_0 values), a discontinuity is visible at the energy $E \approx 7.8$ keV, which corresponds to the point where τ_c changes from a free to a fixed parameter. Contrarily, the normal pulse population shows no effect due to the

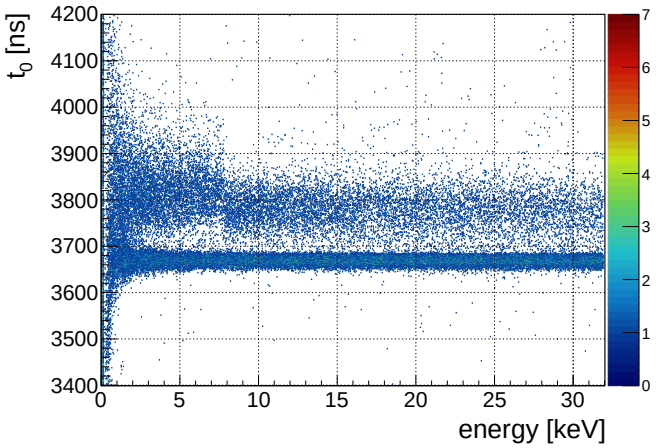

Figure 3.23.: Plot showing the t_0 parameter of the fit, plotted against the energy of each event. The colour bar indicates the number of events per bin. The plot is produced from a Th-228 measurement, which was recorded with the C1 detector.

fixing of τ_c. Only the slow pulse population is affected because, for the slow pulses, the mean τ_c value changes when the parameter gets fixed. Therefore, the other fit parameter needs to be adjusted in order to fit the pulse, leading to a slightly different t_0 value.

high energy t_0-distribution: In Fig. 3.24a, a plot of the t_0-distribution for the high energy case can be seen. The distribution can be divided into four areas, which are marked in the plot. The first area goes from $t_0 \approx 3600 - 3700$ ns and contains all events inside the main (left) peak. This peak contains most of the events and corresponds mainly to normal pulses. Also, the peak has an asymmetry, which can be explained with the superposition of two peaks, one from the higher and one from the lower population. The sub-peak of the lower population has slightly lower t_0 values than the peak from the higher population, resulting in an asymmetric peak if both are combined. With the effect from the pre-trigger explained above, not the complete difference of the two sub-peaks can be explained. An explanation for the rest of the difference could be that the fit is not able to describe the pre-increase, which could result in slightly different values for the fit parameters. The second area of the t_0-distribution, going from $t_0 \approx 3700 - 3900$ ns, contains the right peak. Events inside this peak can be mainly assigned to the slow pulses. The difference between the normal and slow pulse peak can be explained with two effects. First, a part of the deviation can be explained with the pre-trigger effect. From eq. 3.21, the deviation of the two peaks from this effect can be estimated to be around 50 ns. That is not enough to explain the complete measured difference. Secondly, as shown in Fig. 3.13, the fit function does not fit the form of slow pulses well. Using the function to fit the slow pulse can lead to larger t_0 fit parameters than expected if the function would be fitting well. The third area of the distribution is a small peak at higher t_0 values and goes from 4800 ns to 5800 ns. Only a few events have a t_0 parameter inside this area and they are normal and slow pulses. These events have a longer pre-trigger than the majority of the

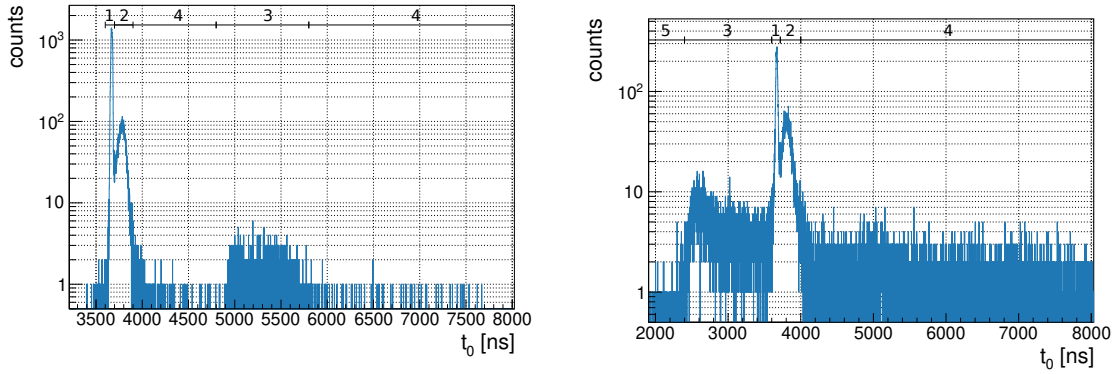

(a) **(b)**

Figure 3.24.: t_0-distribution for the same Th-228 measurement recorded with the C1 detector as shown in Fig. 3.23. In figure a), the distribution for the high energy range and in figure b) the distribution for the low energy range is shown.

events, resulting in a larger t_0 value. Otherwise, the recorded pulses are looking normal and also, the reconstructed energy seems to be correct. The last area of the distribution contains the events between the different peaks, meaning events with parameters between $t_0 \approx 3900 - 4800$ ns and $t_0 \approx 5800 - 10000$ ns. First of all, the number of events in this area is very small. The events in the lower of the two regions are mostly events looking like MSE, with one of the two pulses being a slow pulse. The events in the upper region are mostly wrongly triggered events like in area three and some few saturation events.

low energy t_0-distribution: A t_0-distribution for the low energy range can be found in Fig. 3.24b. The distribution is separated into five areas, which are marked in the plot. The first area contains the main peak and goes from $t_0 \approx 3600 - 3720$ ns. Similar to the high energy case, this peak contains mainly events from the normal pulse population. However, in contrast to the high energy case, the peak has a weaker asymmetry. That makes sense because the noise weakens or erases the differences between the pulses from the higher and lower population and therefore, the difference of the fit parameter becomes weaker or disappear. The second area of the distribution goes from $t_0 \approx 3720 - 4000$ ns and contains mostly events from the slow pulse population. In the third area, going from $t_0 \approx 2400 - 3600$ ns, no events are visible for the high energy case. Looking at these events more closely shows that most of the events come from energies below $E \approx 200$ eV. Most of these events look like fitted noise. However, it is hard for some events with higher energies to distinguish by eye if they are noise or physical events. Also, the fourth area of the distribution, going from $t_0 \approx 4000 - 10000$ ns, contains many of the fitted noise with energies below $E \approx 200$ eV. In addition to the noise, wrongly triggered events, similar to the high energy case, are included in this region. The wrongly triggered events are mainly concentrated around $t_0 \approx 5000$ ns. In the last area of the distribution, only fitted noise events are visible. The region goes from $t_0 \approx 0 - 2400$ ns. All in all, the distribution for the low energy range looks quite similar to the high energy case, with the difference that

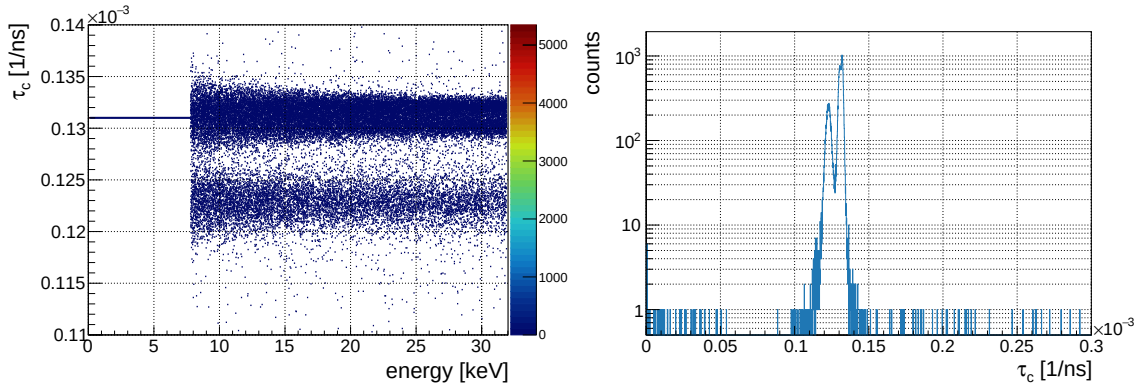

(a) **(b)**

Figure 3.25.: Figure a) shows a τ_c vs. energy plot. For energies below $E \approx 7.8$ keV, the τ_c value is fixed to a specific value. The colour bar indicates the number of events per bin. Figure b) shows a τ_c-distribution for the high energy region. For both plots, a Th-228 measurement recorded with the C1 detector is used.

fitted noise is now included.

The pre-trigger of the DAQ is set for all measurements to a value of 5000 ns. Therefore, from a naive point of view, we would expect that the fitted t_0 values should be around this value. However, looking at the t_0-distributions, we find that the normal pulse events are located in the region of $t_0 \approx 3600 - 3720$ ns. A speculation is that the difference is connected to the shaping applied to the signal for the trigger, but this needs further investigation. Interestingly, few events are centred around a value of $t_0 \approx 5000$ ns. A reason for these 'wrongly' triggered events has not been found yet.

Exponential decay time: τ_c

The τ_c parameter describes the exponential decay of the pulse created by the DAQ system. As explained before, the parameter is fixed to a certain value for energies blow $E = 8000$ ADC. More details about the procedure to fix the parameter and the fixed τ_c values for the different detectors can be found in section 3.2.3. In Fig. 3.25a, a τ_c vs. energy plot for a Th-228 measurement is shown. Two populations are visible, as well as two subpopulations for the normal pulse population. A possible reason for the different τ_c values is investigated in section 3.2.3.

high energy τ_c-distribution: In Fig. 3.25b, a τ_c-distribution for the high energy case is shown. Since the two large peaks are explained already, only two interesting regions of the distribution are left. The first region contains events with values of $\tau_c \approx 0 - 0.000117$ 1/ns and the second region includes events with $\tau_c \approx 0.000135 - 0.0005$ 1/ns. In the first region, two kinds of events appear. First, saturation events contribute in this region, mainly below values of $\tau_c \approx 0.00006$ 1/ns. Events with a value higher than $\tau_c \approx 0.00006$ 1/ns mostly have a second peak visible, located in the exponential decay of the first pulse. Also, the second region can be split into two parts. For values below $\tau_c \approx 0.00016$ 1/ns, different

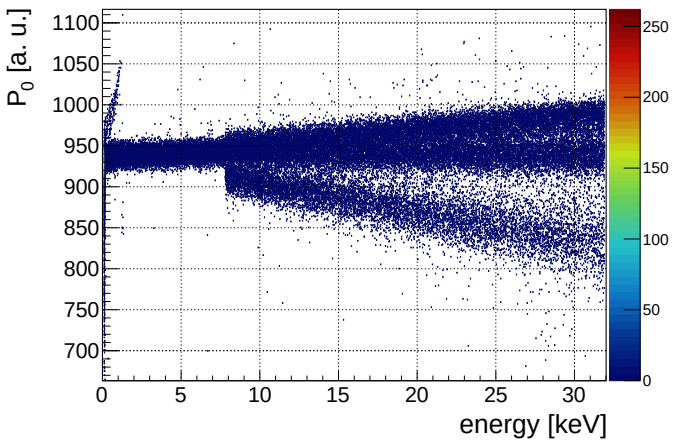

Figure 3.26.: P_0 parameter of the fit, plotted against the energy of each event. The colour bar indicates the number of events per bin. The plot is produced from a Th-228 measurement which was recorded with the C1 detector.

types of events contribute. Some of the events, especially at the lower part of this area, are normal looking pulses. Another type are events with two peaks visible, similar to MSE. The last type are events happening at the very end of the exponential decay of a previous pulse. Pulses appearing in the exponential decay of an event prior contribute to the events above $\tau_c \approx 0.00016$ 1/ns, as well. In addition, saturation events are located in this region, too.

Baseline estimate: P_0

The P_0 parameter is an estimate for the baseline of the pulse. Therefore, the parameter should be equal for all measured events. A plot showing the parameter P_0 plotted against the energy of each event is shown in Fig. 3.26. Multiple interesting effects are visible in this plot. Most noticeable is that P_0 splits up into three different populations at an energy of $E \approx 7.8$ keV and that these populations diverge for higher energies. Other visible effects are that the single population at smaller energies has a small drift towards lower P_0 values and a small artefact at $E \lesssim 1$ keV. First, the split into three populations at high energies will be discussed. The upper two populations only have a relatively small separation at the highest energy and seem to merge earlier than the lowest population. The lowest population has a higher difference to the middle population at the highest energy and is separated from the other two populations until the τ_c parameter is fixed. In addition, the upper and lowest population both diverge from the middle population, meaning that the effect is energy-dependent and increases with higher energy. By looking at the events inside the three populations, it can be seen that the upper population mainly consists of normal pulses with a pre-increase, the middle population contains mainly normal pulses without a pre-increase and the lowest population contains mostly slow pulses. For slow pulses, the τ_c parameter changes most when it is fixed, explaining the abrupt cut of the slow pulse population at the point where τ_c is fixed. The questions are why the three different

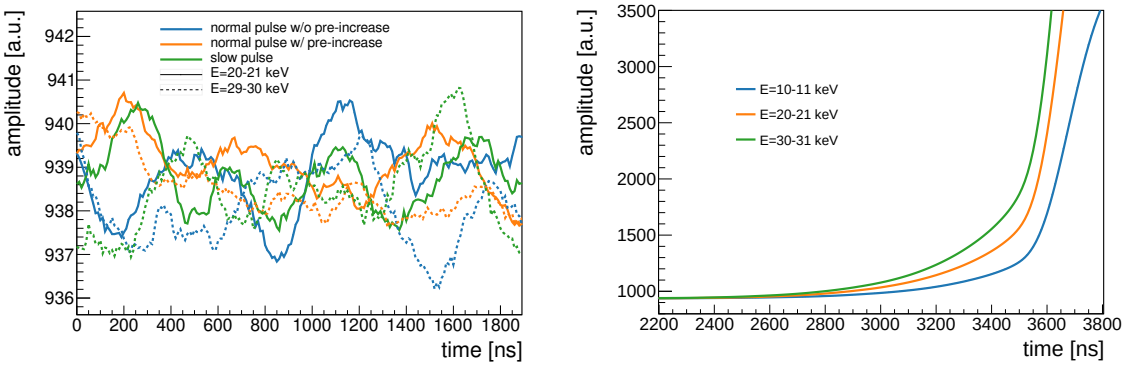

(a) **(b)**

Figure 3.27.: Figure a) shows different mean baselines calculated for different energies and different P_0 parameter populations. Figure b) shows the mean pre-increase for three different energies. For both plots, a Th-228 measurement recorded with the C1 detector is used.

populations exist and why they diverge. Looking at the mean baseline of these populations at different energies, we find that the baselines are similar for all populations and have a very similar value at different energies. Accordingly, the effect comes from the fit and not from the data. A plot showing the mean baselines can be found in Fig. 3.27a. The middle population (normal pulse without pre-increase) seems to be the population, matching with the single population at low energy. That makes sense because the fit function does not describe the pre-increase. Therefore, the events in the middle population are described best by the fit, leading to the best possible fit of the baseline. Also, the fixed τ_c parameter is estimated from the normal pulses, meaning that a change of the fit parameter is not expected when τ_c is fixed. A possible explanation for the two normal pulse populations merging before $E \approx 7.8$ keV could be that at lower energies, the pre-increase is hidden by the noise, making the two normal pulses indistinguishable for the fit. The rise in the P_0 parameter towards higher energies could be connected to the pre-increase. As said before, the pre-increase is not modelled with the fit function. Consequently, the pre-increase can pull the baseline parameter of the fit towards higher values in order to compensate for the pre-increase. That would explain the higher P_0 parameter compared to the baseline estimated from the data. Also, the drift towards higher P_0 values can be explained by this effect. For higher energies, the pre-increase reaches larger values. As a result, the P_0 parameter could be pulled towards larger values than at lower energies, where the pre-increase is not as strong. In Fig. 3.27b, three mean pulses, estimated from the same $\log_{10}(\tau)$ range, but different energies are shown. The figure shows that for roughly the same rise time, the pre-increase is larger for the pulses at higher energies. For the slow pulses, in order to fit the main part of the pulse and exponential decay better, the P_0 parameter is set by the fit to a value lower than the data baseline. The effect should come from the misfit of the fit function to the slow pulse and seems to be mainly driven by the exponential decay because after τ_c is fixed, the effect disappears. Also, due to the

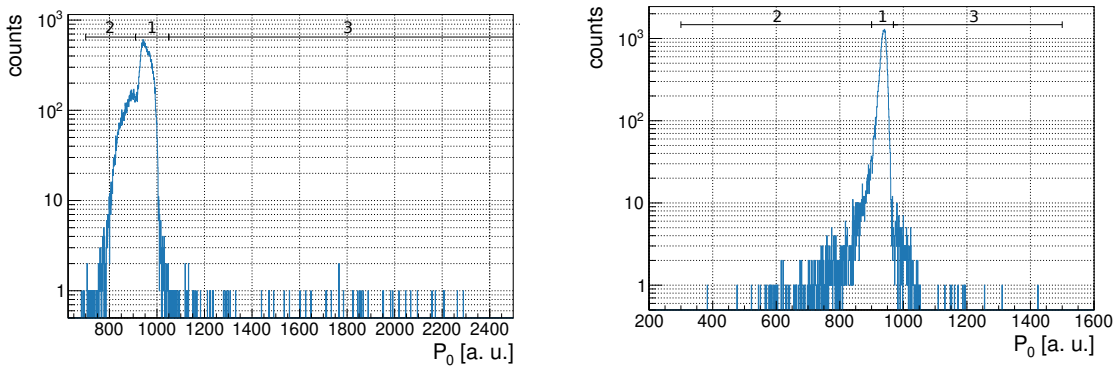

(a) **(b)**

Figure 3.28.: P_0-distribution for the same Th-228 measurement recorded with C1 as shown in Fig. 3.26. In figure a) the distribution for the high energy and figure b) for the low energy case is shown.

decreasing P_0 value at higher energies, it seems that the effect is getting larger for higher energies.

In the low energy range, only one population is visible. This population has a weak drift towards lower P_0 values. In total, the population drifts around $\Delta P_0 \approx 5$ a.u. over an energy range of $\Delta E \approx 7.3$ keV. An explanation for this effect has not been found yet.

The last effect visible in Fig. 3.26 is an artefact for energies below $E \lesssim 1$ keV. At these energies, a small vertical band goes towards larger P_0 values. The band mainly contains fitted noise and very few low energy pulses. Due to larger over fluctuations, the noise can reach higher energy, such that it appears in this artefact.

high energy P_0-distribution: In Fig. 3.28a, a P_0-distribution for the high energy region is shown. The distribution can be separated into three areas, which are marked in the plot. The first region contains the main peak and goes from $P_0 \approx 910 - 1050$ a.u.. Mainly normal pulses make up this peak. As seen before in the P_0 vs. energy plot, the normal pulse population splits into two diverging populations. Accordingly, the main peak is the superposition of both populations, resulting in an asymmetric peak. The second region goes from $P_0 \approx 700 - 910$ a.u. and contains mostly slow pulses. The last region goes from $P_0 \approx 1050 - 4000$ a.u.. Only very few events are in this region and they are mostly saturation events, events happening during the exponential decay of a previous pulse and events with multiple peaks. However, few normal pulses are contained in this region, too.

low energy P_0-distribution: A plot of the P_0-distribution at low energies is shown in Fig. 3.28b. Again, the distribution can be separated into three regions, which are marked in the plot. The first region covers $P_0 \approx 900-970$ a.u. and only one main peak is visible. In this region, normal, slow pulses and also some noise from below $E < 200$ eV are included. The second population, located left from the main peak, goes from $P_0 \approx 300 - 900$ a.u.. Most of the events in this region come from energies below $E < 150$ ADC and are noise events. The last region covers the range of $P_0 \approx 970 - 1500$ a.u. and mainly contains the events of the artefact, which was discussed before.

Quality Cuts

In general, the fit parameters can be used to apply quality cuts[2] to the data to cut artefacts, unphysical pulses and noise. For this thesis, only quality cuts where no signal is cut are chosen. For some parameters, more aggressive quality cuts could be applied. However, an additional efficiency calculation would be needed for these cuts. In the following, we shortly discuss the possible cuts for each fit parameter and how much they influence the spectrum.

First, the "error bins" can be cut. These are two bins where events are stored, which have a non-converging fit, are below a specific energy or are unphysical of the type shown in Fig. 2.15 f). How these events are encoded in the parameter distributions is explained in section A.3. Cutting the error bins is parameter independent and can be performed for one of the fit parameters.

No quality cut is investigated for the τ parameter because this parameter is used for the PSD later. Therefore, no other cuts will be applied to this parameter.

A cut applied for the parameters A_0 and τ_c can reduce the number of saturation events that are not flagged by the DAQ and events happening in the exponential decay of a previous pulse. For A_0, the cut should be applied to the spectrum above $A_0 = 4700$ a.u. and for τ_c, only events within $0.00006\ 1/\text{ns} < \tau_c < 0.00016\ 1/\text{ns}$ should be kept. The number of events rejected by these two cuts will be smaller than expected from Th-228 measurements. For the reactor data, the count rate is lower than for Th-228 and therefore, the number of events happening in the exponential decay will be smaller, too. In addition, after applying the μ-veto, the number of saturation events will be smaller since μ events contribute to the saturation events. Nevertheless, these cuts can be applied to the data.

For the parameters t_0 and P_0, it is harder to define quality cuts without the necessity to calculate a corresponding cut efficiency. No obvious cuts can be found for the high energy part of the parameters. In the low energy part, cuts could be applied to reject noise. However, the energy of the noise is mainly below $E < 200$ eV. Below this energy, the fit does not work anyway (see section 4.4.3) and thus, these cuts are unnecessary. Especially, for t_0 one needs to be careful because also wrongly triggered events appear in the noise regions. All in all, no quality cuts will be applied for these two parameters. For the long term, one could think of possible cuts for these two parameters and calculate the corresponding efficiencies.

The reduction power of these quality cuts is estimated for Th-228 and reactor-ON data. For the Th-228 measurement, the energy spectrum before and after the quality cuts can be seen in Fig. 3.29. It can be seen that the reduction is quite large, especially for lower energies. By far, the largest contribution of the cut comes from the error bins. For the reactor-ON data, a total of ~ 88 days is used. The reduction power of this cut for different energy regions can be found in Tab. 3.4. It can be seen that the reduction is relatively

[2] Quality cuts are used to 'clean' the data from artefacts, etc. In contrast, a PSD-cut is based on the different topologies of the pulse, which have a physical origin.

Table 3.4.: Possible reduction due to the application of the quality cuts. The used measurement is done with the C1 detector and contains ~ 88 days of reactor-ON data.

energy range [keV_{ee}]	reduction due to quality cut [%]
$0 - 0.3$	3.4
$0.3 - 2$	1.2
$2 - 10.1$	1.4
$10.1 - 10.6$	0.12
$10.6 - 20$	3.9
$20 - 32$	0.7

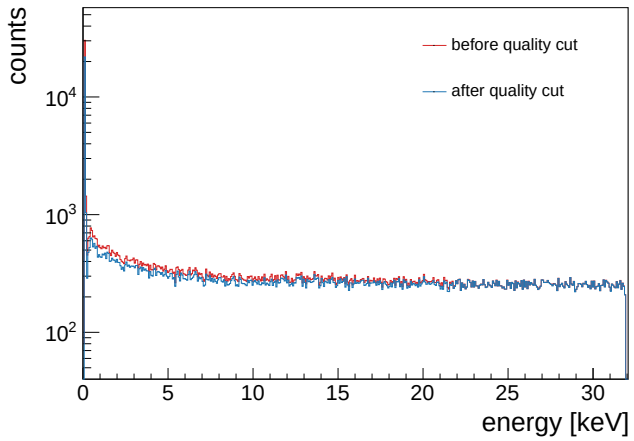

Figure 3.29.: Th-228 spectrum before (red) and after (blue) the quality cuts. For this spectrum, multiple calibration measurements for C1 during RUN-5 are used.

small and between 0.12% and 3.9%. Nevertheless, this cut will be applied to the data. Moreover, it can be seen in this table that the reduction for the last two energy ranges is quite different. A reason for this observation is not found yet.

Chapter 4.

Results and Application

In this chapter, the application of the rise time fit to Th-228 and reactor-ON data is shown and a new method to calculate the PSD-cut efficiencies will be introduced. For the reactor-ON data, the first three month of data collection in RUN-5 (May - August 2021) are used. As before, the C1 detector is used as a benchmark detector. First, the stability of the τ and τ_c parameter is investigated (section 4.1), and the possibility to use the pulse shape analysis as a monitoring tool for the performance of the preamplifier is demonstrated (section 4.2). Then, the application of the rise time fit to a Th-228 measurement is shown, including a comparison of the results to a MC simulation (section 4.3). Afterwards, a detailed pulser study is described, allowing to determine the lower threshold of the rise time fit in the sub-keV region (section 4.4). The method for the PSD-cut efficiency calculation, including the systematic uncertainties, is explained (section 4.5), and the rise time fit and PSD-cut is applied to reactor-ON data (section 4.6). In the end, the "by-product" of the rise time fit, the discrimination between SSE and MSE above 100 keV, is shown (section 4.7).

4.1. Stability of the τ and τ_c Parameter

In this section, we investigate the time stability of the τ and τ_c parameter, which is crucial for the PSD. First, we will look at the τ_c parameter. The parameter is fixed to a certain value for energies below $E < 8000$ ADC (see section 3.2.3). In order to be able to use the same value for τ_c over the complete measurement period, stability over time is necessary. Reactor-ON data in the energy range of $E = 15 - 32$ keV will be used to check if the parameter is stable. For the energy, the same range is chosen as for the initial calculation of the fixed τ_c values. Only the TRP veto and not the μ-veto is applied for the estimation of τ_c, to increase the statistics per measurement. The normal pulse peak of the τ_c-distribution is fitted by a Gaussian function for each measurement and the mean value of the fit is plotted against the time. For the error bars, only the statistical uncertainties are used. The stability plot for the C1 detector can be seen in Fig. 4.1. Figure 4.1 shows that the τ_c value for C1 is very stable over time. In addition, the τ_c value is always compatible with the value used as the fixed τ_c parameter at low energies, $\tau_c = 0.000131$ 1/ns. The stability plots of the other three detectors can be found in the appendix in Fig. B.1. Also, for C3 and C4, the τ_c value is stable and always compatible with the fixed values at low energy (see Tab. 3.2). The τ_c values for the C2 detector are stable, too. However, in the C2 case, the τ_c value is closer to a value of $\tau_c = 0.000130$ 1/ns than to the value estimated in section 3.2.3 ($\tau_c = 0.000131$ 1/ns) for some measurements.

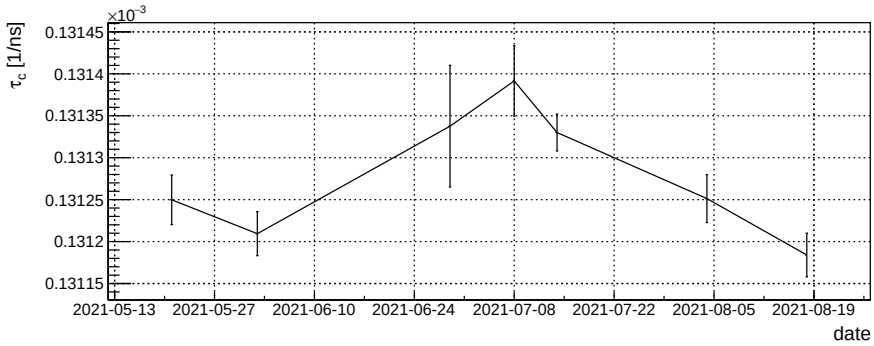

Figure 4.1.: Stability of the τ_c parameter over time for the C1 detector. For the estimation of the parameter, reactor-ON data is used. On the x-axis, the starting date of each measurement is plotted.

The deviation is on the percent level and was considered to be negligible. The stability of the τ_c parameter should be monitored in the future, as well.
Next, we will have a look at the stability of the τ parameter. The stability of the τ parameter over time is important to be able to apply the same PSD-cut to the complete reactor-ON and reactor-OFF data. Therefore, the parameter needs to be stable for the time of around 1.5 years. If this were not the case, the PSD-cut would need a time dependence, introducing new systematic uncertainties. Since the normal pulse population should survive the PSD-cut, the stability of this population will be monitored. The bi-weakly performed Th-228 calibration measurements are ideal for the τ stability monitoring. As before, the TRP veto is applied to the data. For the estimation of the τ parameter stability, the energy range of 25 keV $\leq E \leq$ 32 keV is used. In this energy range, the higher and lower normal populations can be distinguished. The higher population is closer to the PSD-cut and thus is more interesting for stability monitoring. In the τ-distribution, the peak corresponding to the higher normal pulse population is fitted by a Gaussian function and the mean value is plotted against the date of the calibration measurement. For the error bar, only the statistical uncertainty is used. A plot showing the stability of τ for the C1 detector can be seen in Fig. 4.2. The plot shows that for C1, the τ value is stable and only variates in a range of around 0.4 ns, corresponding to a variation of approximately 0.3% relative to the mean value. The stability plots for the other detectors can be found in the appendix in Fig. B.2. Also, the detectors C3 and C4 show only small variations. The C3 detector shows a variation in the range of 1.6 ns, corresponding to a variation of around 0.8% relative to the mean value and the C4 detector has a variation of about 0.6 ns or 0.4% relative to the mean value. However, for both detectors, it slightly looks like the τ parameter drifts towards larger values. The C2 detector shows a clear drift towards larger τ values, going over a region of around 1.5 ns, corresponding to 0.8% relative to the first data point. In general, monitoring the stability of the τ parameter is of paramount importance for the success of the PSD method.

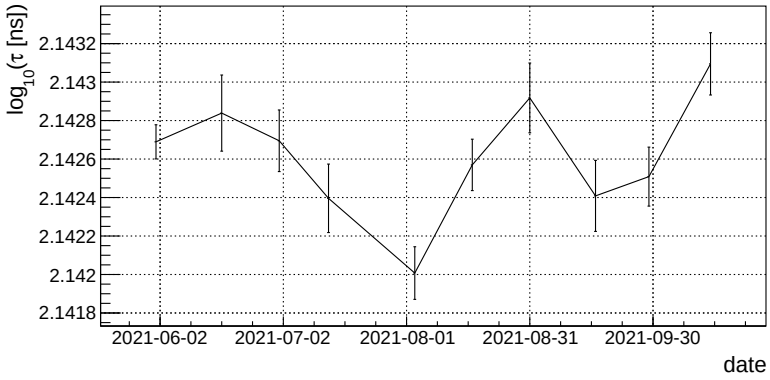

Figure 4.2.: Stability of the τ parameter over time for the C1 detector. For the estimation of the parameter, Th-228 calibration data is used. On the x-axis, the date of each measurement is plotted.

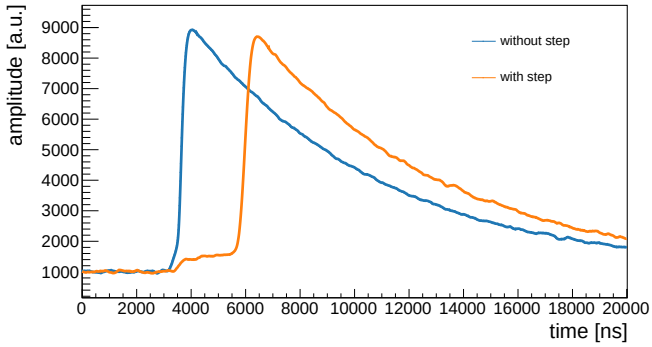

Figure 4.3.: Two example pulses of the C2 detector before the pumping of the cryostat and preamplifier tuning. The blue pulse is a regular normal pulse and the orange one is a normal pulse with a step included.

4.2. Rise Time Fit as Analysis Tool for Preamplifier and Detector Performance

The rise time fit can be utilized as a tool for monitoring the performance of the preamplifier and of the Ge diode, in addition to the main usage for PSD. In general, this can be done by looking for anomalies in the fit parameter distributions and especially by looking at the τ vs. energy plots. In this section, two examples from the commissioning of RUN-5 are shown to illustrate this application.

Example C2: Before the start of RUN-5, some normal pulses from the C2 detector had a step in the recorded pulse shape. This feature is unwanted and should not be confused with the pre-increase (see section 2.4.1). In Fig. 4.3, two example pulses from C2 are shown. One of the pulses is a regular normal pulse and the other one has a step included in the pulse shape. The pulses with an additional step are visible as an additional population in the τ vs. energy plot. An example plot can be found in Fig. 4.4a. In this figure, four populations are visible. The population with the highest rise time (values around

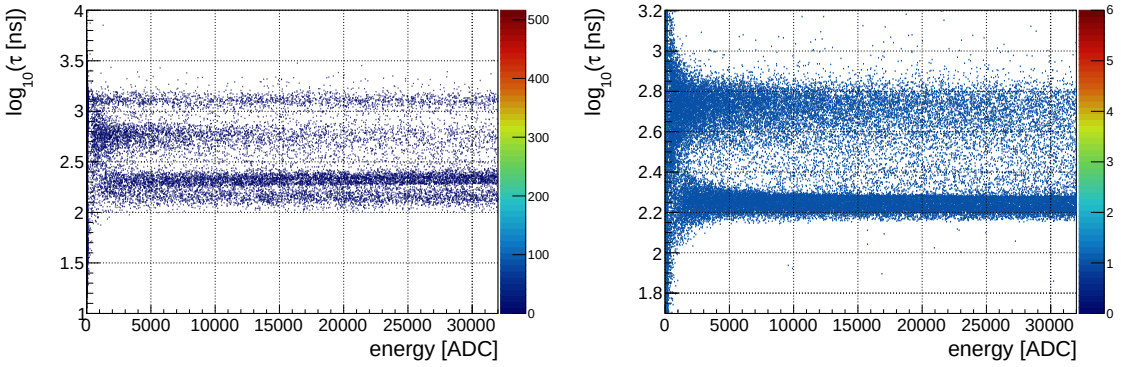

(a) **(b)**

Figure 4.4.: Two τ vs. energy plots for Th-228 measurements with the C2 detector in the low energy range $E \lesssim 32$ keV. The measurement in figure a) was recorded before the pumping of the cryostat and the preamplifier tuning. Therefore, some normal pulses have an unwanted additional step. The measurement in figure b) was recorded after the pumping of the cryostat and preamplifier tuning and looks acceptable again. The colour bar indicates for each plot the number of events per bin.

$\log_{10}(\tau) = 3.1\ \log_{10}(\text{ns})$) contains mostly saturation events. Slow pulses are collected in the population around values of $\log_{10}(\tau) = 2.7 - 2.8\ \log_{10}(\text{ns})$ and the two populations with the lowest rise times contain normal pulses with and without the additional steps. The normal pulses with additional step are included in the population with the larger τ values. This does not only show that normal pulses with an additional step exist, but it also allows quantifying the ratio of normal pulses with and without the step. The ratio could be used to understand the origin of the step by comparing it to theoretical values for possible origins. However, no explanation was found. After a pumping of the cryostat and preamplifier tuning for C2, the additional step mainly disappeared. Also, the τ vs. energy plot looks normal again. In Fig. 4.4b, the normal-looking τ vs. energy plot is shown.

Example C3: During the commissioning of RUN-5, it was observed that the pulses of the C3 detector look different compared to pulses of the C1 detector. A rise time vs. energy plot of the C3 detector can be found in Fig. 4.5a. The used measurement is recorded in the high energy regime $E \lesssim 900$ keV. The high energy measurement is used due to the lack of low energy data before the preamplifier tuning of C3. However, the effect of the preamplifier tuning can also be seen by using this measurement. In this figure, three horizontal populations are visible. The normal and slow pulse population are located around a value of $\log_{10}(\tau) = 3\ \log_{10}(\text{ns})$. Especially, the normal pulse population has way larger τ values than expected and is very close to the slow pulse population. Therefore, the figure shows that something is not working correctly. In order to change the performance, the preamplifier settings were changed. After these changes, the rise time distribution looks normal again and is shown in Fig. 4.5b. The measurement shown in this figure is

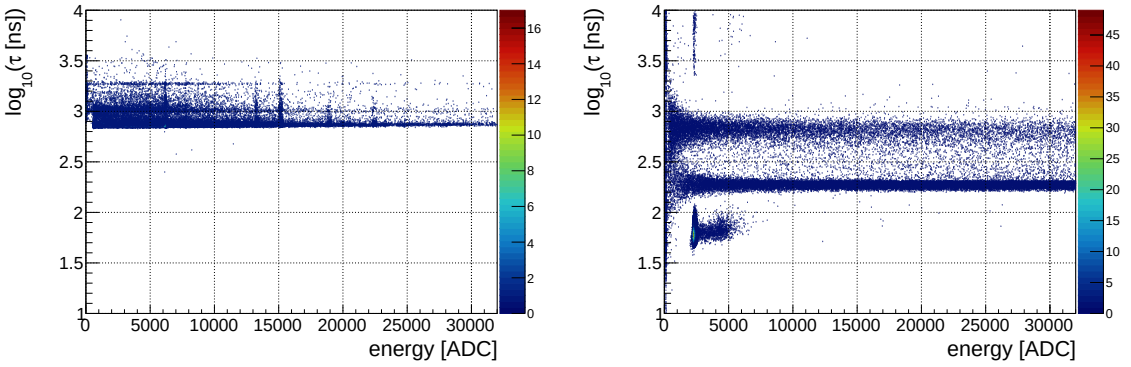

(a) **(b)**

Figure 4.5.: Two τ vs. energy plots for Th-228 measurements with the C3 detector. Figure a) shows a high energy measurement $E \lesssim 900$ keV before the preamplifier tuning of C3. Figure b) shows a low energy measurement $E \lesssim 32$ keV after the preamplifier tuning. The 'blob' visible at energies below $E < 5000$ ADC and rise time values around $\log_{10}(\tau) = 1.5\ \log_{10}(\text{ns})$ comes from events correlated to the TRP resets and can be rejected by the TRP veto. The vertical band at energies of $E \approx 2500$ ADC and rise time values of $\log_{10}(\tau) \geq 3.3\ \log_{10}(\text{ns})$ mainly contains saturation events and events happening in the exponential decay of a previous pulse. The colour bar indicates for each plot the number of events per bin.

conducted in the low energy range ($E \lesssim 32$ keV). Nonetheless, the position of the normal pulse population can be compared to the one from the high energy range because it is assumed that τ is energy-independent. Overall, the τ vs. energy plot shows that the preamplifier is working correctly again and the plot helped determine if the settings were chosen properly.
In addition to the usual visual inspection of a few selected pulses, the rise time fit can help to identify and quantify unusual behaviour of the preamplifier and the detector. Moreover, the parameter distributions can help monitor the changes in time.

4.3. Application of the Rise Time Fit to Th-228 Data

In section 3.1.3, a visual inspection of the τ vs. energy plot showed that the two main populations could be assigned to normal and slow pulses. Now, in this section, these findings are cross-checked by looking at a simple estimation based on the attenuation law (see eq. 2.11) and a comparison with a MC simulation. Afterwards, τ-distributions for Th-228 measurements will be shown and discussed.

Estimation based on the attenuation law: In the following, we will perform a rough estimation for the percentage of normal and slow pulses expected in the detector by using the attenuation law. The theoretical estimate will then be compared to the percentage

Table 4.1.: The results of the rough estimation for the expected percentage of normal (b_{theo}) and slow pulses (s_{theo}) for the C1 detector using the attenuation law. The energy ranges (E) and attenuation coefficient (μ) used in the analysis are also shown. In [14], the mass attenuation coefficient is given, meaning that the values need to be multiplied by the density of germanium ($\rho_{\text{Ge}} = 5.32$ g/cm^3 [36]) to get the attenuation coefficient. For the estimation of the experimentally determined percentage of normal (b_{exp}) and slow pulses (s_{exp}), a Th-228 measurement performed with the C1 detector was used.

E [keV]	μ [1/cm]	b_{theo}	s_{theo}	b_{exp}	s_{exp}
$57 - 63$	10.7684	0.806	0.194	0.768	0.232
$76 - 84$	5.0574	0.904	0.096	0.819	0.181

estimated from a Th-228 measurement. For the estimation, we assume, that all γ-rays from the same source deposit their total energy in the bulk volume or in the transition layer, and only interact once. The percentage b_{theo} of γ-rays reaching the bulk volume and the percentage s_{theo} of γ-rays stopped in the transition layer can be calculated with the attenuation law (see eq. 2.11) as follows:

$$b_{\text{theo}} = \frac{I(\lambda_{\text{trans}})}{I_0} = e^{-\mu(E)\lambda_{\text{trans}}} \tag{4.1}$$

$$s_{\text{theo}} = 1 - b_{\text{theo}}, \tag{4.2}$$

where λ_{trans} is the thickness of the transition layer and I_0 the intensity of γ-rays after the dead layer. The starting intensity I_0 is set after the dead layer because all γ-rays being detected in the transition layer or in the active volume need to pass through the dead layer first. For the thickness of the transition layer, the value of $\lambda_{\text{trans}} = 0.20$ mm [39] is used. The attenuation coefficient is taken from [14] at the energies used for the comparison. In order to avoid a too significant influence from Compton scattering and thus from multiple scattering, only two energy regions below 100 keV are used. Another criterion is that the energy range is above $E \approx 50$ keV, such that the γ-rays from the Th-228 source can penetrate the Cu Cryostat and reach the detector. The energy regions are considered in a 5% range around the values of $E = 60$ keV and $E = 80$ keV. Only a small energy region is used to justify the assumption of a constant attenuation coefficient in the region. The energy regions, corresponding attenuation coefficients and theoretically calculated value for s_{theo} and b_{theo} are reported in Tab. 4.1.

For the estimation of the experimental values, a Th-228 measurement after the application of the TRP veto is used. The number of normal and slow pulses is estimated by counting the events in specific τ regions. The normal pulse region is chosen as $1\ \log_{10}(\text{ns}) < \log_{10}(\tau) < 2.1\ \log_{10}(\text{ns})$ and the slow pulse region is $2.1\ \log_{10}(\text{ns}) < \log_{10}(\tau) < 4\ \log_{10}(\text{ns})$. From the number of events, the percentages of normal b_{exp} and slow pulses s_{exp} are calculated. Both values are shown in Tab. 4.1

Comparing the experimental and theoretical calculated values, one finds that they are

Table 4.2.: All quantities necessary for the MC simulation comparison. N and S are the number of normal and slow pulses extracted from the Th-228 measurement and 'total' means all events between $1\,\log_{10}(\text{ns}) < \log_{10}(\tau) < 4\,\log_{10}(\text{ns})$. The MC values are kindly provided by J. Hakenmüller and give the ratio of slow pulse to normal plus slow pulses.

E [keV]	$\Delta\log_{10}(\tau)$ [$\log_{10}$(ns)] normal pulses	$\Delta\log_{10}(\tau)$ [$\log_{10}$(ns)] slow pulses	$\left(\frac{\text{S}}{\text{S+N}}\right)_{\text{exp}}$	$\left(\frac{\text{S}}{\text{total}}\right)_{\text{exp}}$	$\left(\frac{S}{S+N}\right)_{\text{MC}}$
$2-6$	$1-2.2580$	$2.6410-2.9937$	0.472	0.455	0.45
$6-12$	$1-2.1909$	$2.6666-2.9627$	0.347	0.325	0.29
$15-20$	$1-2.1687$	$2.6528-2.9630$	0.245	0.224	0.21
$25-30$	$1-2.1603$	$2.6139-2.9790$	0.213	0.191	0.19

in the same ballpark. Some possible problems and simplifications of this estimation are described below. First, the attenuation coefficient is a function of energy and in the calculation, it was assumed to be constant in the energy range. From [14], it can be estimated that the change of the attenuation coefficient is about $\sim 28-31\%$ over the chosen 5% energy region. Another simplification is that the possibility of multiple interactions is completely neglected. The influence of multiple scattering could explain why the deviation for the higher energy region is larger. Additionally, the uncertainty of the transition layer thickness is neglected in the calculation as well. Also, it was assumed that the γ-rays only interact once and deposit their complete energy. Lastly, the normal and slow pulse regions for the experimental values were only estimated by eye.
All in all, the simple estimate supports the hypotheses from the visual inspection that the population with the larger rise time comes from slow pulses, while the population with the shorter rise time comes from normal pulses.

MC comparison: A more refined cross-check, accounting for example for the energy dependence of the attenuation coefficient, is a comparison of the number of normal and slow pulse events with a MC simulation. For the comparison, J. Hakenmüller kindly provided the ratio of slow pulses to the sum of normal and slow pulses from a MC simulation for a Th-228 measurement with C1. These numbers can be found in Tab. 4.2. Before starting with the comparison, we need to check if the background of the experiment can be neglected for a Th-228 measurement. To do so, the ratio of the number of background to Th-228 events can be used. Since the reactor is running during all Th-228 calibrations, reactor-ON data is the 'background data' in the current analysis. The ratio is smaller than 0.001 for energies above 10 keV and below 0.002 for energies between 500 eV and 10 keV. As a result, the background events can be neglected for the MC comparison. For the comparison, all low energy Th-228 calibration measurements performed with C1 between 01.06.2021 and 17.08.2021 are used. To be able to separate the normal and slow pulse population clearly, the comparison is only performed down to energies of 2 keV. The normal and slow pulse regions in the τ-distributions are estimated by fitting a Gaussian function to each peak for

every energy region. For the slow pulse population, the τ region is defined by $\mu \pm 3\sigma$. In the case of the normal pulse population, only the higher population is fitted and from this, the upper bound of the region is calculated by $\mu + 3\sigma$. The lower bound is set to one for the complete comparison. The energy ranges and τ regions are listed in Tab. 4.2. For the comparison with the MC simulation, the ratio of slow pulses S to the sum of normal and slow pulses (N+S) is calculated and are summarized in Tab. 4.2. Comparing the values to the MC simulation, we can see that the experimentally determined values already agree at the 15% level with the MC predicted values. However, in this case, all events between the normal and slow pulse population are neglected. If the ratio of slow pulses to the total number of pulses (all events within $1\log_{10}(\text{ns}) < \log_{10}(\tau) < 4\log_{10}(\text{ns})$) is used for the comparison, the numbers fit even better to the MC simulation ($\lesssim$ 5% level, except 6-12 keV: 10% level). All in all, the numbers fit good according to this first comparison attempt. The energy range from 6-12 keV shows the largest deviation from the MC simulation.
In the following, possible explanations for the difference between data and MC are described. First, events in the bulk volume with more than one energy deposition will have a larger τ parameter than the SSE events (see section: 4.7). Therefore, they will be above the normal pulse population in τ space and thus will be not counted as a normal pulse. However, the MC simulation will classify such an event as a normal pulse and thus it can introduce a difference. Another problem could be that the MC simulation will classify an event as slow pulse if a small energy deposition (e.g. 5 eV) takes place in the transition layer. Such an event might appear in the normal pulse population of the τ parameter if the energy deposition in the transition layer is so small that it does not influence the pulse shape significantly. Also, the transition layer is implemented in the MC simulation as a rectangle with sharp corners. However, in reality, it could be that the transition layer is a bit thicker in the corners, leading to differences between the MC simulation and the data. In general, more investigations are needed to determine where the differences between the MC simulation and the data comes from.
In conclusion, the values from the MC simulation and the measured data agree well for a first comparison. Therefore, the MC simulation supports the assumption that the rise time fit allows the separation of physical events, generated either in the transition layer or in the bulk of the Ge diode. More investigations are needed to resolve the differences between simulation and measurement.

In the following, distributions of the rise time parameter τ for Th-228 measurements are shown and discussed. In Fig. 4.6, τ distributions for different energies for the C1 detector are shown. It is clearly visible that the two peaks can still be separated in the energy range of 1-2 keV. At lower energies, these two peaks mix stronger and it is more challenging to separate them. Figure 4.6 shows that the fit is still able to work and can be used to discriminate normal and slow pulses around energies of 1 keV, which is very important since the region of interest for the CEνNS analysis goes down to $\sim$ 300 keV. A determination of the lower energy threshold of the fit is shown in section 4.4.3.

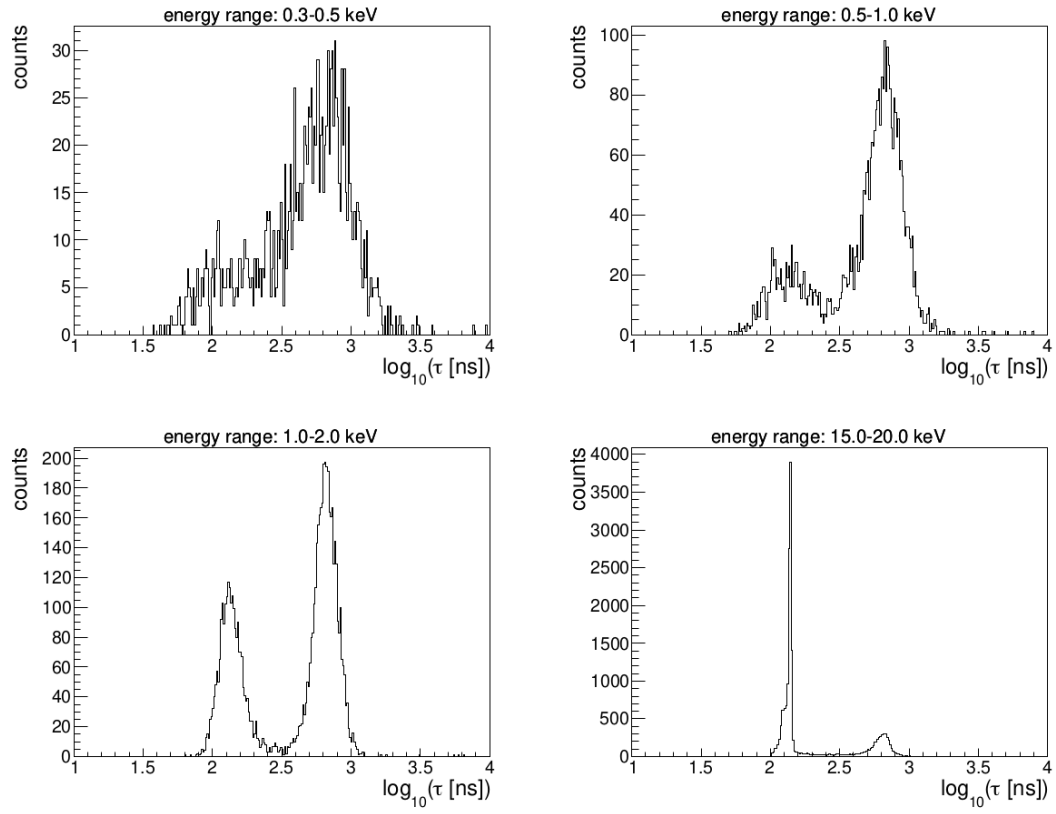

Figure 4.6.: $\log_{10}(\tau)$-distributions for the C1 detector at different energies. For the plots, all Th-228 calibration measurements between 01.06.2021 and 17.08.2021 are used.

In Fig. B.3, B.4 and B.5, multiple τ-distributions are shown at different energies for C2-C4. The position of the populations in τ space depends on the geometry, on the electric field configuration of the detector (see section 2.3.2) and on the preamplifier settings (see section 4.2). Moreover, the discriminating power of τ is different. For example, comparing the τ-distribution of C1 and C2 in the energy range of 0.5 - 1 keV shows that the discriminating power of τ is larger for C1.

In the high energy τ-distribution (15-20 keV, Fig. 4.6), one can see the two subpopulations of the normal pulse peak. The lower population looks like a tail towards lower τ values, while the higher population is a clear peak. From a simple simulation (see section 2.4.1), we know that the two subpopulations probably come from different interaction points inside the bulk of the Ge diode. Events in the lower population occur closer to the p+ contact of the diode, in contrast to events from the higher population. It would be interesting to calculate the volume ratio of the areas inside the diode where the interaction happens by taking the ratio of events from the higher and lower population. The ratio could, e.g. help to validate a pulse shape simulation. However, the estimation cannot be done with the Th-228 data shown in Fig. 4.6 since the γ-rays do not interact homogeneously inside the diode, but more events happen in the outer layers, especially at low energies. In addition, the Th-228 source is located centred above all four detectors, with the p+ contact of

the detectors pointing towards the source. These two points lead to more events in the lower population, making it impossible to use the low energy Th-228 measurement for the calculation. A more homogenous distribution of the interactions in the diode could be achieved by going to higher energies because then the γ-rays are penetrating deeper into the diode. Another option is to use a pulse shape simulation or the $\sim$ 10.4 keV Ge line to determine this volume ratio. An estimation of this ratio using the latter option is shown in section 4.5.1.

4.4. Pulser Studies

In order to estimate a lower threshold for the rise time fit and to calculate the cut efficiency of a PSD-cut and its associated systematic uncertainty, extensive pulser studies were performed. Again, the C1 detector is used as a benchmark detector. The analysis described in this section can be applied to the other detectors in a similar way. First, the experimental setup of the pulser studies is described (section 4.4.1). Then, the resulting parameter distributions are shown and limitations of these measurements are discussed (section 4.4.2). In the end, the lower energy threshold of the rise time fit is determined (section 4.4.3). The calculation of the cut efficiency and systematic uncertainty is shown in the next section (section 4.5.1).

4.4.1. Setup

For the pulser studies, a forced trigger is used, meaning an 'external trigger' signal generated by the pulser forces the recording of an event by the DAQ. The forced trigger allows investigating pulses with a similar amplitude compared to the height of the noise. With a free trigger, the analysis would not be possible because it is hard to tell if the recorded data shows a pulse or noise, at very low energies. In contrast, the setup with a forced trigger can be chosen in a way that all recorded events correspond to an injected test pulse, also at very low energies.
For the pulser studies, the Tektronix AFG 3252 Dual Channel Arbitrary/Function Generator [52] was used. The pulser has two output channels, which were both used for the forced trigger configuration. Both channels can be coupled in frequency, such that they send out signals at the same time. A schematic view of the measurement setup can be found in Fig. 4.7. The signal coming from the second pulser channel was used as the trigger signal, meaning that the signal goes directly to the CAEN without going through the detector. An oscilloscope was used to monitor the input pulse shape and frequency. Additionally, the CAEN was set up in a way that if CH5 triggers, it forces the acquisition of the physical channel 0-3 (CH0, CH1, CH2, CH3). Channel 0-3 were used as the signal channels. The signal from the first pulser channel was split and sent through the electronic chain of

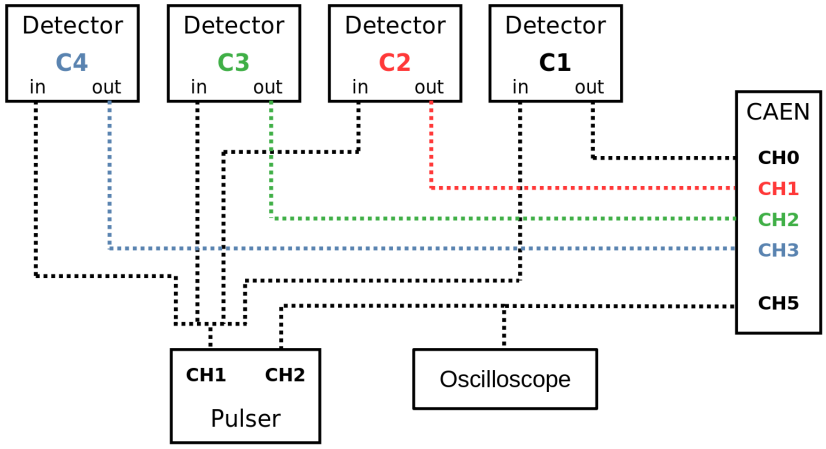

Figure 4.7.: Schematic view of the configuration used for the pulser studies. The dotted lines represent signal cables.

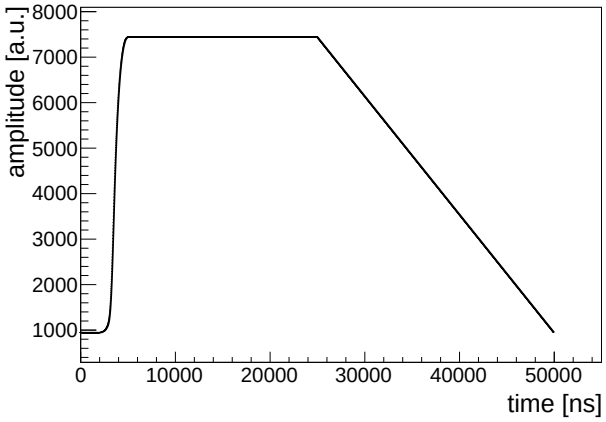

Figure 4.8.: Example of the pulses used as an input for the pulser studies. The shown pulse is created from the mean pulse of the slow pulse population from a Th-228 measurement with the C1 detector.

the four detectors C1-C4. Since the two different pulser channels were used for different purposes, the amplitudes of the trigger and signal pulses can have different amplitudes. As a result, the trigger signal can always have a large amplitude, ensuring that the trigger efficiency of the CAEN is 100%, while the amplitude of the signal pulse can be lowered to very small energies (amplitudes). Due to the forced trigger configuration, we know that in each recorded event, a pulse and not noise is shown.

In order to mimic the physical signal as good as possible, real pulses were used as an input pulse shape for the pulser. These pulses were used for the trigger and signal. In the following, it will be shortly explained how these real pulses are generated. First, mean pulses in the energy range of $E \approx 15 - 16$ keV were calculated for the three physical populations (slow pulse, higher normal pulse and lower normal pulse). A relatively high energy range was chosen for the mean pulses to minimize the influence of noise on the pulses shape. Afterwards, the three pulses are transformed such that the pulses stay flat

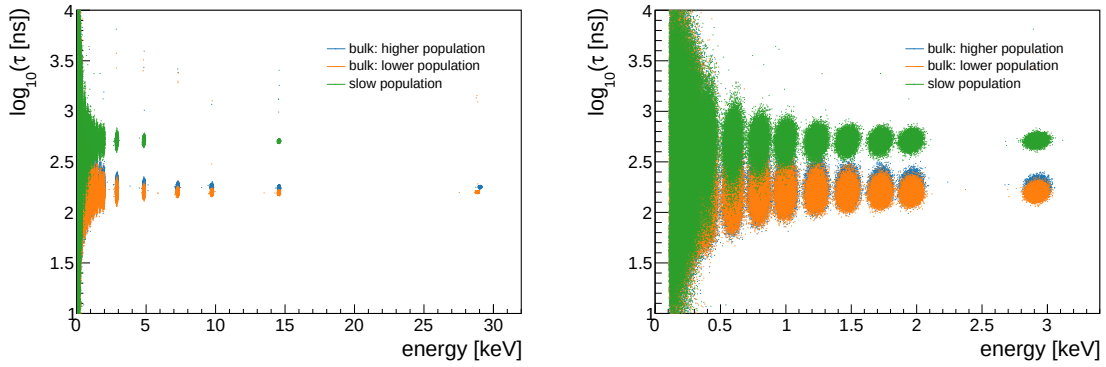

(a) (b)

Figure 4.9.: Result of the pulser measurement with a forced trigger performed with C1. The input pulses of the pulser are generated from a Th-228 measurement. Figure a) shows the complete measurement and figure b) shows the same measurement zoomed into the low energy range.

after they reach their maximum and go slowly back to the baseline after a total time of $t = 25000$ ns. This replaces exponential decay of the mean pulses. Otherwise, the AC coupling response would be accounted twice, resulting in an overall different pulse shape compared to the physical pulses. The decay back to the baseline is chosen relatively long to avoid the CAEN triggering on this decay. An example of such a pulse can be seen in Fig. 4.8. These modified mean pulses were inserted into the pulser and used as the input pulses for the pulser studies. Since the pulses were created with one fixed height only, they are scaled by the pulser to simulate different energies. It was checked that the physical pulses scale in the same way. As a result, it was found that this is the case. Also, this was expected (see section 2.3.2) because the charge (proportional to the energy) is only a scaling factor.

4.4.2. Results

Even though all detectors were connected and measuring during the pulser studies, only the results of the C1 detector are shown here. There are two main reasons for this. First, the measured energy points were optimized for the C1 detector. For the other three detectors, the measured points are at slightly different energies. Secondly, the input pulses for the pulser were calculated from a measurement with the C1 detector.
An overview of the measured energy points can be seen in Fig. 4.9a and 4.9b in the form of a τ vs. energy plot. The blue and orange data points correspond to the measurement where the mean pulse from the higher and lower normal population was used as an input and for the green data points, the mean slow pulse was used. It can be seen that the populations are in the same ordering as one would expect (slow pulses largest τ parameter and pulses from the lower normal population smallest τ parameter) and that the normal and slow populations are clearly separated until energies of around 1.5 keV. In addition, it is visible

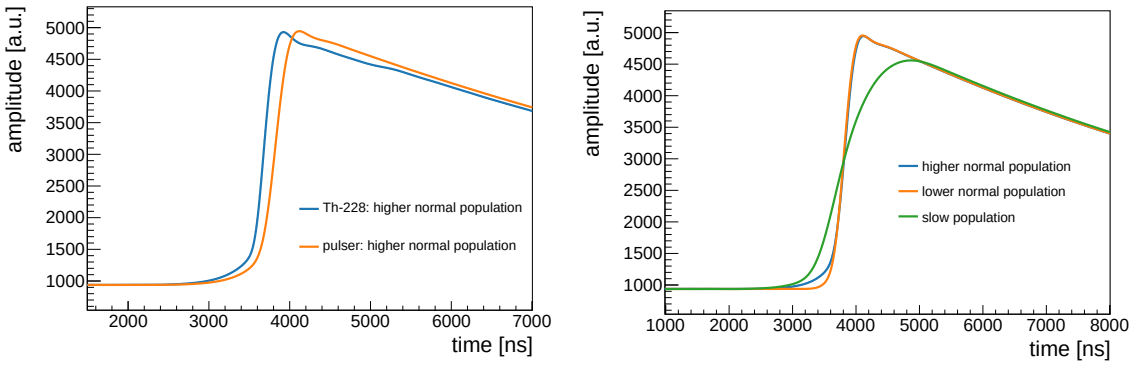

(a) **(b)**

Figure 4.10.: In figure a) a comparison of the mean pulse used to calculate the input pulse for the pulser to the resulting mean pulse from the pulser measurement is shown. Figure b) shows the resulting mean pulses from the pulser measurement for all three populations. The C1 detector was used for the shown measurements and for the calculation of the mean pulses, events with an energy around ~ 15 keV were taken.

that the two normal pulse populations mix for lower energies. That makes sense because, at lower energies, the pre-increase is hidden in the noise. However, the three populations are not centred around the same τ values as expected from the input pulses. The normal pulse populations are shifted to a bit larger values, while the slow pulse population is shifted to smaller values. For example, the mean pulse for the lower normal population is calculated from pulses with a τ parameter between $\log_{10}(\tau) = 2.0 - 2.12$ $\log_{10}(\text{ns})$. But the corresponding pulser population has a mean value of $\log_{10}(\tau) = 2.19$ $\log_{10}(\text{ns})$. Comparing a mean pulse from the Th-228 measurement (used to create the pulser pulses) to a mean pulse from the pulser measurement shows that the problem does not come from the fit but the data. The comparison is shown in Fig. 4.10a. In this figure, the normal higher population was chosen as an example. It is clearly visible that the rise time of the pulse from the pulser is larger, leading to larger τ values. The difference can be explained by the electronic response of the preamplifier and DAQ. The input pulses created for the pulser already include the electronic response. Since they are sent through the preamplifier and DAQ, the electronic response is added again. It would be interesting to calculate the input pulse without the electronic response to mimic the physical measurements better. In order to find a description of the electronic response, more investigations are needed. Another option to achieve a better description is to use pulses from a simulation as an input for the pulser. Nevertheless, looking at a comparison of the mean pulses from all three populations from the pulser measurement, it can be seen that the important features are recreated: different rise times for normal and slow pulses, a pre-increase for the higher normal population, the same form for the lower and higher population, except the pre-increase. The comparison is shown in Fig. 4.10b.

Most of the other fit parameters show no peculiarities. In addition, features of the

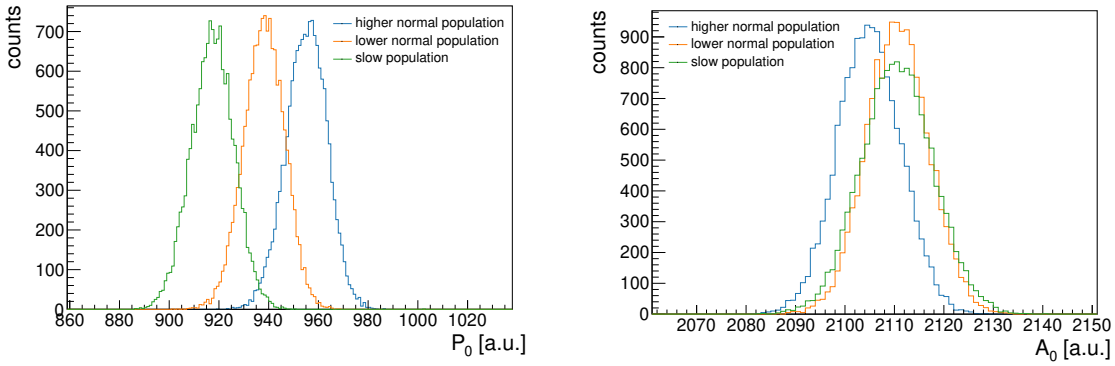

(a) (b)

Figure 4.11.: Parameter distribution for P_0 and A_0 in the high energy range of the pulser measurement. In figure a) the P_0-distribution and in figure b) the A_0-distribution is shown. Both distributions are at an energy of $E \approx 15$ keV and are recorded with the C1 detector.

parameter distributions discussed in section 3.2.4 are reproduced with the pulser measurement. As an example, Fig. 4.11a shows a P_0-distribution for a high energy point (~ 15 keV). In the plot, it can be seen that the distributions of the three populations have different mean values. The ordering of the peaks is the same, as discussed in section 3.2.4 for the high energy case. At lower energies, the peaks have a similar mean value, as expected from the low energy case discussed in section 3.2.4. For the measurement at an energy of ~ 15 keV, the A_0 parameter shows a peculiarity. The corresponding plot is shown in Fig. 4.11b. The A_0-distribution for the higher population has a smaller mean value than for the lower population. A possible reason could be related to the different P_0 values. The maximal point the fit function would reach without the exponential decay is $f_{\max} = 2A_0 + P_0$. Since the maximal amplitude $f_{\max}$ is fixed by the energy of the event, a larger or smaller P_0 parameter would lead to a smaller or larger A_0 parameter. The difference seen in the P_0 parameter has the correct order to make up the majority of the A_0 difference, but it is not large enough to completely explain it. Additionally, it is interesting that the lower and slow populations have nearly the same mean value. Following the argument above, the slow pulse peak should have a higher mean value than the lower population. An explanation for this peculiarity is not found yet. However, the slow pulse has the strongest influence from the electronic response on the shape. Maybe, some effect regarding the electronic response cancels the effect described above.

4.4.3. Lower Energy Threshold for the Rise Time Fit

The pulser measurement can be used to determine the lowest energy up to which the fit method can be used to distinguish between normal and slow pulses. In the forced trigger configuration, we are able to reduce the pulse height without losing trigger efficiency, making it possible to study pulses with a similar height compared to the noise. Moreover,

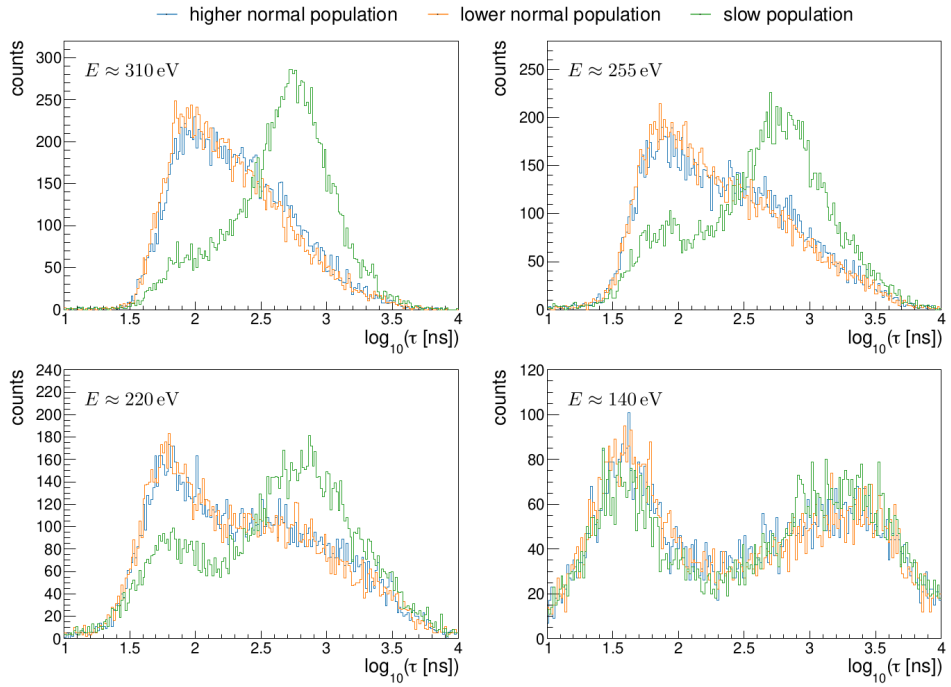

Figure 4.12.: τ-distributions of all three populations at different energies for the pulser measurement with C1. Only distributions at low energies are shown to find the lower threshold of the fit.

with the pulser, we know if an injected event is a normal or slow pulse. In order to determine the lower threshold, the τ distributions of the lowest energy points are used. The distributions for the energy points at $E \approx 310$, 255, 220, 140 eV are shown in Fig. 4.12. In this figure, the τ-distributions of the three different populations are compared for each energy point. At all shown energies, the distribution of the lower and higher population look very similar. That makes sense because the only difference, the pre-increase, disappears for low energies due to the noise. As a result, the two normal pulse populations are basically the same at lower energies. More interesting is the comparison of the slow and normal distribution. In all shown plots, the two distributions overlap. However, for all energies except $E \approx 140$ eV, the form of the two distributions is different. It means that until energies of $E \approx 200$ eV, there is enough information in the data for the fit to create differently shaped τ-distributions. Of course, this will not allow discriminating normal and slow pulses with an efficiency of 100% and event by event, but a statistical separation is still possible. At lower energies, like, e.g. $E \approx 140$ eV, the fit method fails completely and it is impossible to distinguish between normal and slow pulses, the three populations basically look the same.

In conclusion, the rise time fit can be used down to energies of $E \approx 200$ eV. This fully includes the region of interest for the CEνNS analysis.

In the plot with the lowest energy shown in Fig. 4.12, two populations are still visible. These two populations come from events with a failed fit. The peak at lower τ values is created by the fit of noise. In this case, a small fluctuation of the noise is fitted. An

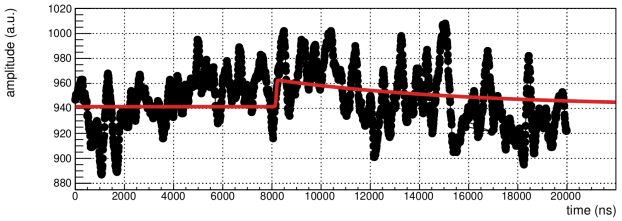

(a)

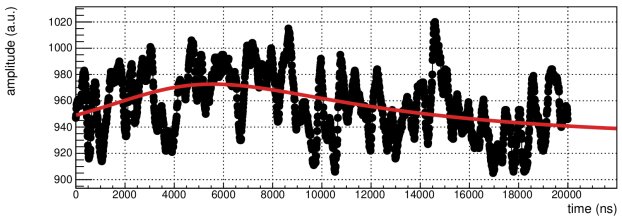

(b)

Figure 4.13.: Two examples for failed fits from the pulser measurement with the C1 detector. In figure a), a pulse is shown, where the increase of noise is fitted. Figure b) shows a pulse, where a function with a too large rise time is fitted to the data.

example pulse for fitted noise is shown in Fig. 4.13a. The peak with higher τ values mainly contains events, where a function with a very long rise time is fitted to the data. Again, this is a failed fit because the fitted pulse is definitely not what was sent in by the pulser. An example can be seen in Fig. 4.13b.
Also, in the distributions with energies above 200 eV, some events with a failed fit can be seen. For example, at the energies of $E \approx 255$ eV and $E \approx 220$ eV, the slow pulse population has a small contribution at low τ values, coming from events where noise is fitted. It shows that the fit starts to get problems at low energies but has not yet failed completely.
To illustrate why it is difficult to distinguish the pulses at these low energies, two example pulses are shown in the appendix in Fig. B.6. In this figure, it is visible that at low energies, the amplitude of the pulses has a similar height compared to the noise, making it hard to distinguish them from the noise. Moreover, the noise will wash out the difference between normal and slow pulses and thus decrease the discriminating power of τ.

4.5. Discrimination of Normal and Slow Pulses

The main goal of the pulse shape analysis is to reduce the background further by discriminating normal and slow pulses. At high energies, the normal and slow populations are clearly separated such that a full discrimination is possible. In contrast, at lower energies, the two populations start to mix and it is getting harder to distinguish them. The region of interest of the CONUS experiment is below 1 keV and thus lies in the region where the two

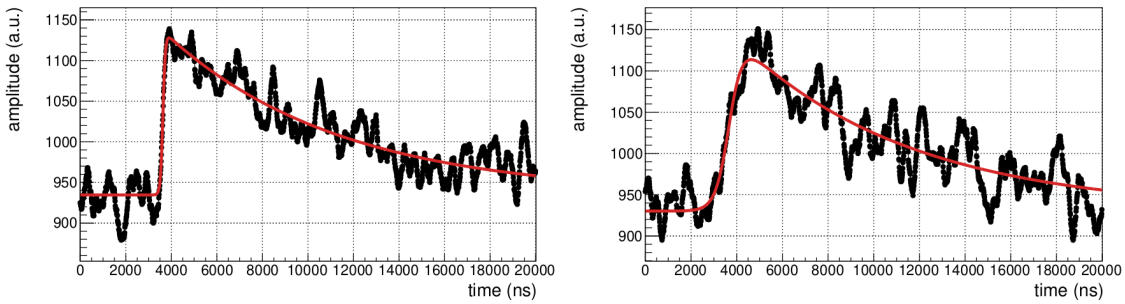

Figure 4.14.: Two example pulses from the low energy regime. The left pulse is a normal pulse, with a rise time of $\tau = (109 \pm 9)$ ns and an energy of $E \approx 0.72$ keV. The right pulse is a slow pulse with a rise time of $\tau = (589 \pm 27)$ ns and an energy of $E \approx 0.75$ keV. Both pulses are recorded with the C1 detector.

populations are hard to distinguish. Two example pulses, a normal and a slow pulse, with an energy below 1 keV, are shown in Fig. 4.14. Comparing the two pulses to high energy pulses (see Fig. 3.13) illustrates why it is harder to distinguish the two populations at low energies. In the low energy regime, the resulting rise time parameter τ can be influenced by the noise, meaning that the differences between normal and slow pulses are washed out. Additionally, at very low energies, the noise makes it harder for the fit to find the pulses. In the following, a method is described, developed to define a PSD-cut in the region of interest and calculate the associated cut efficiencies, including the systematic uncertainties (section 4.5.1). Afterwards, a procedure to identify the most beneficial cut efficiency for each energy will be introduced (section 4.5.2). Furthermore, an overview of the PSD-cut efficiency calculation implementation will be given in the appendix (section A.4). As before, the C1 detector is used as a benchmark detector.

4.5.1. Cut Efficiencies and Systematic Uncertainties

In this section, a newly developed method to calculate the efficiencies and systematic uncertainties for a PSD-cut is described. For this method, the pulser measurement with the forced trigger configuration, Th-228 data and the ~ 10.4 keV line in the reactor data is used. First, the working principle of the method will be described. Then, the used model functions are introduced and the estimation of each model parameter will be explained. In the end, the calculation of the efficiency curves and systematic uncertainties will be presented.

The calculated cut efficiency is defined as the percentage of neutrino events surviving the PSD-cut. Consequentially, the cut efficiency makes no statement about the number of slow or normal pulses cut. However, neutrino events are assumed to be all normal pulses and thus, mostly slow pulses are rejected by the PSD-cut, especially at higher energies. The definition of the efficiency was chosen because one parameter is estimated under the

assumption that the interactions are happening homogeneously throughout the Ge diode. That is true for neutrino events but not for all interactions creating normal pulses.

Method

In the following, an overview of the method to calculate the systematic uncertainties and cut efficiencies will be given.
First, the forced trigger pulser measurement is used to find a model function describing the τ-distribution for each measured energy point. The pulser measurement is used because it allows recording pulses at very low energies. Additionally, we have control over the input pulse and can record a separate τ-distribution for each physical population. Also, other experiments use pulser measurements to define a PSD-cut [1]. Only the two normal pulse distributions are considered because it is assumed that neutrino events only contribute to the normal pulse populations. Therefore, we need a model for the higher and one for the lower population for each energy point. These models describe the broadening of the τ-distribution due to the noise. Due to the discrepancy observed between the pulser and physical data arising from the electronic response of the DAQ and the preamplifier, the model parameters from the pulser measurement can not be used for further calculation. For example, the mean value obtained from the pulser measurement is too large (see section 4.4.2). As a consequence, the model parameters and errors are estimated from Th-228 and reactor-ON data. Also, reactor-OFF data could be used, but only reactor-ON data was available at the time of writing. The estimation of the model parameters from Th-228 data results in large uncertainties for the parameters. These large uncertainties will propagate into the systematic uncertainties of the cut efficiency. After the estimation of the parameters, the models are used to calculate the cut efficiency. For this, a scan over different efficiencies is performed and for each efficiency, the corresponding τ_{cut} value is calculated. The τ_{cut} value gives the point of the model τ-distribution at which it needs to be cut in order to achieve the intended efficiency. A systematic error for the efficiency is calculated by error propagation. In the end, we obtain for each energy point a list containing all scanned cut efficiency, including the systematic uncertainty and the corresponding τ_{cut} value.
To summarize the method: ***First***, the pulser measurement is used to find models for the τ-distributions. ***Second***, the models are anchored to physical data. ***Third***, the anchored models are used to calculate the cut efficiency.

Model

The model functions are determined by fitting different functions to the τ-distribution and taking the simplest best-fitting function. Moreover, the function should obey the following two requirements. First, the model function should have as few free parameters

as possible and the parameters should be related to "physical" quantities, for example, to the full width half maximum (FWHM) of the distribution. Otherwise, it would be difficult to estimate the parameters from the physical data. Second, the parameters should be independent of each other. For simplicity, the $\log_{10}(\tau)$ parameter will be substituted by x for this part of the thesis.
In total, three model functions are used for three different energy ranges. In the following, they are presented.
Gauss: In the energy range of $E \approx 7.5 - 32$ keV, a Gaussian function is used for the higher population and the model of the lower population is fixed.

$$f_{\text{higher}}(x) = \frac{1}{\sqrt{2\pi}\sigma} e^{-\frac{(x-\mu)^2}{2\sigma^2}}, \tag{4.3}$$

For these high energies, the higher and lower distribution can be distinguished well. Since the cut will be set somewhere in the higher population, the model function of the lower population does not matter. For simplicity, the model of the lower population will fixed. That should be justified because at higher energies, the pre-increase is not hidden by noise and thus, the rise time parameter from lower population events will be smaller than from higher population events. In contrast, for lower energies, the noise plays a more significant role, and thus the lower and higher distribution mix and can not be distinguished. Therefore, at lower energies, the lower population is modelled by a function again. In order to be more compatible with other functions, not the mean value μ and standard deviation σ are estimated from the physical data, but the mode M and the FWHM of the model. The relations between the parameters for the Gauss function are shown below [57]:

$$M = \mu, \tag{4.4}$$

$$FWHM = 2\sqrt{2\log(2)}\sigma. \tag{4.5}$$

The gauss model describes the τ-distributions quite good, at these energies. For example, the reduced χ^2 (χ^2_{red}) for the higher population model at $E \approx 9.8$ keV is $\chi^2_{\text{red}} = 1.07$. A summary plot with all distributions and the corresponding model included can be found in Fig. B.7 for the higher population and in Fig. B.8 for the lower population.
Loggauss: In the energy range of $E \approx 0.3 - 7.5$ keV, the distributions develop an asymmetry, such that the Gauss is not the best fitting model anymore. The used model for this energy range is the function shown below and will be called in the following 'loggauss':

$$f_i(x) = \frac{1}{\sqrt{2\pi}\sigma} e^{-\frac{\sigma^2}{2}} e^{-\frac{\log(x-\mu)^2}{2\sigma^2}}, \quad i \in \{\text{higher, lower}\}, \tag{4.6}$$

The relation between the value μ and σ and the mode M and FWHM are:

$$M = \mu + 1, \tag{4.7}$$

$$FWHM = 2\sinh\left(\sqrt{2\log(2)}\sigma\right). \tag{4.8}$$

The calculation of the FWHM can be found in the appendix C.2. In this energy range, the model is used for the higher and lower population. It is interesting to note that the Gauss model is a limit of the loggauss model in the case of a small σ. For small σ also the difference $x - \mu$ will be small, allowing to take the Taylor expansion of the logarithm and obtain the gauss model as the limit. The full calculation can be found in the appendix C.3. Since σ becomes smaller for higher energies, the gauss model is the limit of the loggauss model for the high energy case. Again, all distributions and the corresponding model functions can be found in Fig. B.7 and B.8. The best fit for the higher population is at an energy of $E \approx 1$ keV with $\chi^2_{\text{red}} = 1.06$ and the worst fit is at $E \approx 310$ eV with $\chi^2_{\text{red}} = 2.60$. For the lower population, the fits are slightly better, with, e.g. a $\chi^2_{\text{red}} = 2.05$ at an energy of $E \approx 310$ eV.

Loggauss gauss: In the last energy range, from $E \approx 0.2 - 0.3$ keV, a combination of a loggauss and a Gauss model can be used:

$$f_i(x) = \frac{1}{1+R_i}\left[\frac{R_i}{\sqrt{2\pi}\sigma_1}e^{-\frac{\sigma_1^2}{2}}e^{-\frac{-\log\left(x-((\mu-\Delta\mu)-1)\right)^2}{2\sigma_1^2}} + \frac{1}{\sqrt{2\pi}\sigma_2}e^{-\frac{(x-(\mu+\Delta\mu))^2}{2\sigma_2^2}}\right], \tag{4.9}$$

$$i \in \{\text{higher, lower}\},$$

with R_i being the relative amplitude between the loggauss and gauss part of the function. Some assumptions need to be made to estimate some parameters of the function, which cannot be estimated from physical data. The first assumption is that the peak described by the gauss function purely arises from noise effects. If this is true, the parameters σ_2 and R_i can be estimated directly from the pulser measurement because the noise effect should be the same for physical and pulser data. Another assumption is that the outwards drift of the two peaks, described by $\Delta\mu$, is purely noise driven. In this case, the parameter can be estimated from the pulser measurement, too. The last assumption is that the peak described by the loggauss function comes from the physical signal, allowing to estimate the parameters σ_1 and μ from the Th-228 measurement. Before using the model for efficiency calculations, more investigations are necessary to check if the assumptions hold true. Due to time constraints, the investigations were not carried out and in this thesis, we will restrict ourselves to the energy range of $E \approx 0.3 - 32$ keV. As before, the τ-distributions and corresponding model functions can be found in Fig. B.7 and B.8. The model fits quite well, with χ^2_{red} values between $\chi^2_{\text{red}} = 0.929 - 1.29$, for both populations.

Total model: The total model for each energy point used for the efficiency calculations

is the sum of the model for each population.

$$f_{\text{total}}(x) = A_{\text{higher}} f_{\text{higher}}(x) + A_{\text{lower}} f_{\text{lower}}(x). \tag{4.10}$$

with A_i, $i \in \{\text{higher, lower}\}$ being the relative amplitude of the higher or lower population. All model functions are normalized to unity. As a result, the integral of the total model is equal to $A_{\text{higher}} + A_{\text{lower}}$. Since the area of the total model should be unity, the sum over the relative amplitudes needs to be one ($A_{\text{higher}} + A_{\text{lower}} = 1$).

Parameter Estimation

In total, three parameters need to be estimated for each energy point: mode M, FWHM, relative amplitude A. The first two parameters are estimated from the Th-228 calibration measurements and the latter is estimated from the $\sim$ 10.4 keV line of the reactor-ON data. In the following, it will be discussed how the different parameters and the corresponding errors are estimated.

Relative amplitude A:

The parameter A is the relative amplitude of the higher or lower population. From the first simulations, we know that the events in the lower population come from interactions close to the p+ contact of the Ge diode (see section 2.4.1). Furthermore, the attenuation coefficient is a function of energy and thus, some background particles will have a different penetration depth depending on their energy. As a result, at low energies, more background events occur close to the p+ contact than at higher energies, leading to an energy dependence of the parameter A. In addition, the relative amplitudes can change if the μ-veto is applied (see section 4.6.1). Therefore, this parameter can not be estimated from a Th-228 measurement and will be calculated assuming that the incoming particle interacts homogeneously throughout the detector for all energies. The assumption of homogenous interactions is valid for neutrinos and the parameter A is energy independent. Accordingly, the cut efficiency needs to be defined as the number of neutrinos surviving the PSD-cut. The efficiency can not be defined as normal pulses surviving the cut because not all normal pulses are created homogeneously in the detector. For the estimation of the parameter, the $\sim$ 10.4 keV is chosen. The line comes from the decay of the Ge isotopes ^{68}Ge and ^{71}Ge. The latter isotope is continuously activated by muon induced neutrons created inside the lead shielding. In addition, the isotope was activated by a ^{252}Cf source since the line is used for the energy calibration of the experiment [19, 39]. It can be assumed that the interactions from the decay of the $\sim$ 10.4 keV happen homogeneously throughout the active volume of the detector [19]. Therefore, the line is suitable for the amplitude estimation.

The amplitude is estimated by calculating the percentage of events inside the higher or lower population relative to the complete normal population. In order to define the energy region in which the amplitude is calculated, the $\sim$ 10.4 keV line is fitted with a Gaussian

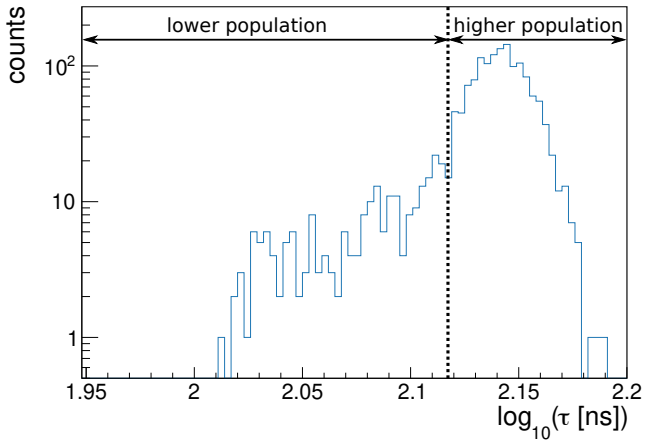

Figure 4.15.: τ-distribution used for the estimation of the parameter A. The used energy range is $E = 10.14 - 10.59$ keV and a total of $\sim$ 88 days of reactor-ON data is used. For this distribution, the C1 detector was used.

Table 4.3.: Estimate values for the relative amplitudes A for the C1 detector. In addition, the estimated background counts in the used energy region are shown. The used energy range is $E = 10.14 - 10.59$ keV and a total of $\sim$ 88 days of reactor-ON data is used.

population	background counts	counts (background reduced)	A
higher	131^{+4}_{-3}	1230^{+34}_{-46}	$0.918^{+0.025}_{-0.03}$
lower	134^{+3}_{-4}	110^{+46}_{-34}	$0.082^{+0.03}_{-0.025}$

function with mean μ and standard deviation σ and the energy region is defined as $\mu \pm 3\sigma$. For the calculation, reactor-ON data is used. A plot of the τ-distribution for this energy range is shown in Fig. 4.15. The boundary between higher and lower populations is chosen by eye and for the uncertainty estimation, this boundary is moved to higher and lower τ values. For the higher population, the interval of $\log_{10}(\tau) = 2.117 - 2.200$ $\log_{10}$(ns) and for the lower population, the interval $\log_{10}(\tau) = 2.000 - 2.117$ $\log_{10}$(ns) is chosen. Before calculating the number of events from the $\sim$ 10.4 keV line, the background events from other sources are estimated in this energy range. To calculate the background events, the number of events in the energy range before ($E = 9 - 10$ keV) and after ($E = 11 - 12$ keV) the line are estimated. The mean of these two values is used as the number of background events and is subtracted from the number of the $\sim$ 10.4 keV line events. All numbers for both populations and the final parameters A are shown in Tab. 4.3.

Furthermore, the amplitudes of the lower and higher population are fully correlated because the sum of both values is imposed to be one. Therefore, only the higher amplitude is used in the final calculation of the efficiencies, and the lower amplitude is substituted by $A_{\text{lower}} = 1 - A_{\text{higher}}$.

Under the assumption that the interaction happens homogeneously inside the detector, the amplitudes should reflect the relative volume of the Ge diode in which the type of

interaction occurs. In other words, A_{lower} should correspond to the relative volume for which the resulting pulses have no or a slight pre-increase. If we assume that the volume in which the lower interactions occurs is a half-sphere around the p+ contact, we can calculate the radius r_l of this volume V_l. With the total volume of the detector V_tot assumed to be a cylinder, we can find the following relation:

$$A_\text{lower} = \frac{V_\text{l}}{V_\text{tot}} = \frac{\frac{2}{3}\pi r_\text{l}^3}{\pi r_\text{tot}^2 h_\text{tot}} \rightarrow r_\text{l} = \sqrt[3]{\frac{3}{2} A_\text{lower} r_\text{tot}^2 h_\text{tot}} \tag{4.11}$$

Using the value for A_lower from Tab. 4.3 and for the other values $r_\text{tot} = 31$ mm and $h_\text{tot} = 62$ mm [19], a value of $r_\text{l} \approx 19.4$ mm is found for the radius. Another way to estimate this value would be to use a pulse shape simulation or Th-228 data at higher energies.

Mode M:

The mode parameter is the anchoring point of the model functions in τ space. In section 3.2.4, it was shown that the rise time parameter τ should be energy independent and thus, the mode parameter should be the same for all energies. Looking at the τ vs. energy plots, we can confirm that there is no strong energy dependency for the τ parameter. Therefore, the mode parameter only needs to be estimated for a high energy point and the other mode values are fixed to this value. In order to obtain the parameters for the two populations, the mode value is calculated from a Th-228 measurement in the energy range of $E = 29 - 31$ keV. For the higher population, a Gauss function is fitted to the peak in the τ-distribution and the mean value of the fit is used as the mode parameter (see eq. 4.4). With this method, a value of $\log_{10}(\tau) = 2.14235 \pm 0.00011$ $\log_{10}(\text{ns})$ is estimated. At high energies, the lower population does not have a Gaussian shape. Therefore, for the mode value, the mean value and for the mode error, the standard deviation of this population is used. For the lower population, a value of $\log_{10}(\tau) = 2.090 \pm 0.026$ $\log_{10}(\text{ns})$ is calculated.

Moreover, we can look at the mode values from the pulser measurement. A plot showing the mode value vs. the energy for both populations is shown in Fig. 4.16. In this figure, a deviation from the anchoring point can be seen for the values above $E \approx 2.5$ keV. To account for this, the relative deviation is used as symmetric uncertainty for these energy points. The highest energy point is the reference and thus, only the rescaled model fit error is used for the mode uncertainty. The deviation could be an effect coming from the pulser. If this is the case, the deviation should be ignored. Therefore, looking into the effect is necessary to reduce the uncertainty of the mode value and thus of the cut efficiency. Additionally, for the energy points below $E \approx 2.5$ keV, a systematic drift towards lower τ values can be observed for both populations until the model changed to the loggauss gauss model for $E < 300$ eV. Since the loggauss gauss model is not used, we will ignore these data points for now. An assumption is that the systematic drift is an effect coming from the noise. Consequently, the effect should be visible in the data as well and included in the model parameter. To do that, the size of the drift is scaled down to the anchoring

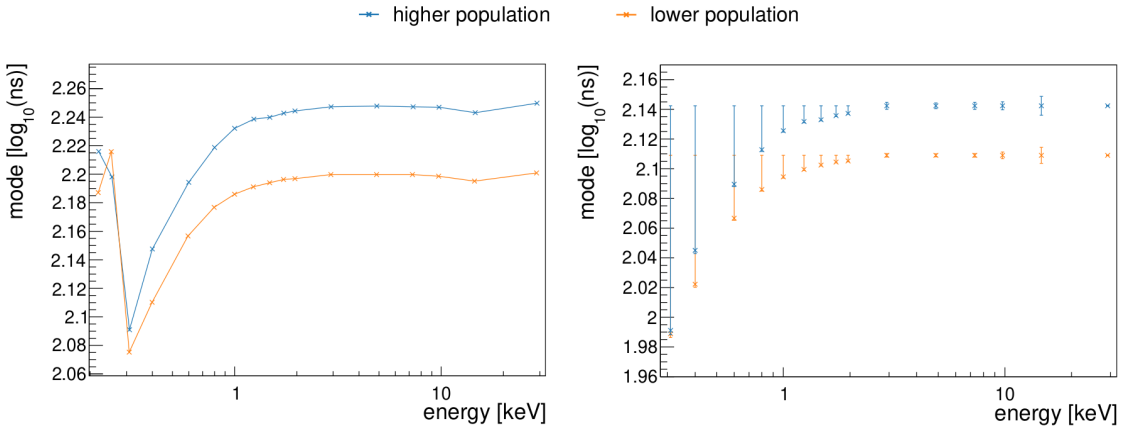

Figure 4.16.: The left figure shows the mode values from the pulser measurement for both populations. The right figure shows the mode parameters used for the models. The uncertainty due to the stability of τ is not included in the plot. For both plots, the C1 detector was used.

value of the Th-228 measurement and the mode values are redefined as the estimated values from above minus the relative drift. In order to still cover the range of the high energy value, i.e. allow an energy-independent τ, the size of the scaled drift is used as the positive mode uncertainty. For the negative uncertainty, the rescaled fit error from the pulser measurement is used. A summary plot showing the mode values, including the uncertainties for all measured energy points, can be found in Fig. 4.16.

In addition to the uncertainty discussed above, the stability of the τ parameter over time has to be taken into account. The stability was already discussed in section 4.1 and it was shown that the τ distribution for C1 is relatively stable over time. Nevertheless, a systematic uncertainty is taken as the standard deviation of the data points of Fig. 4.2. It is calculated to be $\sigma_{\log_{10}(\tau)} = 0.0003\ \log_{10}(\text{ns})$ and is added quadratically to the uncertainties described above. Figure 4.17 shows the relative contribution of the parameter uncertainty and the stability uncertainty to the total mode uncertainty. It can be seen that the stability uncertainty is for all data points subdominant, except for the highest data point. That makes sense because the parameter uncertainty for the highest data point is the rescaled model fit error which is very small.

Full width half maximum FWHM:

For the estimation of the FWHM parameter, two different methods are used. At high energies ($E \approx 7.5{-}32$ keV), the lower and higher population are distinguishable. Therefore, the FWHM can be estimated directly from the Th-228 measurement by fitting a gaussian function to the higher population. The fit parameter and error of the gaussian function are translated into an FWHM with equations 4.5 and C.35 and the FWHM is used as the model parameter. Since the lower population model is fixed at these energies, it is unnecessary to estimate the FWHM for this population. At energies below $E \approx 7.5$ keV, the estimation is more complicated because the lower and higher populations are not

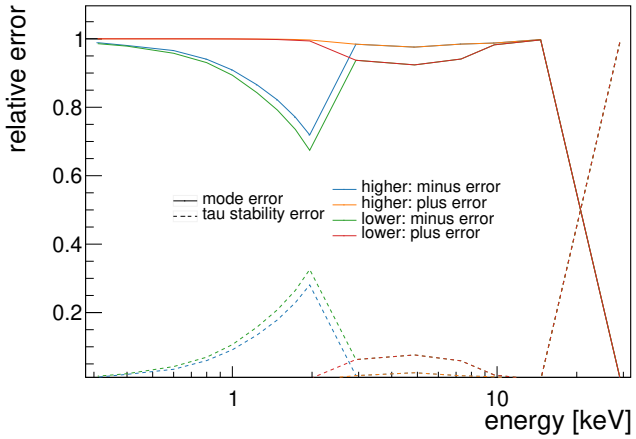

Figure 4.17.: Relative contribution of the parameter uncertainty (solid lines) and the stability uncertainty (dashed lines) to the total mode uncertainty.

distinguishable. The combination of both populations is fitted by a gaussian function to estimate the FWHM of the combined peak. However, this is not possible for all energies because, at energies below $E \approx 600$ eV, the mixing of the normal and slow pulse population is too strong. For the energies below 600 eV, the values are extrapolated by fitting the following function to the data points:

$$f(E) = p_0(E+1)^{p_1} + p2, \tag{4.12}$$

with the resulting best fit parameters: $p_0 = 1.4 \pm 0.3$, $p_1 = -2.68 \pm 0.29$ and $p_2 = 0.065 \pm 0.005$. The parameters are strongly correlated (correlation coefficients: 0.6-0.96) and thus, the correlation coefficients are taken into account for the calculation of the error bands of the function. With the fit parameters and the correlation coefficients, the 3σ error band of the fit function can be calculated via the error propagation formula for correlated errors. The calculation can be found in the appendix C.4. The 3σ error band is chosen conservatively instead of the 1σ band such that all estimated values from the Th-228 measurement lie inside the error band. For each lower and higher population model below an energy of $E \approx 7.5$ keV, the values obtained from the fit function and the 3σ error band are used as values for the FWHM and the parameter uncertainty. A summary plot showing the estimated FWHM values for all measured energies as well as the fit function can be found in Fig. 4.18.

A problem of the described method above is that the FWHM for one population is estimated by fitting both populations at the same time. Therefore, a consistency check needs to be performed. For the consistency check, it is tested if the FWHM of the total model (the sum of the model for the lower and higher population) is compatible with the estimated value of the combined peak from the Th-228 measurements. The inspection showed that the FWHM of the total model is systematically larger than the one estimated from the physical data. However, for all models, the deviation is within the 1σ band of

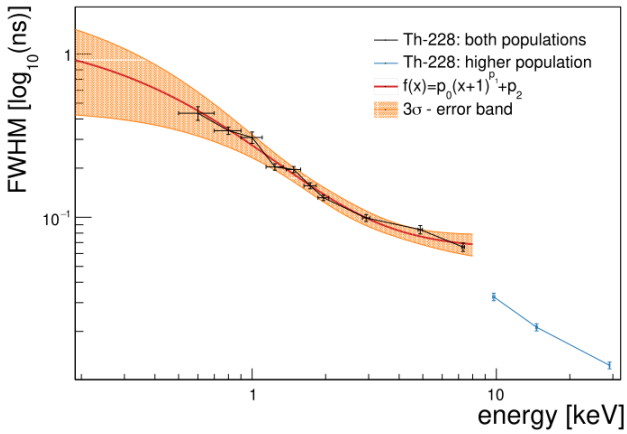

Figure 4.18.: Summary of all FWHM parameters used for the lower and higher population models. At high energy, the values and errors of the fit to the higher population are used. For lower energies, the values from the fit function and the 3σ error band are used.

the fit. As a result, the FWHM of the total model is compatible with the estimated values and thus, this discrepancy will be neglected. A possible explanation for the FWHM of the total model being compatible with the estimated values is that the variance of the two models is larger than the difference of their mean values. Moreover, the major contribution to the total model only comes from one population (see Tab. 4.3).

Calculation of the Efficiency and Systematic Uncertainties

After the models are defined and the model parameters, including uncertainties, are estimated, the cut efficiency can be calculated. First, the $\log_{10}(\tau_{\text{cut}})$ values will be determined, at which the τ spectrum needs to be cut, in order to reach a given cut efficiency. The total models are all normalized to one, such that the integral over the total model until a $\log_{10}(\tau_{\text{cut}})$ value will give the percentage of events surviving the PSD-cut and, thus, the cut efficiency ϵ_{cut}.

$$\int_{\log_{10}(\tau_{\text{min}})}^{\log_{10}(\tau_{\text{cut}})} f_{\text{total}}(\log_{10}(\tau))\ \mathrm{d}\log_{10}(\tau) = \epsilon_{\text{cut}} \tag{4.13}$$

The lower boundary of the integral is chosen depending on the model. For a gauss model, unity is arbitrarily chosen because all models are basically zero reaching this value. In the case of the loggauss model, $\log_{10}(\tau_{\text{min}}) = M - 1$ is chosen since the model function is only defined for higher values. Also, the loggauss model is basically zero for this value. For a given cut efficiency, the corresponding $\log_{10}(\tau_{\text{cut}})$ value is found by an iterative process. In each step, the $\log_{10}(\tau_{\text{cut}})$ value is increased by 10^{-5} $\log_{10}(\text{ns})$ and equation 4.13 is solved numerically with ROOT [21] until the desired cut efficiency is reached. Afterwards, the $\log_{10}(\tau_{\text{cut}})$ value is fixed and the systematic uncertainties of the cut efficiency are calculated

Table 4.4.: Example cut efficiencies ϵ_{cut} for the model at an energy of $E = 1$ keV. The calculation is performed for the C1 detector.

$\log_{10}(\tau_{\text{cut}})$ [$\log_{10}$(ns)]	cut efficiency ϵ_{cut} [%]	-Δ ϵ_{cut} [%]	+Δ ϵ_{cut} [%]
2.13683	50.0	1.3	5.4
2.15186	55.0	2.1	5.5
2.16735	60.0	2.7	5.6
2.18361	65.0	3.3	5.7
2.20101	70.0	3.9	5.8
2.22011	75.0	4.3	5.8
2.24177	80.0	4.5	5.6
2.26756	85.0	4.4	5.2
2.30084	90.0	4.0	4.5
2.35195	95.0	2.9	3.1
2.45385	99.0	1.0	1.0

by standard error propagation. The error propagation formulas and their derivation can be found in appendix C.5. If the uncertainties are too large, it can happen that the uncertainty added to the efficiency is artificially larger than one. In this case, the uncertainty is reduced to a value such that the sum is equal to unity. For each input efficiency, the output is a $\log_{10}(\tau_{\text{cut}})$ value and systematic uncertainties for the efficiency. An example output for the model at an energy of $E = 1$ keV is shown in Tab. 4.4. In this example, a scan over possible cut efficiencies between 50% and 99% was performed. The table shows, e.g. if a cut is applied at a value of $\log_{10}(\tau_{\text{cut}}) = 2.35195$ $\log_{10}$(ns), a resulting cut efficiency of $95.0^{+2.9}_{-3.1}$% is reached. In Fig. 4.19a, the calculated cut values and efficiencies from Tab. 4.4 are plotted as an efficiency curve. The efficiency curves for all measured energy points can be found in Fig. B.9.

Furthermore, the relative contribution of each model parameter to the total systematic uncertainty can be plotted. An example is shown in Fig. 4.19b for the model at an energy of $E = 1$ keV. This kind of plot can be used to visualize the dominant contribution to the systematic uncertainty. In Fig. B.10, the relative uncertainty contribution plots for all measured energy points can be found. Figure B.10 shows that the systematic uncertainty is dominated in the region of interest for high cut efficiency values by the contribution of the FWHM. For low cut efficiency values, the contribution of the mode parameter dominates the positive systematic uncertainty.

Another systematic uncertainty that can contribute to the overall uncertainty is related to the model choice. For example, at the energy $E = 9.8$ keV, the gaussian function is chosen as the model, but a loggaus function could also describe the distribution. Another example is the distribution at an energy of $E = 0.31$ keV. A loggauss function was used for the model instead of the loggauss gauss function. How the systematic uncertainty is included for these models will be explained for the model at $E = 0.31$ keV.

First step: The cut efficiency for the nominal model is calculated. In Fig. 4.20a, the cut efficiency for the loggauss model is shown in blue. ***Second step:*** The cut efficiency for

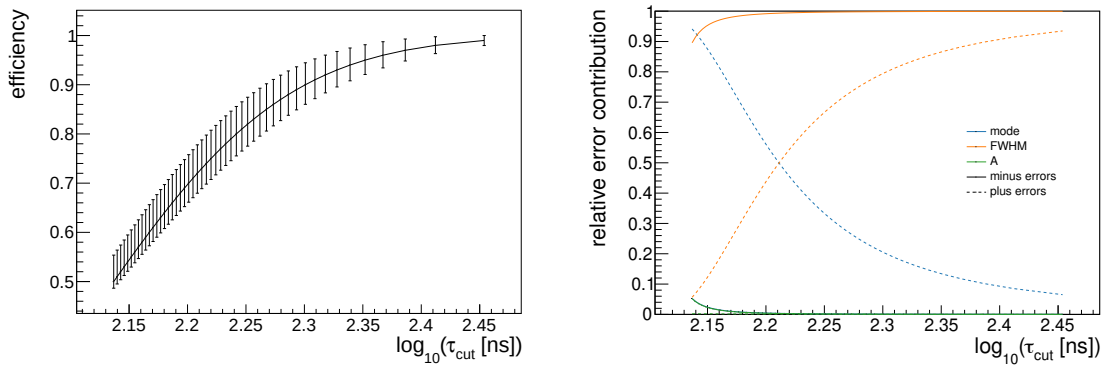

(a) **(b)**

Figure 4.19.: Figure a) shows a cut efficiency curve for the C1 detector at an energy of $E = 1$ keV. Figure b) shows the contribution of the different parameter uncertainties to the overall uncertainty for the model at this energy.

the alternative model function will be calculated (shown in Fig. 4.20a in orange). ***Third step:*** The difference between the two efficiency curves is taken as uncertainty and is added quadratically to the overall uncertainty.
In Fig. 4.20a, the efficiency curve with the updated uncertainties is shown in green. Additionally, the model uncertainty is included in the relative uncertainty contribution plot, shown in Fig. 4.20b. The uncertainty contribution plots in Fig. B.10 show that the model uncertainty is subdominant for all models where this uncertainty contributes.
In conclusion, the method described above allows to calculate for each cut efficiency, a $\log_{10}(\tau_{\text{cut}})$ value and the corresponding systematic uncertainties of the efficiency. The systematic uncertainties contributing to the overall uncertainty are listed below:

1. Systematic uncertainty from the model parameter
2. Stability of the τ parameter over time
3. Correct choice of the model function

The dominant contribution of the total systematic uncertainty comes from the model parameter and thus, from the anchoring to physical data. Therefore, it is of interest to find a description of the electronic response, to correct the pulses and be able to estimate the model parameters directly from the pulser measurement. That will lead to smaller model errors and thus will decrease the systematic uncertainty of the cut efficiencies.

4.5.2. Method to Find the Best Cut Efficiency

In order to apply the PSD-cut to physics reactor data, a cut efficiency needs to be chosen at each measured energy. The cut efficiency should be chosen in a way that the benefit of the cut is maximal. To describe the benefit, a figure of merit should be defined. A scan

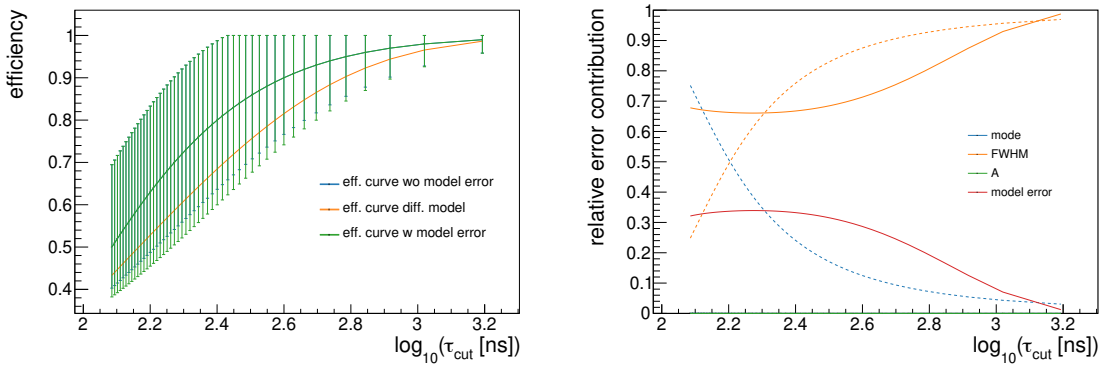

(a) **(b)**

Figure 4.20.: Figure a) shows a cut efficiency curve for the C1 detector at an energy of $E = 0.31$ keV. The blue curve shows the efficiency without the model uncertainty included, while the green curve shows the efficiency with the model uncertainty included. The orange curve describes the efficiency calculated with an alternative model to estimate the model uncertainty. Figure b) shows the contribution of the different parameter uncertainties and the model uncertainty to the overall systematic uncertainty. The dashed lines show the positive and solid line the negative uncertainties.

over different cut efficiencies can be performed to maximize this figure of merit. This can be repeated for each measured energy point to obtain an efficiency curve as a function of the energy. A factor describing the comparison of the signal and background after the cut should be included in the figure of merit, because the cut should ideally reduce the background as much as possible while leaving the signal untouched. For the calculation of the background after the cut, the PSD-cut can be applied to reactor-OFF data. Since the efficiency is defined as the number of neutrino events surviving the PSD-cut, the signal after the cut can be calculated by multiplying the cut efficiency to the signal prediction. Moreover, the figure of merit should include a factor reflecting the systematic uncertainty of the cut efficiency. More investigations are needed to find the ideal figure of merit for each specific physics case. This will be done in the future analysis of the CONUS experiment.

4.6. Application of the Rise Time Fit to Reactor-ON Data

In this chapter, the rise time fit will be applied to reactor-ON data. First, the τ-distributions for ~ 88 days of reactor-ON data will be shown and discussed (section 4.6.1). Afterwards, an example PSD-cut will be applied to the reactor-ON data and the resulting background reduction will be quantified (section 4.6.2). As before, the C1 detector will be used in this section as a benchmark detector.

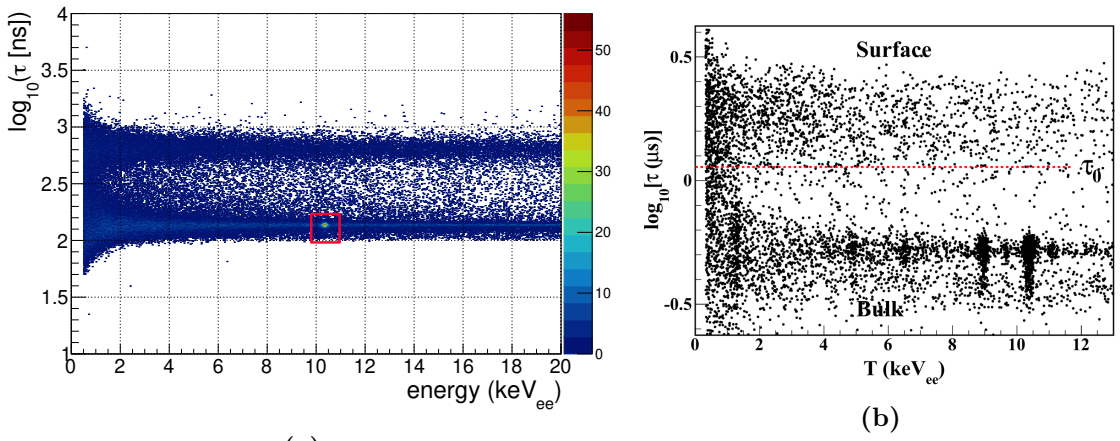

(a) (b)

Figure 4.21.: Figure a) shows a τ vs. energy plot for the C1 detector for a total of 88.5 days of reactor-ON data before the application of the μ-veto. The $\sim$ 10.4 keV line is marked with the red rectangle. The colour bar indicates the number of events per bin. Figure b) shows a τ vs. energy plot from the TEXONO collaboration. The plot is taken from [50]

4.6.1. Reactor-ON Spectrum

In Fig. 4.21a, a τ vs. energy plot for a total of 88.5 days of reactor-ON data before the application of the μ-veto is shown. As before, two major populations, one for slow and one for normal pulses, are visible and therefore, a PSD-cut will be possible. The $\sim$ 10.4 keV line is visible as a 'blob' in the normal pulses population, as expected since the decay of the Ge isotope happens homogeneously inside the detector [19] and the majority of the events occur inside the bulk volume, producing normal pulses. Therefore, the presence of the $\sim$ 10.4 keV line in the normal pulse population validates the rise time fit.
An interesting effect can be seen when comparing the $\log_{10}\tau$-distribution before and after the μ-veto (see Fig. 4.22). It can be observed that the ratio of events in the higher population relative to the lower population changes. Before applying the μ-veto, 64% of all normal pulse events are part of the higher population. After the application of the μ-veto, only 43% are part of the higher population. This has to be connected to the background cut away by the μ-veto. If the timespan between the muons triggering the μ-veto and the μ induced neutrons interacting with the Ge diode lies within the time window of the μ-veto, the events created by the μ induced neutrons are cut. These neutrons can be assumed to interact homogeneously throughout the detector. As a result, more events will be cut by the μ-veto in the higher than in the lower population because the higher population is related to the larger part of the active volume. The effect could lead to or contribute to the observed difference before and after the veto. Further investigations can help to understand this difference in more detail. It is interesting to look into the effect because it changes the shape of the normal pulse distribution.
Also, other experiments working with Ge detectors use PSD to discard events in the

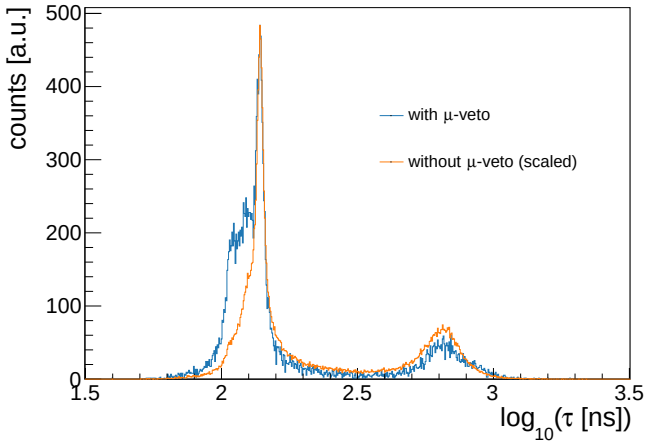

Figure 4.22.: $\log_{10}(\tau)$-distribution before and after the application of the μ-veto integrated over the energy range [0.5 keV, 20keV]. The distributions are created from 88.5 days reactor-ON data recorded with the C1 detector, and arbitrarily renormalized for visibility.

transition layer [1, 50]. As an example, in Fig., 4.21b a τ vs. energy plot from the TEXONO Collaboration is shown. For the shown plot, a Ge detector with a p+ point contact was used, similar to the CONUS detectors. When comparing the result from TEXONO and CONUS, it can be seen that with the CONUS detectors and the new DAQ system, a similar discrimination between normal and slow pulses is reached.

4.6.2. Example PSD-Cut

In this section, an estimation of the background reduction thanks to a PSD-cut is shown and quantified. At the time of writing, no reactor-OFF data with pulse shape information is available. Therefore, the background reduction will be estimated by applying the PSD-cut to reactor-ON data. That is justified because the signal over background ratio S/B is tiny for the used energy ranges. The ratio is $S/B \approx 10^{-2}$ at an energy of $E = 0.31$ keV and $S/B \approx 10^{-5}$ at an energy of $E = 0.39$ keV. For higher energies, the ratio becomes even smaller and thus, the signal contribution is negligible. The estimated number of the S/B for C1 RUN-5 under the assumption of a quenching parameter of $k = 0.16$ are kindly provided by A. Bonhomme. Moreover, due to time constraints, it was not possible to obtain the most beneficial cut efficiency using a figure of merit. As a result, an example cut function was estimated by eye. The used efficiency values at each energy are shown in Tab. 4.5 and the resulting efficiency curve can be seen in Fig. 4.23a. In Fig. 4.23b, the reactor-ON data is shown with the PSD-cut function included. The cut was chosen to keep a 99% cut efficiency until an energy of 1.5 keV. The small kink in the corresponding $\log_{10}(\tau_{\text{cut}})$ values at around $E \approx 7 - 10$ keV could be a consequence of the method used to determine the FWHM of the model function (see section 4.5.1 and Fig. 4.18).
An interpolation is used between the different pulser points to create a continuous function.

Table 4.5.: Cut efficiencies for the example PSD-cut. For each energy point, the efficiency and the corresponding $\log_{10}(\tau_{\text{cut}})$ value is listed.

energy [keV]	$\log_{10}(\tau_{\text{cut}})$ [$\log_{10}$(ns)]	cut efficiency ϵ_{cut} [%]	-$\Delta\epsilon_{\text{cut}}$ [%]	+$\Delta\epsilon_{\text{cut}}$ [%]
29	2.15442	99.0	0.3	0.3
14.6	2.16301	99.0	1.9	1.0
9.8	2.17406	99.0	0.6	0.6
7.3	2.21309	99.0	0.9	0.9
4.9	2.22074	99.0	0.7	0.7
2.9	2.24595	99.0	0.7	0.7
2.0	2.28597	99.0	0.7	0.7
1.7	2.30617	99.0	0.6	0.7
1.5	2.33761	99.0	0.6	0.7
1.2	2.35290	98.0	1.2	1.3
1.0	2.38632	97.0	2.2	2.3
0.8	2.43051	96.0	4.0	4.0
0.6	2.45927	93.0	7.0	7.0
0.4	2.48728	88	12	12
0.3	2.48549	85	19	15

In order to avoid large interpolation errors, more energy points could be measured. Appling the PSD-cut, all events above the cut function are discarded and to quantify the possible background reduction, the percentage of rejected events is calculated. The percentage is calculated by taking the ratio of events before and after the cut and subtracting it from unity. The energy spectrum before and after the PSD-cut can be found in Fig. 4.24 and the possible background reduction is listed in Tab. 4.6 for different energy ranges. All results of the PSD-cut shown here also include the reduction due to the quality cut explained in section 3.2.4.

In Tab. 4.6, it can be seen that the achieved reduction is larger at higher energies. That is in contrast to what we would expect. The penetration depth of the particles becomes smaller for lower energies and thus, more particles will interact in the transition layer. As a result, we would expect a stronger reduction at lower energies. A possible explanation for the larger reduction at higher energies could be related to the change of the calculation method for the FWHM. For higher energies, it looks like the cut function is closer to the higher population than for lower energies, resulting in a stronger cut and larger reduction. All in all, in this section, a pulse shape discrimination down to energies of $E \approx 300$ eV is shown. Until energies of 1.5 keV, a cut efficiency of 99% can be used and below this energy, the minimal cut efficiency is 85^{+15}_{-19}%. The maximal reduction of 35.9% is reached in the energy range of $E = 10.6 - 20$ keV and in the region of interest ($E = 0.3 - 2$ keV), the achieved reduction is 23.3%.

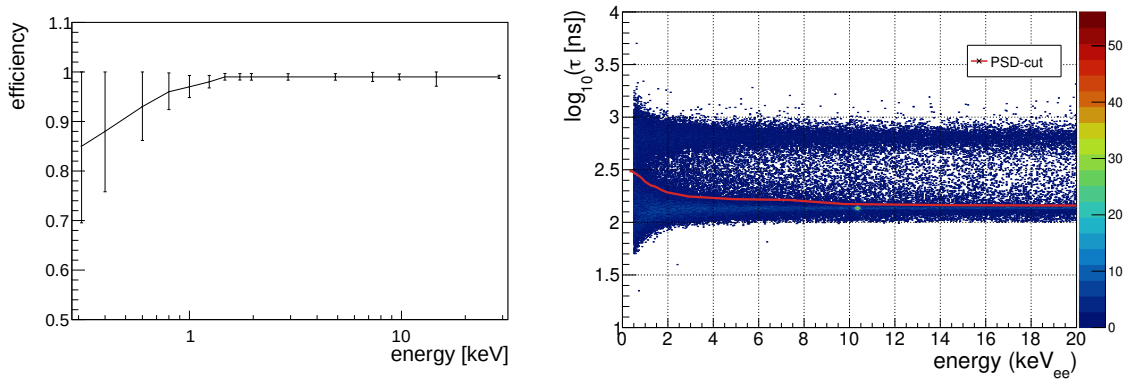

(a) (b)

Figure 4.23.: Figure a) shows the chosen cut efficiency as a function of energy, for the example PSD-cut. In figure b), a τ vs. energy plot for a total of $\sim$ 88 days of reactor-ON data for the C1 detector before the application of the μ-veto is shown. The red function shows the example PSD-cut and the colour bar indicates the number of events per bin.

Table 4.6.: Background reduction achieved with the chosen PSD-cut for different energy ranges. The reduction is calculated for reactor-ON data measured with C1, assuming that the signal contribution is negligible for the $\sim$ 88 days of measurement time. The used cut function is only exemplary. The reduction is defined as the percentage of rejected events. For the results shown in this table, the reduction due to the quality cut (see section 3.2.4) is also included.

energy [keV]	reduction $\left(1 - \frac{\text{cts with PSD}}{\text{cts without PSD}}\right)$
$0.3 - 2$	0.233
$2 - 10.1$	0.218
$10.1 - 10.6$	0.041
$10.6 - 20$	0.359
$20 - 32$	0.275

4.7. Discrimination of SSE and MSE

In this section, a by-product of the rise time fit, the discrimination of SSE and MSE is demonstrated. Multi-site events play a significant role at higher energies, i.e. at MeV scale, when γ-rays can interact via Compton scattering and pair production. As a result, energy ranges up to several hundred keV are investigated in this section.
If the rise time fit is applied to a MSE, the function describing a single pulse is fitted to the sum of multiple pulses recorded by the DAQ. In order to describe the recorded pulse as best as possible, a function with a larger rise time, compared to the rise time of each single sub pulse, is fitted to the MSE. An example of a fitted MSE is shown in Fig. 4.25a. Therefore, all MSE will have a larger τ value than the SSE, allowing for SSE and MSE discrimination. A τ vs. energy plot for a Th-228 measurement recorded with C1 up

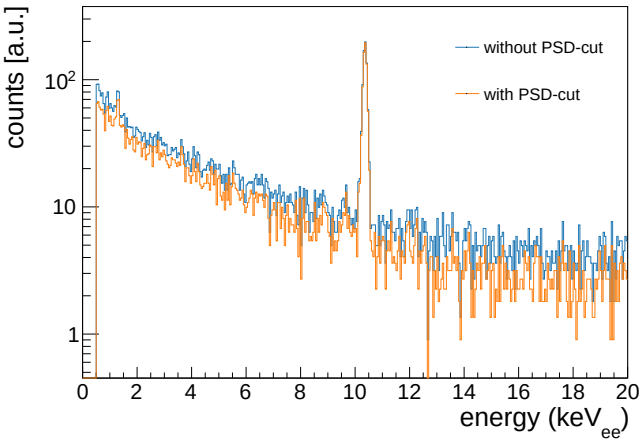

Figure 4.24.: Energy spectrum for 88.5 days of reactor-ON data before and after the PSD cut.

to energies of 900 keV is shown in Fig. 4.25b. In this figure, a normal pulse population containing SSE can be seen around a value of $\log_{10}(\tau) \approx 2\ \log_{10}(\text{ns})$. The MSE lie in the region above the SSE band. For energies below 100 keV, a contribution to the region above the SSE band from slow pulses can be seen as well. Slow pulses do not contribute significantly at higher energies because the γ-rays can penetrate the detector far enough to reach the active volume and produce normal pulses. Most interesting are the vertical lines visible in Fig. 4.25b. Events inside the lines with a τ parameter above the SSE band are mainly MSE. These lines appear at the energies of the Th-228 spectral lines because more γ-rays are produced with this energy than for the Compton continuum. The events contained in the vertical lines with a τ value inside or below the SSE band are SSE. Events inside the SSE band have a pre-increase and the events below have only a slight or no pre-increase. Besides a visual inspection of the data, more tests can be performed to confirm the findings described above. In the following, some tests will be discussed.

First test: The photoelectric absorption is dominant for energies below $E \lesssim 100$ keV and mainly SSE are produced in the interaction. In contrast, through Compton scattering SSE and MSE events can be produced and the interaction becomes dominant for energies larger than $E \approx 100$ keV (see section 2.4.3). If the vertical lines come from MSE, it is expected that peaks above 100 keV show the MSE lines, while peaks below 100 keV do not show them. A Ba-133 measurement can be used to check this hypothesis. Ba-133 has a peak at $E = 80.9979 \pm 0.0011$ keV and four peaks at energies of $E > 250$ keV [11]. In Fig. 4.26, a τ vs. energy plot for Ba-133 conducted with the C5 detector in the LLL is shown. It is visible that the peak at $E \approx 80$ keV does not show a vertical line and the four peaks above 250 keV show them. Exactly that is what we would expect and thus, supports the hypothesis that the vertical lines consist of MSE.

Second test: Events contributing to the double escape peak (DEP) of pair production are with a high probability SSE (see section 2.4.3). Therefore, the DEP should not show a MSE line in a τ vs. energy plot, although the peaks around the DEP show such a line.

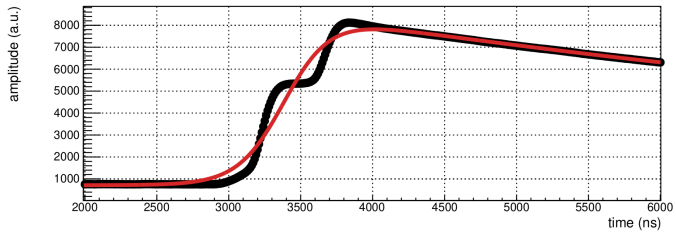

(a)

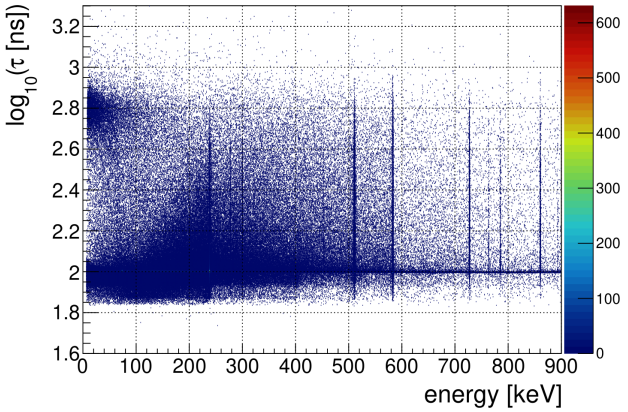

(b)

Figure 4.25.: In figure a), an example for a MSE, including the rise time fit function is shown. In figure b), a $\log_{10}(\tau)$ vs. energy plot for a high energy Th-228 measurement conducted with C1 is shown. The colour bar indicates the number of events per bin.

As a radioactive source, Th-228 can be used to probe the DEP. Thorium-228 has a strong line at an energy of $E = 2614.511 \pm 0.010$ keV [10], resulting in a DEP at an energy of $E = 1592.511$ keV. Figure 4.27 shows a τ vs. energy plot for a Th-228 measurement conducted with C5, zoomed into the energy region around the DEP. In this figure, the DEP (marked with a red circle) can be seen and no vertical line is visible for the peak. In contrast, the two Th-228 lines around the DEP show the MSE lines. Again, exactly that is what we would expect for the vertical lines consisting of MSE.
Moreover, a horizontal line can be seen below the SSE band, in Fig. 4.27. These events arise from artefacts coming from an external attenuator. The attenuator was used for the measurement in order to reach high enough energies to observe the DEP. The conclusion should not be affected by these artefacts.

The two tests described above and the visual inspection confirm the origin of the vertical lines visible in the τ vs. energy plots. In conclusion, it was shown that MSE have a larger rise time parameter τ, giving the possibility to use the rise time information for MSE and SSE discrimination. The discrimination is interesting for the CONUS experiment to help better understand the high energy background. Furthermore, it can help to learn more about the low energy background because background sources visible in the high energy part can also contribute to the low energy background.

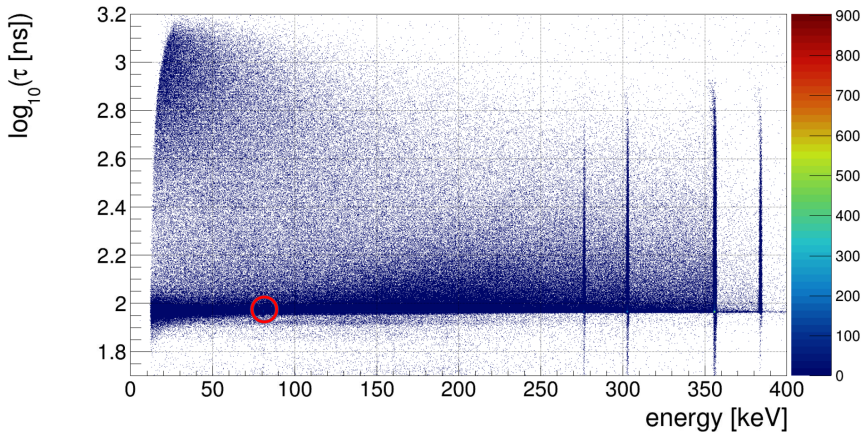

Figure 4.26.: τ vs. energy plot of a high energy Ba-133 measurement recorded with C5. The $E = 80.9979 \pm 0.0011$ keV [11] peak is marked with a red circle. The colour bar indicates the number of events per bin.

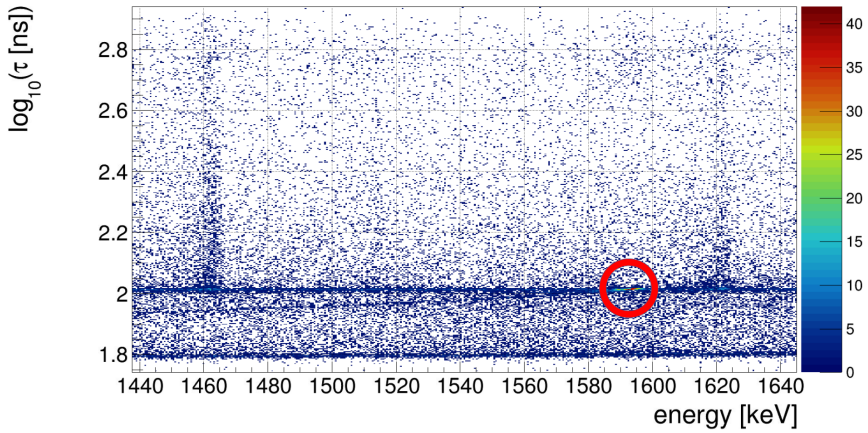

Figure 4.27.: τ vs. energy plot for a high energy Th-228 measurement. Only the region around the DEP (marked with a red circle) of the $E = 2614.511 \pm 0.010$ keV [10] line is shown. The colour bar indicates the number of events per bin.

Other experiments profit from using the MSE and SSE discrimination for background reduction. An example is the GERDA experiment, aiming to observe neutrinoless double beta decay ($0\nu\beta\beta$). The GERDA Collaboration developed and refined the A/E method [22, 23] introduced in section 3.1.1 as a method for MSE and slow pulse discrimination in a similar point-contact detector design as used in CONUS. With the A/E method, the GERDA experiment reaches an average MSE reduction of $86.2 \pm 0.2\%$ for an average SSE survival probability of $90.0 \pm 0.2\%$ [2]. The MSE reduction is calculated for the 1620 keV Th-228 FEP and the SSE survival probability is estimated from the 1593 keV Th-228 DEP. In the following, the MSE reduction achieved by GERDA with the A/E method is compared to the possible reduction with the here presented rise time fit. For the detectors C1-C4, no pulse shape data is available at these high energies. Therefore, the peak at

$E = 860.56 \pm 0.03$ keV [36] in the Th-228 spectrum of C1 is used to compare the MSE reduction from the rise time fit to the one achieved with the A/E method. For both peaks, the Compton scattering is the dominant interaction [14], making it as compatible as possible. The used energy range around the 860 keV peak is estimated from the 99.7% interval of a Gaussian distribution fitted to the peak. Since no method to calculate a MSE cut and the corresponding efficiencies is developed yet, a cut with 90% SSE survival probability is only roughly estimated. At an energy before the peak, where no MSE band is visible, the MSE cut is determined by estimating the $\log_{10}(\tau)$ value at which the SSE distribution needs to be cut to get 90% of the events from the distribution. With this rough estimate, a value of $\log_{10}(\tau) = 2.003$ is determined. All events in the 860 keV peak with a larger rise time parameter than the cut value will be rejected. As a result, we get a 84.7% MSE reduction for the C1 detector. The number is relatively close to the average value from the GERDA Collaboration. This is only a rough comparison and to do it more precisely, a proper MSE cut, including calculated efficiencies is necessary. However, the rough comparison already shows that a similar SSE and MSE discrimination is possible with the rise time fit compared to the A/E method. That demonstrates the universality of the rise time method. The technique can be employed, from sub-keV to several MeV, to efficiently separate SSE created in the active volume of the Ge diode (normal pulse) from SSE created in the transition layer (slow pulses) and from MSE events. Slow pulses contribute dominantly in the sub-keV and keV energy regime, wile MSE mainly contribute for energies above 100 keV.

Chapter 5.

Conclusions and Outlook

Up to now, no detection of the CEνNS interaction with the CONUS experiment was possible. Therefore, improvements regarding the three experimental challenges are necessary. The challenges are: **(1)** a high neutrino flux, **(2)** a very low energy threshold, **(3)** a low and stable background level.
With the new DAQ system installed at the experimental site for RUN-5 (begin: May 2021), first it has become possible to lower the energy threshold of the experiment. That is very beneficial and illustrated as follows: If the threshold would be lowered from the previously achieved around 310 eV to 210 eV, an increase from approx. 1 to 10 neutrino interactions per day is expected [1]. Second, with the new DAQ system the recording of pulse shapes has become possible. The goal of this thesis was to develop a analysis to further reduce the background of the experiment by examining these pulse shapes of single events on an event-by-events basis. In this thesis, it was possible to show that a background reduction through pulse shape discrimination (PSD) is possible for the CONUS experiment via the discrimination of so-called 'slow pulses' down to the sub-keV energy regime. The slow pulses are produced by interactions in the outer layer of the HPGe diode (transition layer) with a charge collection efficiency below 100%. For the purpose of PSD, a new method was developed, allowing also to calculate efficiencies and systematic uncertainties of a PSD-cut. In the following, the impact of the PSD analysis will be discussed. Afterwards, the main contributions of this thesis will be summarised and an outlook into future work will be given. In the end, the main results are summarised and presented.

Impact of the PSD analysis
A pulse shape analysis gives the possibility for a further background reduction and, therefore, can increase the experiment's sensitivity for CEνNS or BSM signals. For the CEνNS analysis, the energy region around and below 300 eV is most important. That is illustrated by the expected increase of CEνNS events due to lowering the threshold as described above. Therefore, lowering the threshold would be most beneficial for the CEνNS analysis. However, reducing the background will have a positive benefit, too. For the BSM analysis, we have to distinguish between two detection channels. First, BSM models can change either the shape or the expected count rate of the CEνNS signal. For these models, the same applies as mentioned above for the CEνNS analysis. An example of such a BSM model are non-standard neutrino interactions (NSI) in the neutrino-quark sector. Secondly, BSM models can be investigated via the neutrino-electron scattering channel, like, for example, the neutrino magnetic moment. For the electron recoil, measured in

[1] The numbers of expected neutrinos are kindly provided by A. Bonhomme.

neutrino-electron scattering, the quenching effect plays no role. The region of interest for the electron scattering is between $E \approx 2 - 8$ keV and can profit from the 99% PSD-cut efficiency and the resulting good background reduction in this energy range.
If the detectors are not cooled during storage, the transition and dead layer can grow over time (i.e. 0.1 mm/y ([2] and references therein)) and with it the number of slow pulses. Therefore, a good understanding of the pulses created in the transition layer and an effective PSD-cut to suppress these events can get even more important over time.
Moreover, an enhancement of the sensitivity can be achieved by improving the background model, because the background model is an input of the likelihood analyses. The pulse shape analysis can help to strengthen the predicted decomposition of the background model and, therefore, can help to reduce the systematic uncertainties of the MC background model itself. An example of this are cosmogenic lines. Events occurring in the transition layer, will have lower reconstructed energies and thus will contribute to the continuum below the lines. If the slow pulses are cut, the line should not be affected and the continuum should change, allowing to analyse if the contribution of the cosmogenic lines is implemented correctly. Furthermore, cutting the slow pulses will reduce the uncertainty related to the implementation of the transition layer and its charge collection efficiency and, therefore, will improve the MC background model [39].
Even though CEνNS events will only produce SSE, a background reduction due to SSE and MSE discrimination is not interesting for the CONUS experiment, because MSE plays no significant role in the region of interest. However, background sources identifiable at high energies can contribute to the low energy part of the spectrum. A pulse shape analysis can help to understand the experiment's high energy background by looking at the SSE and MSE. Vice versa, this will improve our understanding of the background at low energies.
Pulse shape analyses are interesting for other experiments or are already used by them, for example, to discriminate MSE or slow pulse events from normal pulse SSE. This makes the method presented in this thesis interesting for other experiments working with Ge detectors. However, it is important to mention that the here presented technique cannot be applied to other experiments one to one. The pulse shape depends on the geometry and electric field configuration of the Ge detector, meaning that the methods described might only work for the point-contact design.

Main contributions of this thesis & open points

The main goal of this thesis was the development of a PSD analysis applicable to the sub-keV energy regime, important for the CONUS physics analyses. It was shown that a discrimination of normal and slow pulses is possible with the here introduced rise time fit. Furthermore, a method was developed, to calculate the efficiency of a PSD-cut, including the determination of the systematic uncertainties. As far as we know, it is the first time a pulse shape discrimination was performed using the CAEN DAQ and the CoMPASS software with Ge ionisation detectors. In the following, the main contributions of this

thesis are listed and the necessary future work is discussed.

(i) Test of different PSD methods: In the beginning of this thesis, three different techniques to differentiate between normal and slow pulses are presented. The first method, the traditionally used A/E method, developed by the GERDA Collaboration has been used and tested at the MeV scale to discriminate MSE and slow pulses from SSE. However, the method uses the derivative of the pulse shape. At sub-keV energies, the derivative disappears completely in the noise, making it impossible to use this method for sub-keV energies. As a result, the A/E method does not fulfil the requirements for the CEνNS analysis. The second newly developed method uses the ratio of two integrals calculated over different regions of the pulses as a discriminating variable. Again, especially in the sub-keV region, the discriminating power of this method is not very strong. Finally, a third method, the rise time method was employed in this thesis. In this method, each raw event is fitted by a function describing the original form of the pulses. This method works indeed also in the sub-keV range. As the discriminating variable, the rise time parameter τ is used. A small τ parameter is associated with a normal pulse and a large parameter with a slow pulse. Different fit functions were tried out. As a result, it was found that the function using a hyperbolic tangent gives the best performance. In addition, the relation between the fit parameters of the function and quantities of the recorded pulse, e.g. the rise time or pre-trigger, were analysed. Furthermore, the distributions of the different fit parameters were studied. Not all peculiarities found in the analysis could be explained within this work and further work is necessary to fully understand them.

(ii) Validation of the rise time fit: Multiple checks were performed during this thesis in order to validate the rise time method. First, a visual inspection of the different event populations was carried out. Afterwards, a rough analytical estimation of the relative contribution of normal and slow pulses (SSE) to the total number of events was performed based on the attenuation law. As a result, a 10% agreement is obtained compared to the estimated numbers from the experimental data. In addition, a comparison of the relative number of normal and slow pulses (SSE) with a MC simulation was performed. An agreement at the few percent level was found. The differences between the data and the MC simulation are not fully explained yet and require further work, but some possible explanations are given. It will be interesting to investigate the differences to further validate the rise time method and improve the background model. Additionally, as a further indication of the robustness of the method, it is found that the $\sim$ 10.4 keV line from internal activation appears mainly in the normal pulse (SSE) population, as expected.

(iii) Pulse features: The normal pulse population (SSE) has two sub-populations. With a preliminary simulation, it was possible to show that the difference comes from events happening at different positions inside the bulk of the diode. A full pulse simulation can help verify this hypothesis and can be used to calculate the ratio between the volumes of the detector, in which the events are sorted in different sub-populations. In addition, a pulse simulation will contribute to a better understanding of the pulse shapes and gives

the opportunity to improve the method to calculate the cut efficiencies due to a better knowledge of the relative contribution of both sub-populations. Vice versa, the recorded pulse shapes will help to validate the full pulse simulation.

(iv) Pulse shape as monitoring tool: Also, it was shown that the pulse shape analysis and the related τ parameter can be used as a monitoring tool for the performance of the diode and preamplifier. For example, if the preamplifier is not tuned correctly, artefacts can be immediately identified from the τ vs. energy plots. Therefore, one can benefit from monitoring, e.g. the stability of the mean τ position of the normal pulse (SSE) population. Furthermore, it is essential that this quantity stays stable over time to apply the same PSD-cut to the complete ON and OFF data, recorded over more than 1.5 years. It was shown that the τ parameter is stable within 0.8% relative to the mean value for all detectors, except for C2, over a period of three months. For C2, a slight drift of 0.8% is observable and thus, further monitoring is required.

(v) Pulser studies and cut efficiencies: Extensive pulser studies were performed for this thesis. To mimic physical pulses in the keV and sub-keV region as good as possible, input pulses for the pulser were modelled according to real pulses provided from a Th-228 calibration measurement. However, the electronic response of the preamplifier and DAQ has not yet been considered, leading to small differences in the rise time between the Th-228 and pulser measurement. In future work, the electronic response will be taken into account to reproduce the data correctly. The pulser studies were used to study the very low energy range and to determine the energy until the fit can distinguish physical pulses from noise, resulting in a determination of a lower threshold of ~ 200 eV. Moreover, the pulser measurements are used in a newly developed method to calculate the PSD-cut efficiencies, including the associated systematic uncertainties. For this method, pulser measurements at different energies are conducted and for each energy point, the τ distribution is modelled by a function. Next, the model parameters are estimated from physical data. A cut in terms of a $\log_{10}(\tau_{\text{cut}})$ value can be derived from these models for any desired efficiency. The systematic uncertainties are calculated by propagating the uncertainties of the model into the efficiency calculation. As systematic uncertainties, the model parameter uncertainties estimated from the physical data, the stability of the τ distribution and the uncertainty due to the model choice are included. The uncertainties regarding the model parameters are dominant and are coming from the calibration with physical data. The anchoring of the model to physical data was required due to the missing modelling of the electronic response. By including the electronic response, a better knowledge of the distributions will be reached in the future, allowing to get rid of the anchoring to physical data and thus drastically reducing the model parameter uncertainties. In addition, the calculation of the cut efficiency is only performed down to energies of 300 eV. The reason for this is that the assumptions, related to the impact of the noise, to use the models at lower energies have not been validated yet. Future work will investigate if these assumptions hold true to allow the calculation of the cut efficiency for energies below 300 eV. In the end of the thesis, an example PSD-cut applied to CONUS reactor-ON data is shown. In future work,

a figure of merit could be defined and maximized or minimized in a scan over different cut efficiency values in order to find the most advantageous efficiency for each energy.
(vi) SSE and MSE discrimination: As a by-product, the rise time method can be used at MeV scale to discriminate between SSE and MSE. Several tests were performed to confirm that the vertical bands visible in the τ vs. energy plots at high energy consist of MSE. A first exemplary cut showed that similar MSE rejection efficiencies can be achieved with the rise time method, as with the A/E method. In contrast to the A/E method, the rise time fit works at MeV and sub-keV energies and enables simultaneously a slow pulse and MSE rejection. This shows the universality of this method. However, further work is necessary to use the rise time method for SSE and MSE discrimination and the comparison with the A/E method needs to be done more carefully. Also, if the rise time fit should be used for MSE discrimination, a method to define a cut and calculate the efficiencies has still to be developed.
(vii) Implementation: The rise time method is implemented as a mixture of Python and ROOT (ROOT libraries in C++) code and is used by the CONUS collaboration in the data processing chain. Also, the pulser method to calculate the cut efficiency is implemented as a ROOT macro, only taking as an input a setup file with the model names and parameters. The collaboration can use the macro to update the efficiency calculation after the electronic response is included or to calculate the efficiencies for the detectors C2-C4. Within this thesis, the calculation of the cut efficiencies was only done for C1 as a benchmark detector, meaning that the pulser studies and calculation of the cut efficiencies still need to be repeated for the detectors C2-C4. Furthermore, the PSD-cut needs to be included in the analysis chain of RUN-5 data.

Besides the further work mentioned above, other interesting investigations can be done in the future. It would be interesting to study the influence of the PSD-cut on the shape of the spectrum. If the shape of the background and CEνNS spectrum are similar, the likelihood used for the analysis is degenerated, resulting in a worse sensitivity than for a non-degenerated likelihood. Therefore, it will be interesting to investigate if the PSD-cut will create a significant shape difference and thus, increases the sensitivity. Furthermore, the interaction of neutrinos in the active volume close to the transition layer could be studied. In this case, some charge carriers can also be created inside the transition layer, leading to a potential change of the pulse shape. It would be of interest to investigate if this border effect can be neglected or needs to be taken into account for the PSD-cut efficiency. In general, an improvement regarding the discriminating power of the pulse shape analysis at low energies could be achieved by reducing the noise level. With a lower noise level, the pulses can be better distinguished by the fit, leading to a better discrimination.

Summary of the main results
The pulse shape analysis presented in this thesis helped to build a better understanding of the pulses created in the Ge detectors. It was shown that with the here introduced rise time

method, a differentiation of normal and slow pulses is possible down to energies of ~ 200 eV. This includes the complete region of interest of the CONUS CEνNS analysis. Lower energies are not of interest because the trigger efficiency of the used DAQ becomes very small for lower energies and noise events largely dominate over physical events. Moreover, in the thesis, a new method was presented to define a PSD-cut and calculate the efficiencies and corresponding systematic uncertainties. With a realistic PSD-cut, it was shown that a cut efficiency of 99% down to energies of 1.5 keV is achievable for the bulk/normal signals while rejecting the majority of the slow pulses. In addition, it was shown that an additional background suppression of around 23% in the region of interest for the CEνNS and neutrino nucleus scattering BSM analysis ($0.3-2$ keV) can be achieved through PSD. For the region of interest used in the electron neutrino scattering BSM analyses ($2-8$ keV), a reduction of around 22% is possible. In order to apply the PSD-cut at energies below 300 eV, where the noise has a non-negligible contribution, it has been shown that a good knowledge of the DAQ chain response is necessary. Furthermore, the rise time fit can be used at keV and sub-keV energies for slow pulse, and at the MeV scale for MSE and slow pulse discrimination, demonstrating the universality of this approach.
However, the possible background reduction from the application of the PSD-cut is intrinsically limited by the background composition. Not all background events occur inside the transition layer and thus cannot be distinguished from neutrino induced events. An example are neutrons, which interact in the detector nearly homogeneously. For the CONUS experiment, the dominant background contributions come from μ-induced neutrons in the shield and from the decay of ^{210}Pb in the cryostat and shield. The latter dominant contribution can be reduced by the PSD-cut. Moreover, the PSD helps to improve the understanding of the background model and to reduce its systematic uncertainties.
In conclusion, the introduced PSD will increase the sensitivity for CEνNS and brings the CONUS experiment one step closer to a possible detection of this interaction.

Appendix A.

Additional Information

In this chapter, additional information and analyses are presented. First, an overview of the frequently used measurements will be given (section A.1). Then, the influence of different data window sizes on the rise time fit results will be discussed (section A.2). Afterwards, the implementation of the fit routine (section A.3) and the calculation of the PSD-cut efficiencies, including the systematic uncertainties (section A.4), will be described briefly.

A.1. Frequently Used Measurements

In this section, the mainly used measurement are shortly explained. An overview of important facts about the three measurements can be found in Tab. A.1.
Pulser: For this measurement, the Tektronix AFG 3252 Dual Channel Arbitrary/Function Generator [52] is connected to the test input of the preamplifier. The test input allows to send generated pulses through the electronic processing chain. As a result, it enables to test the electronic response. Due to the Pulser, we have control over the input pulse shapes, the energies of each event and the frequency in which the pulses are generated. Therefore, we know what kind of pulses and how many of them are expected in the measurement. Moreover, the measurements are not statistically limited.

Th-228: During every shift at the experimental site, a calibration measurement with a Th-228 source is performed. The calibration is used to measure the stability of a Th-228 peak position over time in the high energy regime with the Lynx. The CAEN is operated in the low energy regime, allowing to use these measurements to study, e.g. the distribution of the fit parameters (see section 3.2.4). Due to the Th-228 source, the measurement is dominated by γ-rays. The measured pulses come from the Ge diode such that we have no control over the pulse shapes. In comparison to the pulser measurements, the Th-228 measurements are statistically limited.

Reactor: Until the time of writing, only reactor-ON data from RUN-5 with pulse shape information is available. After the shut down of the power plant at the end of December 2021, reactor-OFF data will be collected as well. These measurements are used for the physical analyses and are running continuously between the shifts. Both the reactor-ON and OFF data is dominated by two background contributions: μ-induce neutrons and ^{210}Pb decay products (see section 2.4.4). Due to the low background level, the count rate is very low and of the order of 10 counts $\mathrm{day}^{-1}\,\mathrm{kg}^{-1}$ in the sub-$\mathrm{keV}_{\mathrm{ee}}$ region [19]. Therefore,

Table A.1.: Summary of important facts about the frequently used measurements.

Pulser	**Th-228**	**Reactor**
on demand	each shift	running between shifts
control over input pulses	physical pulses	physical pulses
statistically unlimited	statistically limited	statistically limited
	dominated by γ-rays	dominated by μ-induce neutrons and ^{210}Pb decay products

Table A.2.: Used time segment of the recorded pulses to test the influence of different data window sizes on the fit result.

	start point [ns]	end point [ns]
first part	1000	20000
	2000	20000
second part	0	19000
	0	15000
	0	10000
uncut pulse	0	20000

these measurements are statistically limited. Like the Th-228 measurement, the pulses are created inside the Ge diode and we have no control over the pulse shapes.

A.2. Influence of Different Window Sizes on the Rise Time Fit

Looking at the size of the output files created by the fit, we see that the recorded pulse shapes contribute the most. Due to limited space on the hard drive at KBR, it was investigated if it is possible to reduce the window size of the recorded pulse in order to save storage. For this investigation, a Th-228 measurement recorded with C1 was fitted multiple times. Each time the fit was applied, the used time span of the fitted pulse was changed to simulate a different recorded time window. From the fits, we can extract how much of the recorded time window can be neglected until the fit results change significantly. The investigation is split into two parts. For the first part, the data window is reduced at the beginning, while for the second part, the window is reduced at the end of the pulse. The unreduced data window has a recorded time length of $t_{\text{window}} = 20000$ ns. For the first part, two reduced cases and the unreduced case are compared. The used start and end points of the reduced pulses can be found in Tab. A.2. More reduction is not considered because, in the most aggressive case already the majority of the baseline is cut. Since only the baseline is cut for the first comparison, the most meaningful parameter to look at is

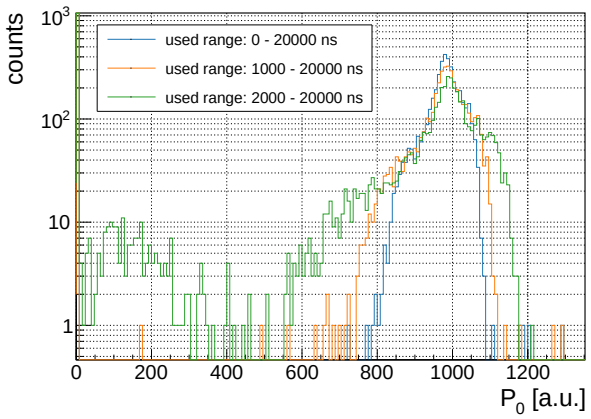

Figure A.1.: P_0-distributions for the same Th-228 measurement, recorded with C1, but different data windows were used for the fit. For this plot, two cases where the pre-trigger is reduced are compared to the uncut case.

the baseline estimate P_0. A plot of the P_0-distribution for the three different cases can be seen in Fig. A.1. Figure A.1 shows exactly what we would expect. The P_0-distribution gets wider if a larger fraction of the baseline is cut because important information about the baseline is lost. For the most extreme cut with a starting point of $t = 2000$ ns, some events cluster at P_0 values around 200 a.u. and smaller. These events come from fits of unphysical events and appear only for the maximally reduced pulse because for pulses with a longer baseline, the fit of these events does not converge. Also, these events lead to an artefact in the rise time and A_0-distribution and are correlated to the TRP reset. Figure A.1 shows that a certain baseline is needed to get enough information about the P_0 parameter. In conclusion, the pre-trigger should not be shortened.

For the second part, the exponential decay is reduced. Three cases are compared to the uncut pulse. The used start and end points of the reduced pulses can be found in Tab. A.2. Only some part of the exponential decay is cut. Therefore, it is most interesting to look at the τ_c parameter. A τ_c-distribution for the three cases is shown in Fig. A.2. The figure shows that the largest change in the τ_c-distribution occurs for the pulse with the largest cut. In this case, the peak, mainly containing slow pulses, move further to the left. Due to the reduced exponential decay, the fit prefers a different τ_c value for slow pulses. For the other two cases, only minor changes are observed.

For both parts described above, the discriminating power of the rise time parameter did not deteriorate significantly. However, some significant changes in other fit parameters can be observed. In conclusion, in principle, the exponential decay could be shortened a bit but not as extreme as tested with the largest cut shown in Fig. A.2. But, the pre-trigger should not be shortened. Especially for the lower energy pulses, all information available can help to constrain the fit. Therefore, we decided not to reduce the recording time and leave the time window recorded by the CAEN at 20000 ns.

For the CONUS experiment, the storage issue was solved by writing a program, which deletes the recorded pulse shapes of the noise events.

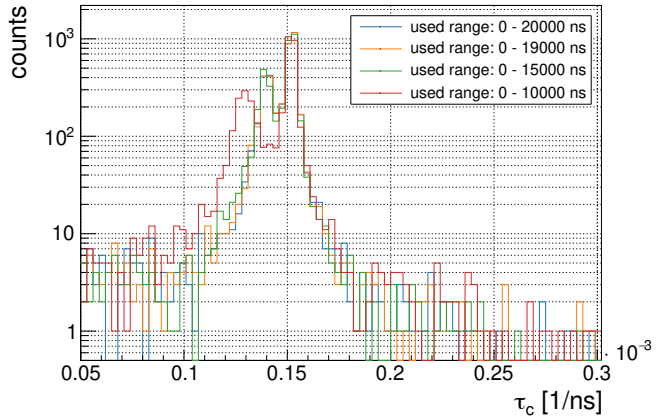

Figure A.2.: τ_c-distribution for the same Th-228 measurement, recorded with C1, but different data window sizes were used for the fit. For this plot, three cases where the exponential decay is reduced are compared to the uncut pulse.

A.3. Implementation of the Fit Routine

In this section, an overview of the implemented rise time fit routine is given. A schematic overview of the implementation can be seen in Fig. A.3. The fit routine is started with the python program *risetime.py*, which takes 6 mandatory and one optional argument as an input. The mandatory arguments are: 'path', 'filename', 'min', 'max', 'files per job' and 'energy cut'. As the input 'path', the directory where the data is stored must be specified. In order to lose as little amount of data as possible if the DAQ crashes, several data files are produced during data taking. Therefore, if the DAQ crashes, only the current file is lost. Each file has the same file name and only the ending is changing. After the zeroth file, the ending changes from *'.root'* to *'_n.root'*, where n is the number of the saved file. For the argument 'filename', the name of the data file with the *'.root'* ending needs to be taken. The input arguments 'min' and 'max' specify the lowest and highest file number of the recorded data, which should be fitted. In order to decrease the run time of the rise time fit on the cluster, the job can be split. With the mandatory argument 'files per job', the splitting in multiple cluster jobs is managed. For the argument, the number of files processed per cluster job should be given. The last mandatory argument defines the event's energy for which the fit is applied, meaning that events with a lower energy will not be fitted. Also, this can be used to decrease the run time of the fit by avoiding fitting too much noise. The optional argument gives the possibility to decide if the τ_c parameter is used as a fixed or free parameter. If an optional argument is provided, all events with an energy below $E = 8000$ ADC are fitted with τ_c as a fixed parameter (see section 3.2.3). First, the python program checks if the output folder exists. If this is the case, the program checks if the data is already fitted to avoid overwriting the existing files. In the case where the folder does not exist, an output folder with the name *Risetime* is automatically created. The output folder is located in the directory where the rest of the

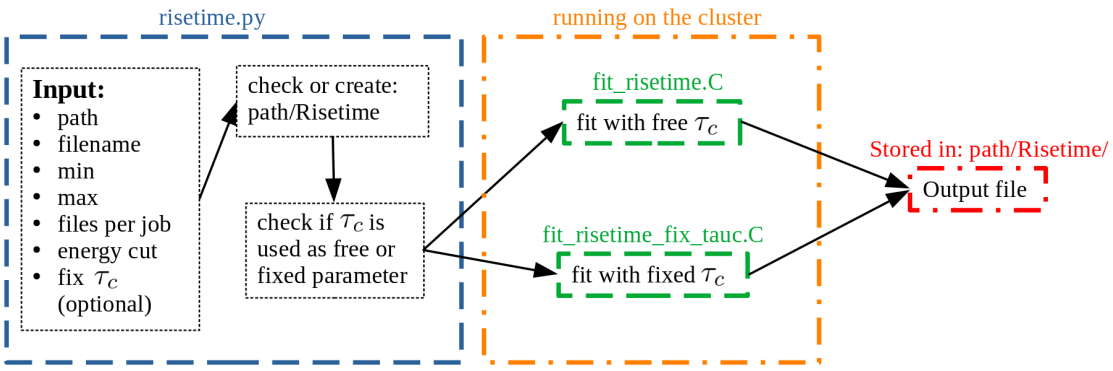

Figure A.3.: Schematic overview of the implemented fit routine. The input parameters are the path where the data is stored (path), the name of the data files (filename), the minimal and maximal number of data files which should be fitted (min, max), the number of files per cluster job (files per job), the lowest energy for which the events are still fitted (energy cut) and the optional argument which determines if τ_c is fixed in the fit or not (fix τ_c). If the optional argument is not given, the fit will be performed with τ_c as a free parameter.

data is stored. Afterwards, the program starts the fit routine on the cluster. The actual fit routine is written as a ROOT [21] macro. If τ_c is used as a free parameter, the macro *fit_risetime.C* is used; otherwise, the macro *fit_risetime_fix_tauc.C* will be selected. The fit results are saved in a separate output file, with the same name as the data file, but the ending changes to *'_risetime.root'*. All output files are stored in the output folder. In the following, the fit routine and output file will be described in more detail.

Fit routine: The program loads one file and processes the file before the next one is loaded. After loading a file, the program goes through each event separately. First, two checks are applied to the events to decide if the current event should be fitted or not. The first check is an energy scale cut, which is defined by an input parameter. The second check controls if the maximal height of the pulse appears before a time of 1000 ns and is applied to avoid fitting events like shown in Fig. 2.15 f). Only events passing these two checks are fitted. For the failed events, all fit parameters are set to -1 and are saved in the output file. By looking at events with fit parameters equal to -1, it can be seen that the two cuts are working well. After the two checks, the starting fit values for the different fit parameters are estimated. For all parameters except τ_c, the starting values are estimated from the pulse. The starting value for the τ_c parameter is set to a specific value for all pulses. Then, the fit is performed and the program checks automatically if the fit converged. Measures to ensure a covered fit are, e.g. checking the fit status given by ROOT and if the errors of the fit parameter are 'NAN'. If the fit does not converge, the procedure is repeated up to 10 times. After being repeated 10 times, a value of -2 will be saved for all fit parameters. An estimation for the percentage of events with the fit parameters equal to '-2' can be

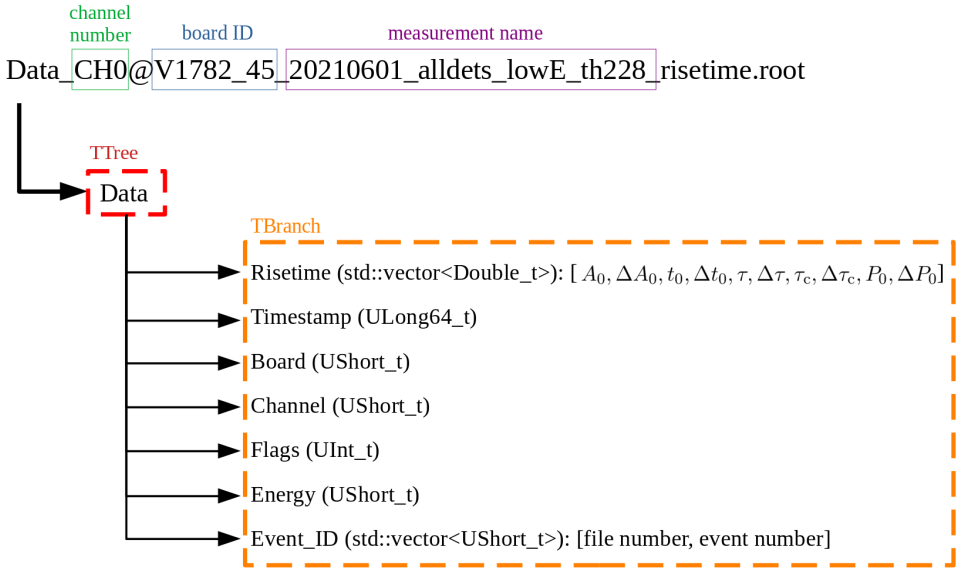

Figure A.4.: Schematic overview of the structure of the output file created by the fit routine. For n>0, the filename becomes: *Data_CH0@V1782_45_20210601_alldets_lowE_th228_n_risetime.root*. The branch *Timestamp* contains the timestamps of the events, *Board* contains the board ID, *Channel* contains the numbers of the channels used for recording the event, *Flags* contains numbers, e.g. marking saturation or pile-up events, *Energy* contains the energy of each event, *Event_ID* contains two numbers, making it possible to identify the event and *Risetime* contains the fit parameters and errors of each event.

found in Tab. 3.1. Events with a non-converging fit are mainly looking like noise events and unphysical pulses. The unphysical pulses are correlated to the TRP reset. In the end, together with more information about the event, the fit parameters are saved in a separated output file. All fit parameters per event are saved in one array in the following ordering: $A_0, t_0, \tau, \tau_c, P_0$, with value and fit error alternating. A separate output file is created such that the original data stays untouched.

Output file: A schematic overview of the output file structure can be seen in Fig. A.4. Similar to the data files, the output files are in the *.root* data format and have the same structure. The information is saved in the tree *Data*. All information from the data file, except the pulse shape, are saved in the same way in the output file. The pulse shape is not saved again to reduce the size of the files. In addition, to the information from the data file, the arrays with the fit parameters and an event ID are saved in the output file. The event IDs are two numbers corresponding to the file number and event number inside the file. These two numbers allow to relate the fit parameters to a pulse shape. If the data is calibrated, an additional branch can be added, including the calibrated energies.

A.4. Implementation of the Efficiency Calculation

In this section, a short explanation of the implementation of the efficiency calculation will be given. The calculation of the cut efficiency, including the systematic uncertainties (without the model uncertainty), is done with the ROOT [21] Macro *cut_efficieny.C*. As an input for the macro, a setup file containing information about the models is needed. The information included in the setup file is the type of the model, the energy of the pulser point and the model parameter, including the uncertainties. The structure of such a setup file is shown in Fig. A.5. With the macro five output files can be generated per model included in the setup file. Three files are plots showing the efficiency curve, the relative uncertainty contribution and the lower and higher population model. Another file (*.csv*) contains a table with the cut efficiency, the systematic uncertainty and the $\log_{10}(\tau_{\text{cut}})$ value. In addition, the header of the table includes information about the model and the energy of the measurement. In the last file, the relative uncertainty plot is stored in the *.root* format. The file is necessary to update the relative uncertainty contribution plot after the model uncertainty is calculated. Another input of the macro is the location where these files are saved.
In order to calculate the model uncertainty, a second ROOT macro is necessary (*model_error.C*). Again, the macro takes a setup file as an input. The setup file needs to have the same format as the previous one. If a model uncertainty should be calculated for a measured energy, the setup file needs to include the information about the alternative model. In addition, the path where the old efficiency curve and relative uncertainty plot are saved is necessary as an input to load and update the table and plots. As the output, three files are created, the updated versions of the table including the data, the efficiency curve and the relative uncertainty plot.

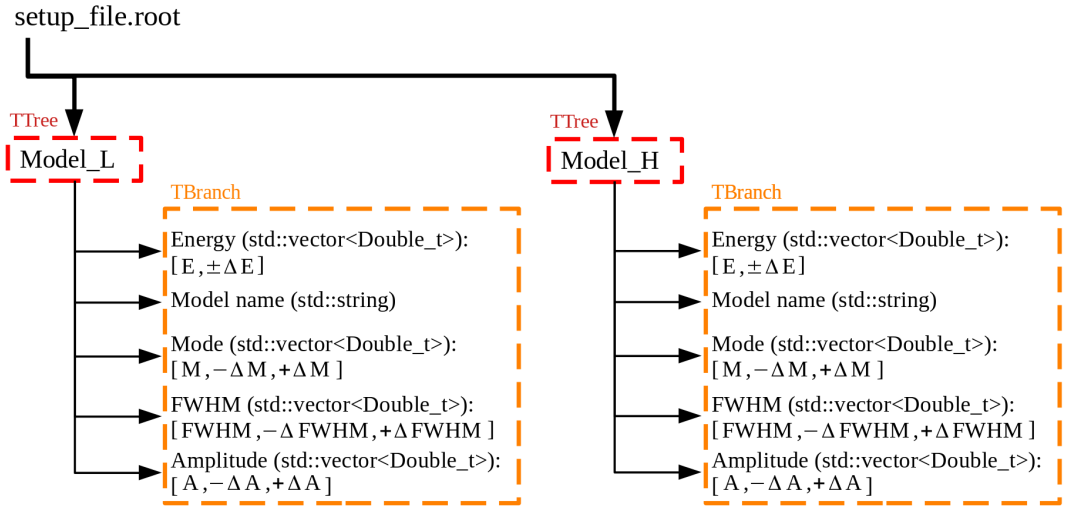

Figure A.5.: Schematic overview of the setup file's structure needed for the cut efficiency calculation. In the branch 'Model name', the name of the models ('gauss', loggauss' or 'loggaussgauss') are stored.

Additional Plots

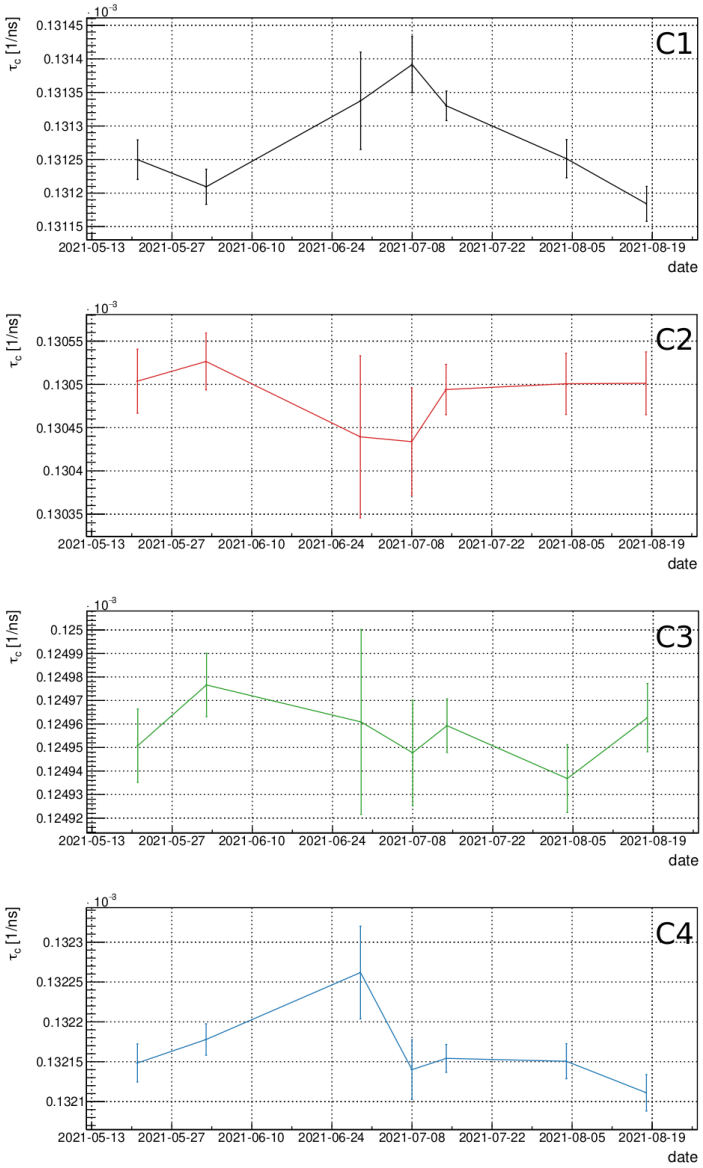

Figure B.1.: Stability of the τ_c parameter in time for all four CONUS detectors. From top to bottom, the stability plot of the detectors C1 to C4 are shown. For the estimation of the parameter, reactor-ON data is used. On the x-axis, the starting date of each measurement is plotted.

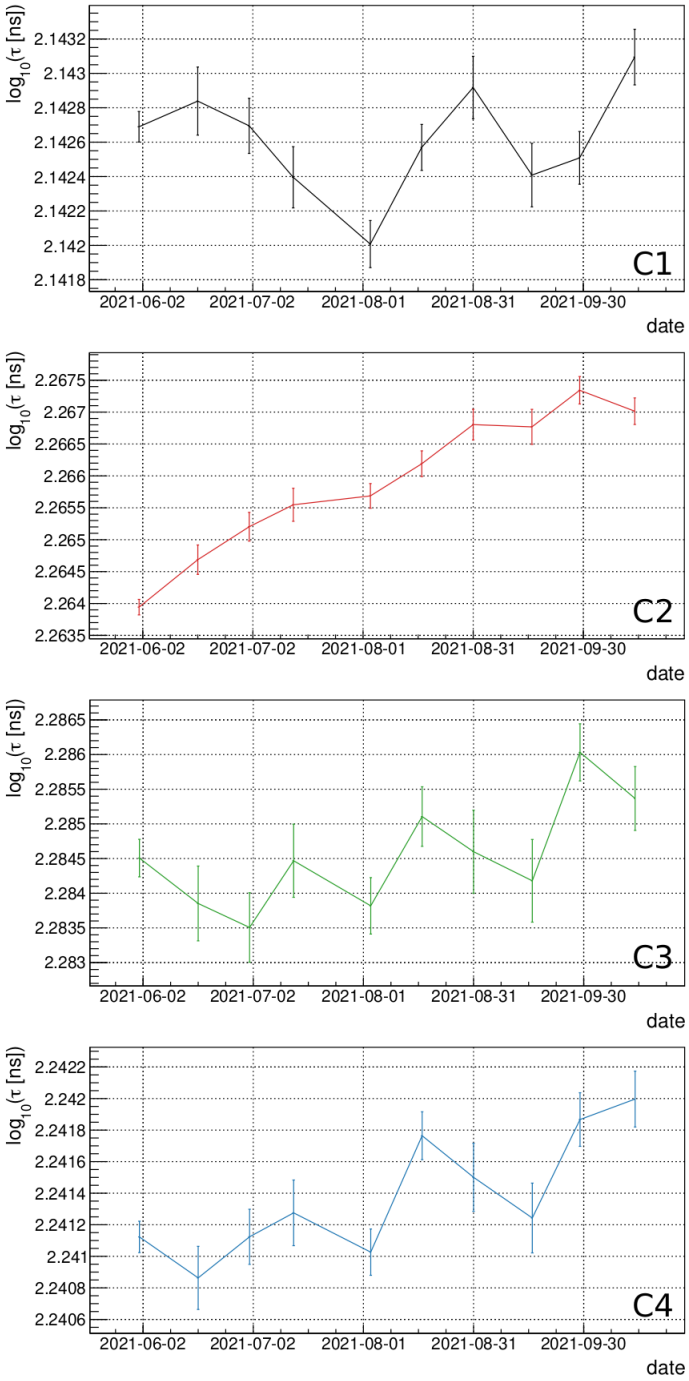

Figure B.2.: Stability of the τ parameter in time for all four CONUS detectors. From top to bottom, the stability plot of the detectors C1 to C4 are shown. For the estimation of the parameter, Th-228 data is used. On the x-axis, the date of each measurement is plotted.

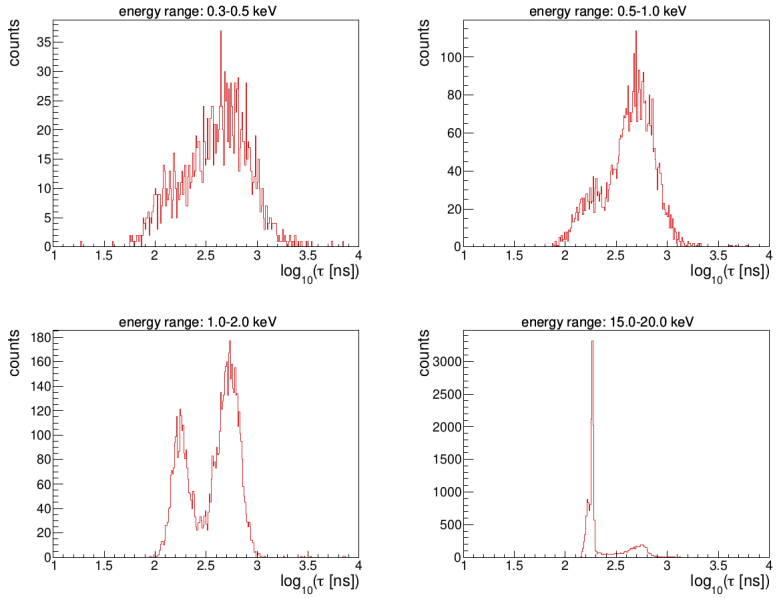

Figure B.3.: $\log_{10}(\tau)$-distributions for the C2 detector at different energies. For the shown plots, all Th-228 calibration measurements between 01.06.2021 and 17.08.2021 are used.

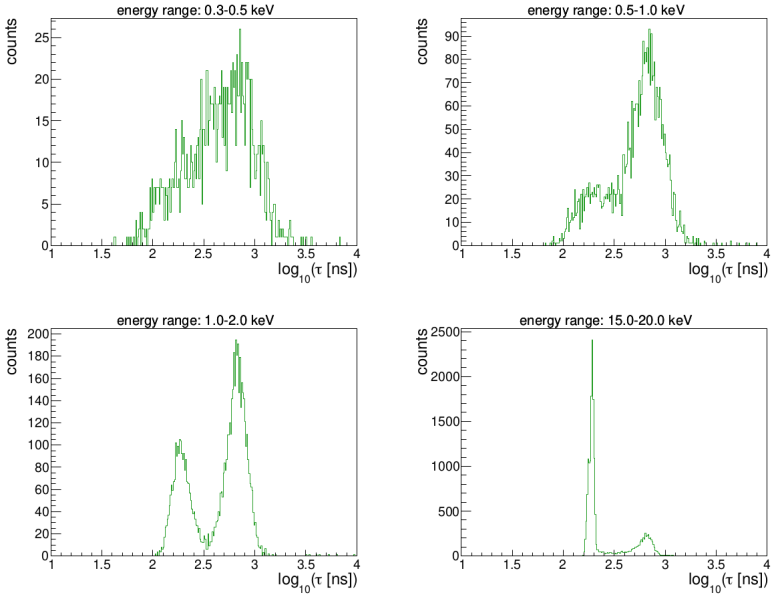

Figure B.4.: $\log_{10}(\tau)$-distributions for the C3 detector at different energies. For the shown plots, all Th-228 calibration measurements between 01.06.2021 and 17.08.2021 are used.

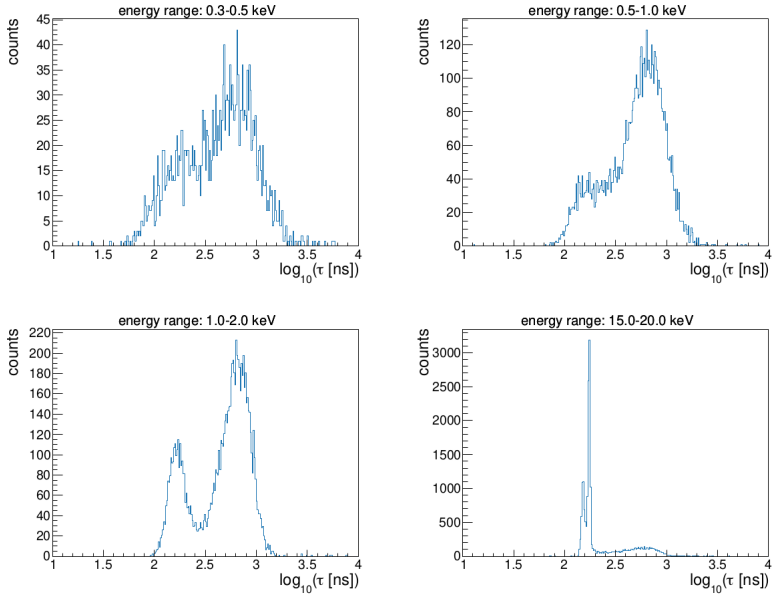

Figure B.5.: $\log_{10}(\tau)$-distributions for the C4 detector at different energies. For the shown plots, all Th-228 calibration measurements between 01.06.2021 and 17.08.2021 are used.

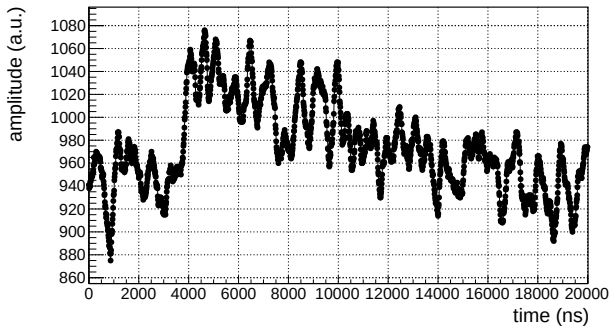

(a)

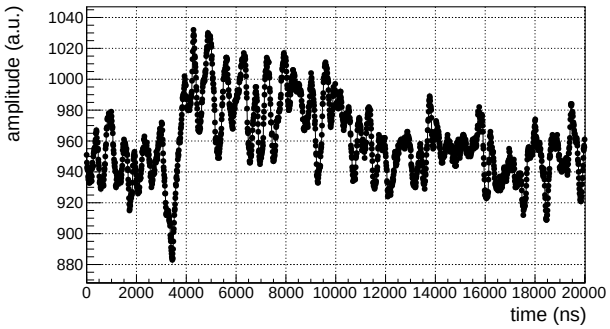

(b)

Figure B.6.: Two example pulses at low energy, recorded with the C1 detector. In figure a), the pulse has an energy of $E \approx 370$ eV and in figure b), the pulse has an energy of $E \approx 215$ eV.

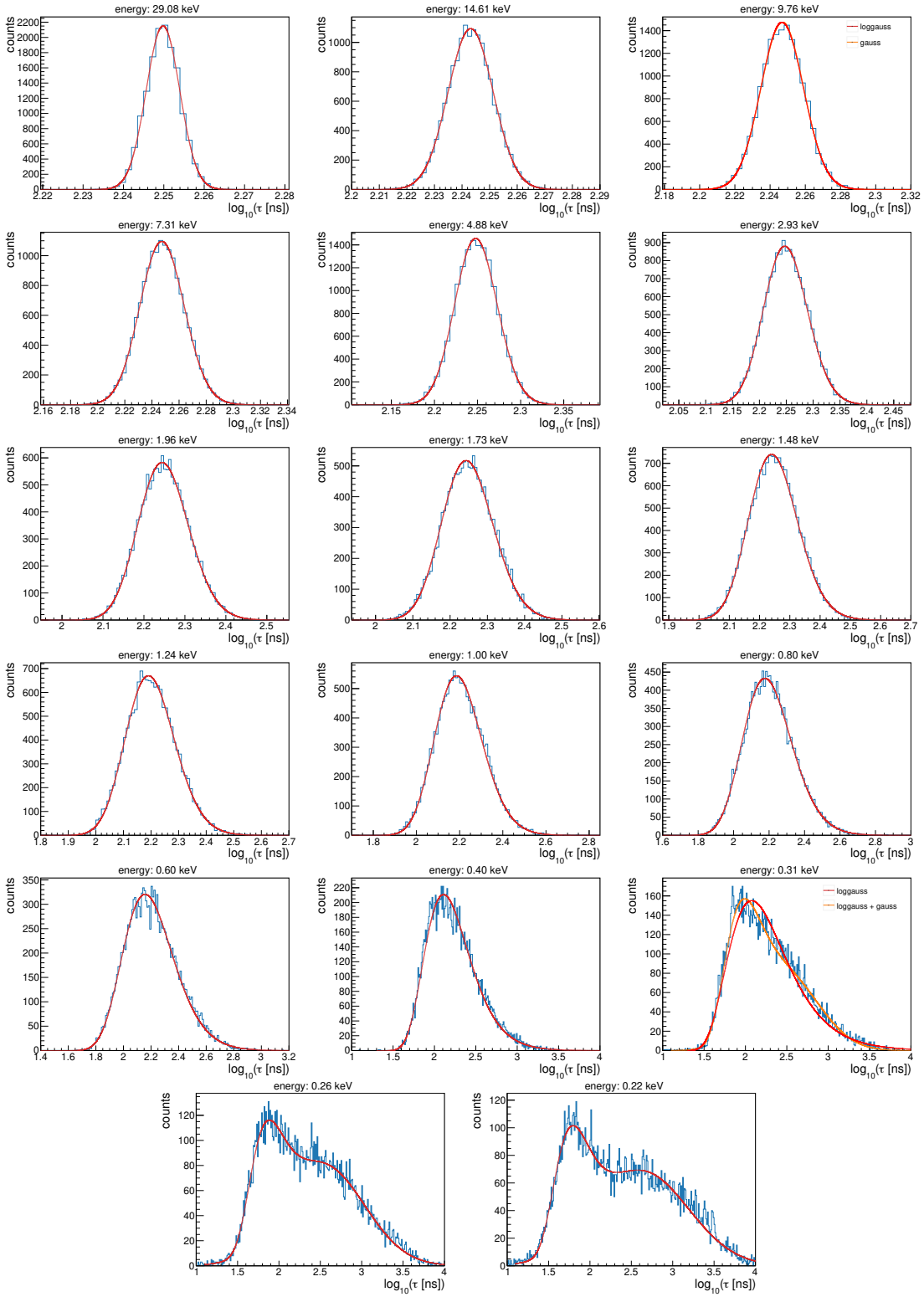

Figure B.7.: τ-distribution with the corresponding fitted model for the higher population of the pulser measurement for all measured energy points. For the two energies where a model uncertainty is calculated, the fit of both models is shown. All shown plots are for the C1 detector.

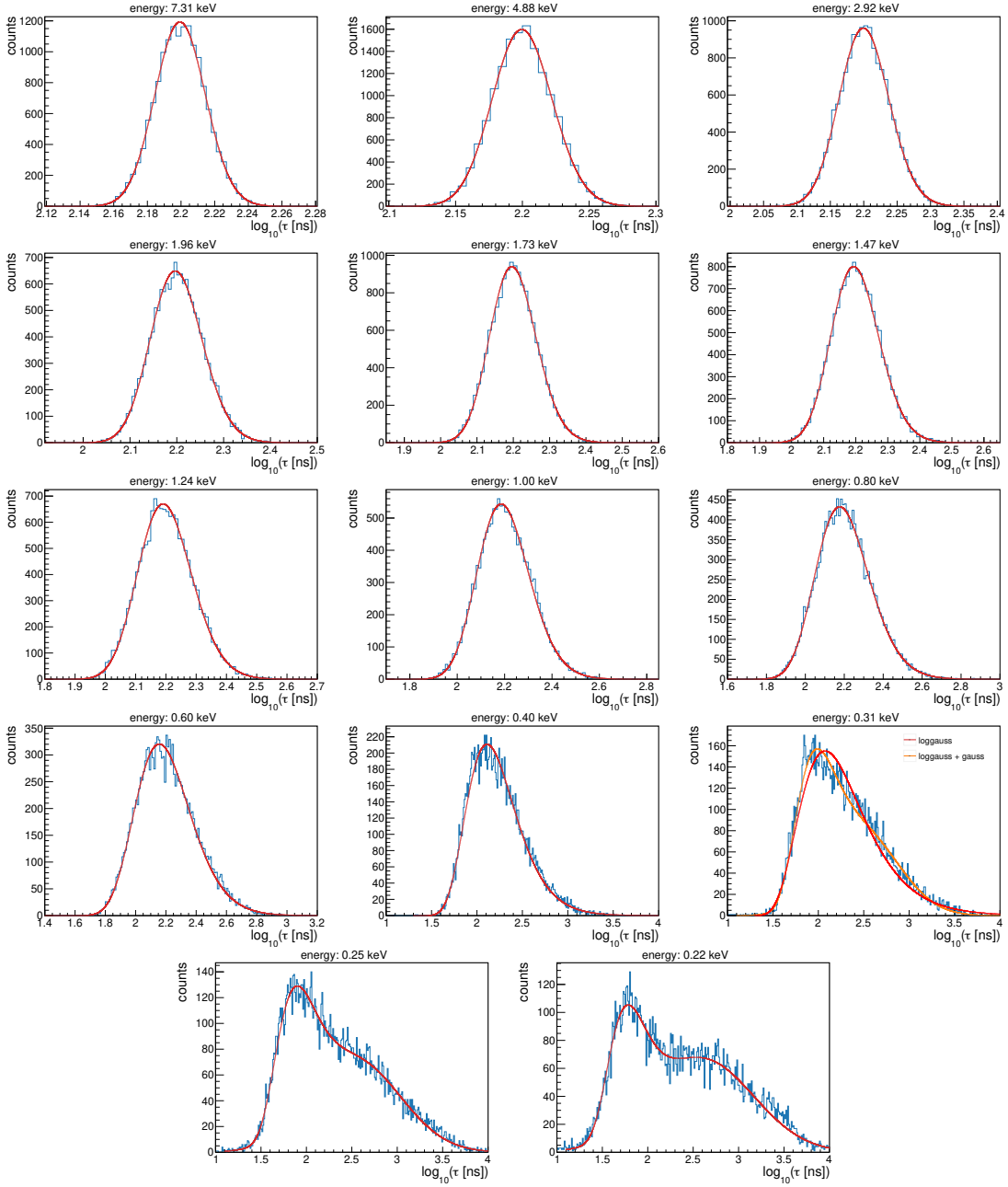

Figure B.8.: τ-distribution with the corresponding fitted model for the lower population of the pulser measurement for all measured energy points. For the two energies where a model uncertainty is calculated, the fit of both models is shown. For the three highest energy points, the model is fixed and therefore, the three models are not shown in this plot. All shown plots are for the C1 detector.

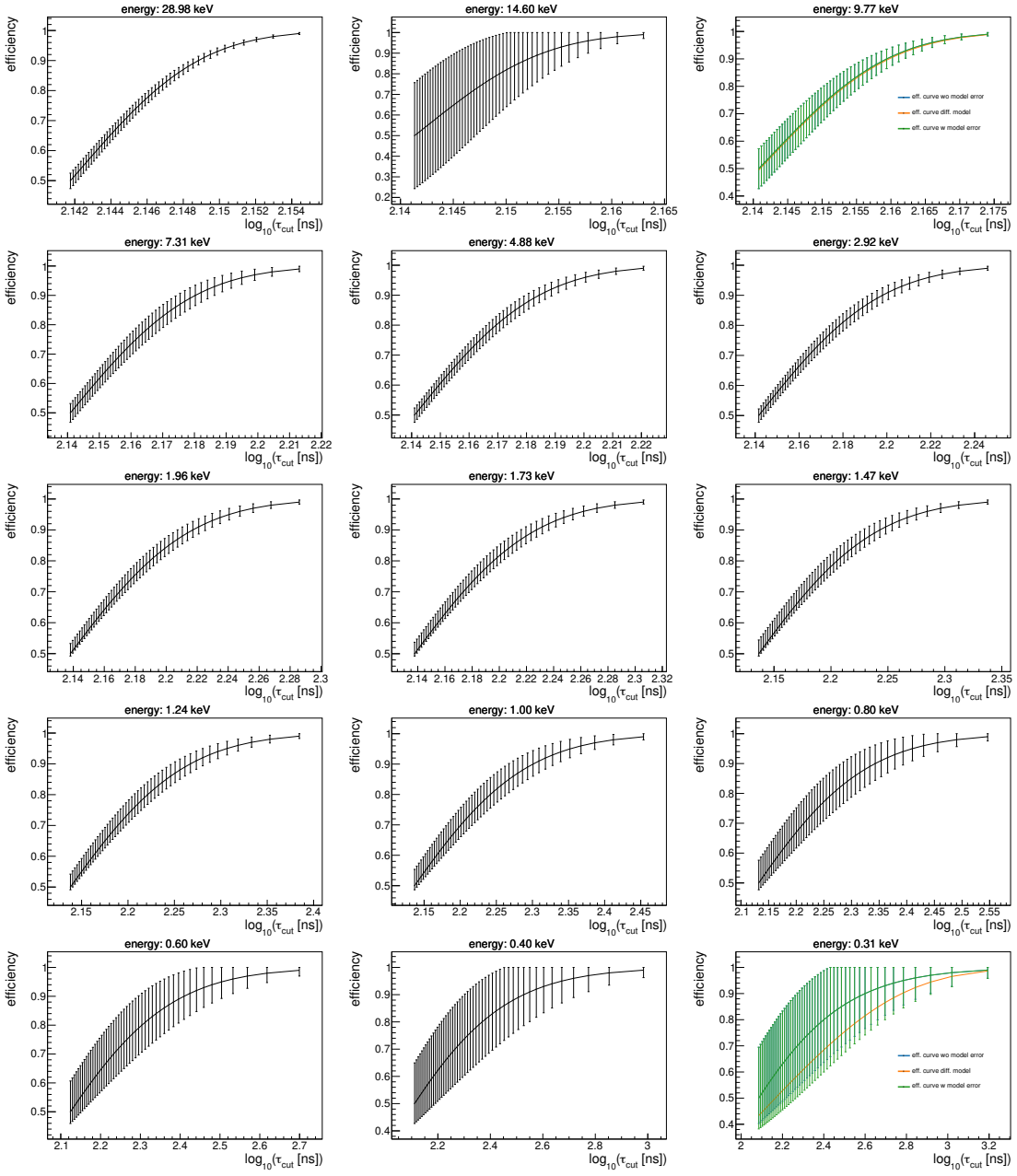

Figure B.9.: PSD-cut efficiency curves for all measured energy points. All shown plots are for the C1 detector.

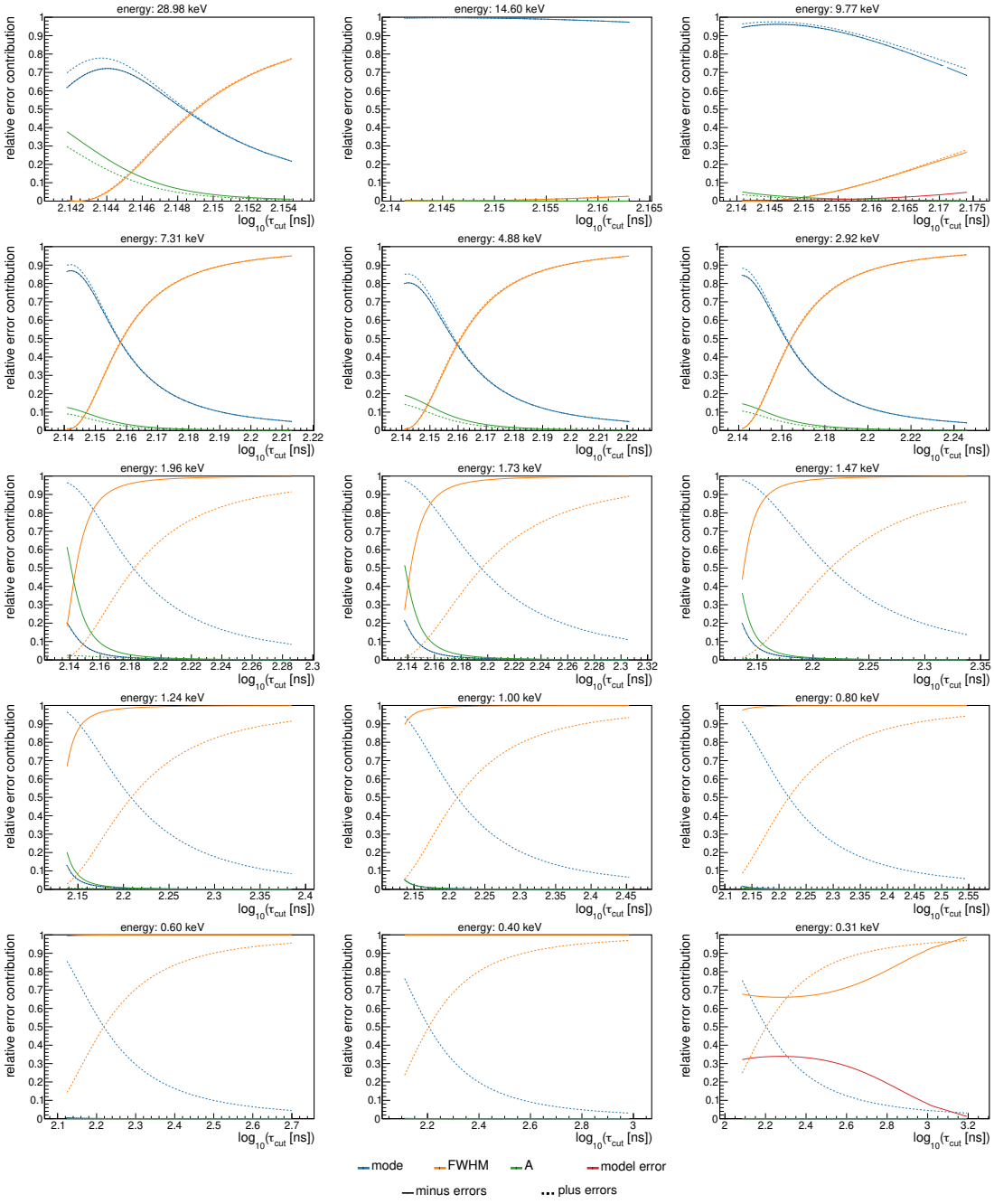

Figure B.10.: The relative contribution from the systematic uncertainties used for the efficiency calculation for all measured energy points. The uncertainty regarding the stability of the τ-distribution is included in the mode uncertainty. A comparison of this uncertainty relative to the uncertainty of the mode parameter can be found in Fig. 4.17. All shown plots are for the C1 detector.

Appendix C.

Supplementary Calculations

In the following, all calculations necessary to the understand formulas discussed in the main part of the thesis are shown.

C.1. Relations Between the Fit Parameters

Before the relations of the different fit parameters are calculated, the first and second derivative of the fit function is shown. Both derivatives will be needed for further calculations. The first derivative is:

$$\frac{\mathrm{d}}{\mathrm{d}t}f(t) = A_0 \left(\frac{1}{\tau} \left[1 - \tanh^2 \left(\frac{t-t_0}{\tau} \right) \right] - \left[\tanh \left(\frac{t-t_0}{\tau} \right) + 1 \right] \tau_\mathrm{c} \right) \exp\left(-\tau_\mathrm{c} \left(t - t_0 \right) \right). \tag{C.1}$$

The second derivative is:

$$\begin{aligned} \frac{\mathrm{d}^2}{\mathrm{d}t^2}f(t) = A_0 \Bigg[& -\frac{2\tanh\left(\frac{t-t_0}{\tau}\right)\left(1-\tanh^2\left(\frac{t-t_0}{\tau}\right)\right)}{\tau^2} + \tau_\mathrm{c}^2 \left(\tanh\left(\frac{t-t_0}{\tau}\right) + 1 \right) \\ & - \frac{2\tau_\mathrm{c}}{\tau}\left(1-\tanh^2\left(\frac{t-t_0}{\tau}\right)\right) \Bigg] \exp\left(-\tau_\mathrm{c}\left(t-t_0\right)\right). \end{aligned} \tag{C.2}$$

relation between rise time and τ:
Next, the relation between the rise time and the τ parameter of the simplified fit function (see eq. 3.14) is calculated. The maximal value of the simplified fit function is $2A_0$. Therefore, we can define the time t_{10} when the pulse reaches 10% of the maximal height as:

$$f(t_{10}) = A_0 \left[\tanh\left(\frac{t_{10}-t_0}{\tau} \right) \right] = 0.1 \times (2A_0) \tag{C.3}$$

The parameter A_0 can be cancelled on both sides of the equation and the resulting function can be solved for t_{10}:

$$t_{10} = \tau \mathrm{artanh}(-0.8) + t_0 \tag{C.4}$$

The same calculation can be done for the time t_{90} when the function reaches 90% of its maximal height. The resulting formula for t_{90} is:

$$t_{90} = \tau \text{artanh}(0.8) + t_0 \tag{C.5}$$

The rise time of a pulse is defined as the time needed to raise from 10% to 90% of its maximal height. As a result, we can take the difference of the times t_{90} and t_{10} and get the following relation between the rise time and the τ parameter:

$$t_{90} - t_{10} = \tau(\text{artanh}(0.8) - \text{artanh}(-0.8)) = \tau(\text{artanh}(0.8) + \text{artanh}(0.8)) = 2\tau\text{artanh}(0.8) \tag{C.6}$$

Solving the equation above for τ gives the relation shown in section 3.2.4.

relation between slope and τ:

Next, we calculate the relation between the τ parameter and the slope at the point t_0 for the complete fit function (see eq. 3.9). The derivative of the fit function is shown in eq. C.2. If we insert $t = t_0$ into this equation, it reduces to:

$$\frac{\mathrm{d}}{\mathrm{d}t} f(t_0) = A_0 \left(\frac{1}{\tau} - \tau_\mathrm{c} \right). \tag{C.7}$$

That is the relation shown in section 3.2.4.

relation between $f_{\max}$ and A_0:

Next, the relation between A_0 and the maximal point of the fit function is calculated. First, the time when the maximal point is reached must be calculated. This is done by setting the first derivative equal to zero and solving the equation for t. The calculation is done with Mathematica and the result is:

$$t_{\max} = t_0 - \tau \log \left(\sqrt{\frac{\tau\tau_\mathrm{c}}{2 - \tau\tau_\mathrm{c}}} \right) \tag{C.8}$$

Also, this result is shown in eq. 3.18. After that, the calculated time is inserted into the fit function and the resulting function is simplified. The simplification is done in small steps. First, the result is inserted in the hyperbolic tangent:

$$\tanh\left(\frac{t_{\max} - t_0}{\tau} \right) + 1 = \tanh\left(-\log\left(\sqrt{\frac{\tau\tau_\mathrm{c}}{2 - \tau\tau_\mathrm{c}}} \right) \right) + 1 \tag{C.9}$$

To simplify this equation further, the following relation is used:

$$\tanh(x) = \frac{e^{2x} - 1}{e^{2x} + 1} \tag{C.10}$$

Additionally, the relation $\exp(a\log(x)) = x^a$ is used. With these two relations, the equation simplifies to:

$$\tanh\left(\frac{t_{\max}-t_0}{\tau}\right)+1 = \frac{\frac{2-\tau\tau_c}{\tau\tau_c}-1}{\frac{2-\tau\tau_c}{\tau\tau_c}+1}+1 = 2-\tau\tau_c \tag{C.11}$$

Second, the time $t_{\max}$ is inserted into the exponential part of the fit function and the result is simplified:

$$\exp\left(-\tau_c\left(t_{\max}-t_0\right)\right) = \exp\left(\tau\tau_c\log\left(\sqrt{\frac{\tau\tau_c}{2-\tau\tau_c}}\right)\right) = \left(\sqrt{\frac{\tau\tau_c}{2-\tau\tau_c}}\right)^{\tau\tau_c} = \left(\frac{\tau\tau_c}{2-\tau\tau_c}\right)^{\frac{\tau\tau_c}{2}} \tag{C.12}$$

Combining the simplified hyperbolic tangent part and the exponential part to the fit function, we find the final relation between the A_0 parameter and the maximal point of the fit function. The final result is shown in eq. 3.18.

C.2. FWHM for Loggauss Model

In this section, the FWHM for the loggaus model (see eq. 4.6) will be calculated. The calculation is similar to the calculation of the FWHM for a Gaussian function. First, the maximum of the loggaus model $f_{\max}$ needs to be calculated:

$$f_{\max} = \frac{1}{\sqrt{2\pi}\sigma}e^{-\frac{\sigma^2}{2}} \tag{C.13}$$

Afterwards, the two x-values $x_{1,2}$ need to be found for which the function reaches half of its maximum.

$$\frac{1}{2}f_{\max} = f(x_{1,2}) \tag{C.14}$$

$$\frac{1}{2} = e^{-\frac{\log\left(x_{1,2}-\mu\right)^2}{2\sigma^2}} \tag{C.15}$$

$$\pm\sqrt{2\log(2)}\sigma = \log(x_{1,2}-\mu) \tag{C.16}$$

$$x_1 = \mu + e^{+\sqrt{2\log(2)}\sigma} \tag{C.17}$$

$$x_2 = \mu + e^{-\sqrt{2\log(2)}\sigma} \tag{C.18}$$

The FWHM is the difference of the two x-values calculated above and thus, the FWHM of the loggaus model is:

$$FWHM = x_1 - x_2 = e^{+\sqrt{2\log(2)}\sigma} - e^{-\sqrt{2\log(2)}\sigma} = 2\sinh(\sqrt{2\log(2)}\sigma) \tag{C.19}$$

C.3. Relation Between the Gauss and Loggauss Model

In this section, it will be shown that the gauss function (see eq. 4.3) is only the small σ limit of the loggauss function (see eq. 4.6). If the σ parameter of the loggaus model is small, also $x - M$ is small, with $M = \mu + 1$ being the Mode value. Therefore, we can use the Taylor expansion for the logarithm, but first, we rewrite the argument of the logarithm as follows.

$$\log(x - \mu) = \log(x - M + 1) = \log(1 + \Delta x), \text{ with } \Delta x = x - M \tag{C.20}$$

For small σ values, Δx is small and the Taylor expansion of the logarithm is:

$$\log(1 + \Delta x) = \Delta x + \mathcal{O}(\Delta x^2) \tag{C.21}$$

The Taylor expansion can be inserted into the loggauss function and Δx can be transformed back into μ.

$$f(x) = \frac{1}{\sqrt{2\pi}\sigma} e^{-\frac{\sigma^2}{2}} e^{-\frac{(x-(\mu+1))^2}{2\sigma^2}} \tag{C.22}$$

Since σ is very small, the prefactor $e^{-\frac{\sigma^2}{2}}$ is approximately one. In addition, by redefining the μ parameter to $\mu' = \mu + 1$, the function shown above is a gaussian distribution.

C.4. Error Propagation Formula for the FWHM Estimation

In this section, the error propagation formula for the fit function of the FWHM (see eq. 4.12) is shown. The formula is needed in order to calculate the error band of the fit. Since the parameters are strongly correlated, the error propagation formula for correlated errors is used. The general formula for the error of $y = f(x_i)$, with x_i being correlated, is [43]:

$$\Delta y = \sqrt{\sum_{i=0}^{m} \left(\frac{\partial y}{\partial x_i} \Delta x_i \right)^2 + 2 \sum_{i=1}^{m-1} \sum_{k=i+1}^{m} \frac{\partial y}{\partial x_i} \frac{\partial y}{\partial x_k} \mathrm{cov}(x_i, x_k)}, \tag{C.23}$$

with the covariance matrix being related to the correlation matrix (correlation coefficients) as follows [43]:

$$\mathrm{corr}(x_i, x_j) = \frac{\mathrm{cov}(x_i, x_j)}{\Delta x_i \Delta x_j} \tag{C.24}$$

The derivatives of the fit function with respect to the different parameters are:

$$\frac{\partial f(x)}{\partial p_0} = (x+1)^{p_1} \tag{C.25}$$

$$\frac{\partial f(x)}{\partial p_1} = p_0 \log(x+1)(x+1)^{p_1} \tag{C.26}$$

$$\frac{\partial f(x)}{\partial p_2} = 1 \tag{C.27}$$

Together with the values from the covariant matrix, the error band can be calculated.

C.5. Error Propagation Formulas for the Model Functions

In this section, the error propagation formulas for the different models regarding the cut efficiencies will be calculated. For the calculation, the standard error propagation formula is applied. The error propagation formula for the function $y = f(x_1, x_2)$ is [43]:

$$\Delta y = \sqrt{\left(\frac{\partial f(x_1,x_2)}{\partial x_1}\Delta x_1\right)^2 + \left(\frac{\partial f(x_1,x_2)}{\partial x_2}\Delta x_2\right)^2} \tag{C.28}$$

First, the cut efficiency ϵ is calculated analytically for the corresponding model with the following function:

$$\epsilon = \int_{-\infty}^{\log_{10}(\tau_{\text{cut}})} f_{\text{total}}(\log_{10}(\tau))\,\mathrm{d}\log_{10}(\tau) \tag{C.29}$$

Then, the resulting function can be inserted in the error propagation formula.
In the following, the formulas for the three different models are derived. For simplification, the rise time values will be renamed to $\log_{10}(\tau_{\text{cut}}) = x_{\text{cut}}$ and $\log_{10}(\tau) = x$ for the rest of this section.

Gauss: The solution of the integral shown in eq. C.29 for the gauss model is:

$$\epsilon(x_{\text{cut}}) = \frac{A_{\text{H}}}{2}\left[1 - \text{erf}\left(\frac{\mu_{\text{H}} - x_{\text{cut}}}{\sqrt{2}\sigma_{\text{H}}}\right)\right] + \frac{(1-A_{\text{H}})}{2}\left[1 - \text{erf}\left(\frac{\mu_{\text{L}} - x_{\text{cut}}}{\sqrt{2}\sigma_{\text{L}}}\right)\right], \tag{C.30}$$

where the indices 'H'('L') mark the higher (lower) population model parameter. With this formula, all terms needed for the error propagation formula can be calculated and the

resulting terms are shown below:

$$\frac{\partial\epsilon(x_{\text{cut}})}{\partial A_{\text{H}}} = \frac{1}{2}\left[1 - \text{erf}\left(\frac{\mu_{\text{H}} - x_{\text{cut}}}{\sqrt{2}\sigma_{\text{H}}}\right)\right] - \frac{1}{2}\left[1 - \text{erf}\left(\frac{\mu_{\text{L}} - x_{\text{cut}}}{\sqrt{2}\sigma_{\text{L}}}\right)\right] \tag{C.31}$$

$$\frac{\partial\epsilon(x_{\text{cut}})}{\partial \mu_i} = -\frac{A_i}{\sqrt{2\pi}\sigma_i}\exp\left[-\frac{(\mu_i - x_{\text{cut}})^2}{2\sigma_i^2}\right] \tag{C.32}$$

$$\frac{\partial\epsilon(x_{\text{cut}})}{\partial \sigma_i} = \frac{A_i(\mu_i - x_{\text{cut}})}{\sqrt{2\pi}\sigma_i^2}\exp\left[-\frac{(\mu_i - x_{\text{cut}})^2}{2\sigma_i^2}\right] \tag{C.33}$$

with $i \in \{\text{H}, \text{L}\}$ and $A_{\text{L}} = 1 - A_{\text{H}}$. Using eq. C.28, the terms above can be combined to the final formula for the efficiency error $\Delta\epsilon$:

$$\begin{aligned}\Delta\epsilon = \Bigg[&\left(\frac{\partial\epsilon(x_{\text{cut}})}{\partial A_{\text{H}}}\Delta A_{\text{H}}\right)^2 + \left(\frac{\partial\epsilon(x_{\text{cut}})}{\partial \mu_{\text{H}}}\Delta\mu_{\text{H}}\right)^2 + \left(\frac{\partial\epsilon(x_{\text{cut}})}{\partial \sigma_{\text{H}}}\Delta\sigma_{\text{H}}\right)^2 \\ &+ \left(\frac{\partial\epsilon(x_{\text{cut}})}{\partial \mu_{\text{L}}}\Delta\mu_{\text{L}}\right)^2 + \left(\frac{\partial\epsilon(x_{\text{cut}})}{\partial \sigma_{\text{L}}}\Delta\sigma_{\text{L}}\right)^2\Bigg]^{\frac{1}{2}}\end{aligned} \tag{C.34}$$

In addition, not σ is estimated from the Th-228 measurement but the FWHM. Therefore, the relation between the error of σ and the FWHM is also needed.

$$\Delta\sigma = \frac{\Delta FWHM}{2\sqrt{2\log(2)}} \tag{C.35}$$

Loggauss: The solution of eq. C.29 for the loggauss model is shown below:

$$\epsilon(x_{\text{cut}}) = \frac{A_{\text{H}}}{2}\left[1 - \text{erf}\left(\frac{\sigma_{\text{H}}^2 - \log(x_{\text{cut}} - \mu_{\text{H}})}{\sqrt{2}\sigma_{\text{H}}}\right)\right] + \frac{(1 - A_{\text{H}})}{2}\left[1 - \text{erf}\left(\frac{\sigma_{\text{L}}^2 - \log(x_{\text{cut}} - \mu_{\text{L}})}{\sqrt{2}\sigma_{\text{L}}}\right)\right] \tag{C.36}$$

The terms needed for the error propagation formula are shown below:

$$\frac{\partial\epsilon(x_{\text{cut}})}{\partial A_{\text{H}}} = \frac{1}{2}\left[1 - \text{erf}\left(\frac{\sigma_{\text{H}}^2 - \log(x_{\text{cut}} - \mu_{\text{H}})}{\sqrt{2}\sigma_{\text{H}}}\right)\right] - \frac{1}{2}\left[1 - \text{erf}\left(\frac{\sigma_{\text{L}}^2 - \log(x_{\text{cut}} - \mu_{\text{L}})}{\sqrt{2}\sigma_{\text{L}}}\right)\right] \tag{C.37}$$

$$\frac{\partial\epsilon(x_{\text{cut}})}{\partial \mu_i} = -\frac{A_i}{\sqrt{2\pi}\sigma}\exp\left[-\frac{(\sigma_i^2 - \log(x_{\text{cut}} - \mu_i))^2}{2\sigma_i^2}\right]\frac{1}{x_{\text{cut}} - \mu_i} \tag{C.38}$$

$$\frac{\partial\epsilon(x_{\text{cut}})}{\partial \sigma_i} = -\frac{A_i}{\sqrt{2\pi}}\exp\left[-\frac{(\sigma_i^2 - \log(x_{\text{cut}} - \mu_i))^2}{2\sigma_i^2}\right]\left(1 + \frac{\log(x_{\text{cut}} - \mu_i)}{\sigma_i^2}\right) \tag{C.39}$$

with $i \in \{\text{H}, \text{L}\}$ and $A_{\text{L}} = 1 - A_{\text{H}}$. The final error propagation formula is equal to eq. C.34, but the terms shown above for the loggaus model are inserted. Again, the relation

between the error of σ and the FWHM is also needed and given below:

$$\Delta\sigma = \frac{\Delta FWHM}{2\sqrt{2\log(2)}\sqrt{\left(\frac{FWHM}{2}\right)^2 + 1}} \tag{C.40}$$

loggauss + gauss: The solution of eq. C.29 for the loggauss gauss model is shown below:

$$\begin{aligned}\epsilon(x_{\text{cut}}) = {} & \frac{A_{\text{H}}}{1+R_{\text{H}}}\left[\frac{R_{\text{H}}}{2}\left(1-\text{erf}\left(\frac{\sigma_{1\,\text{H}}^2 - \log(x_{\text{cut}} - ((\mu_{\text{H}} - \Delta\mu_{\text{H}}) - 1))}{\sqrt{2}\sigma_{1\,\text{H}}}\right)\right)\right. \\ & \left. + \frac{1}{2}\left(1-\text{erf}\left(\frac{(\mu_{\text{H}} + \Delta\mu_{\text{H}}) - x_{\text{cut}}}{\sqrt{2}\sigma_{2\,\text{H}}}\right)\right)\right] \\ & + \frac{1-A_{\text{H}}}{1+R_{\text{L}}}\left[\frac{R_{\text{L}}}{2}\left(1-\text{erf}\left(\frac{\sigma_{1\,\text{L}}^2 - \log(x_{\text{cut}} - ((\mu_{\text{L}} - \Delta\mu_{\text{L}}) - 1))}{\sqrt{2}\sigma_{1\,\text{L}}}\right)\right)\right. \\ & \left. + \frac{1}{2}\left(1-\text{erf}\left(\frac{(\mu_{\text{L}} + \Delta\mu_{\text{L}}) - x_{\text{cut}}}{\sqrt{2}\sigma_{2\,\text{L}}}\right)\right)\right]\end{aligned} \tag{C.41}$$

Since the model has 11 free parameters, the resulting error propagation formula is:

$$\begin{aligned}\Delta\epsilon = {} & \left[\left(\frac{\partial\epsilon(x_{\text{cut}})}{\partial A_{\text{H}}}\Delta A_{\text{H}}\right)^2 + \left(\frac{\partial\epsilon(x_{\text{cut}})}{\partial R_{\text{H}}}\Delta R_{\text{H}}\right)^2 + \left(\frac{\partial\epsilon(x_{\text{cut}})}{\partial \mu_{\text{H}}}\Delta\mu_{\text{H}}\right)^2 + \left(\frac{\partial\epsilon(x_{\text{cut}})}{\partial \Delta\mu_{\text{H}}}\Delta\Delta\mu_{\text{H}}\right)^2\right. \\ & + \left(\frac{\partial\epsilon(x_{\text{cut}})}{\partial \sigma_{1\,\text{H}}}\Delta\sigma_{1\,\text{H}}\right)^2 + \left(\frac{\partial\epsilon(x_{\text{cut}})}{\partial \sigma_{2\,\text{H}}}\Delta\sigma_{2\,\text{H}}\right)^2 + \left(\frac{\partial\epsilon(x_{\text{cut}})}{\partial R_{\text{L}}}\Delta R_{\text{L}}\right)^2 + \left(\frac{\partial\epsilon(x_{\text{cut}})}{\partial \mu_{\text{L}}}\Delta\mu_{\text{L}}\right)^2 \\ & \left. + \left(\frac{\partial\epsilon(x_{\text{cut}})}{\partial \Delta\mu_{\text{L}}}\Delta\Delta\mu_{\text{L}}\right)^2 + \left(\frac{\partial\epsilon(x_{\text{cut}})}{\partial \sigma_{1\,\text{L}}}\Delta\sigma_{1\,\text{L}}\right)^2 + \left(\frac{\partial\epsilon(x_{\text{cut}})}{\partial \sigma_{2\,\text{L}}}\Delta\sigma_{2\,\text{L}}\right)^2\right]^{\frac{1}{2}}\end{aligned} \tag{C.42}$$

The terms needed for the error propagation formula are listed below:

$$\begin{aligned}\frac{\partial\epsilon(x_{\text{cut}})}{\partial\sigma_{1\,i}} = {} & -\frac{A_i R_i}{1+R_i}\frac{1}{\sqrt{2\pi}}\exp\left[-\frac{(\sigma_{1\,i}^2 - \log(x_{\text{cut}} - ((\mu_i - \Delta\mu_i) - 1)))^2}{2\sigma_{1\,i}^2}\right] \\ & \cdot\left(1 + \frac{\log(x_{\text{cut}} - ((\mu_i - \Delta\mu_i) - 1))}{\sigma_{1\,i}^2}\right)\end{aligned} \tag{C.43}$$

$$\frac{\partial\epsilon(x_{\text{cut}})}{\partial\sigma_{2\,i}} = \frac{A_i}{1+R_i}\frac{((\mu_i + \Delta\mu_i) - x_{\text{cut}})}{\sqrt{2\pi}\sigma_{2\,i}^2}\exp\left[-\frac{((\mu_i + \Delta\mu_i) - x_{\text{cut}})^2}{2\sigma_{2\,i}^2}\right] \tag{C.44}$$

$$\frac{\partial\epsilon(x_{\text{cut}})}{\partial A_{\text{H}}} = \frac{1}{1+R_{\text{H}}}\left[\frac{R_{\text{H}}}{2}\left(1-\text{erf}\left(\frac{\sigma_{1\,\text{H}}^2-\log(x_{\text{cut}}-((\mu_{\text{H}}-\Delta\mu_{\text{H}})-1))}{\sqrt{2}\sigma_{1\,\text{H}}}\right)\right)\right. \tag{C.45}$$
$$\left.+\frac{1}{2}\left(1-\text{erf}\left(\frac{(\mu_{\text{H}}+\Delta\mu_{\text{H}})-x_{\text{cut}}}{\sqrt{2}\sigma_{2\,\text{H}}}\right)\right)\right]$$
$$-\frac{1}{1+R_{\text{L}}}\left[\frac{R_{\text{L}}}{2}\left(1-\text{erf}\left(\frac{\sigma_{1\,\text{L}}^2-\log(x_{\text{cut}}-((\mu_{\text{L}}-\Delta\mu_{\text{L}})-1))}{\sqrt{2}\sigma_{1\,\text{L}}}\right)\right)\right.$$
$$\left.+\frac{1}{2}\left(1-\text{erf}\left(\frac{(\mu_{\text{L}}+\Delta\mu_{\text{L}})-x_{\text{cut}}}{\sqrt{2}\sigma_{2\,\text{L}}}\right)\right)\right]$$

$$\frac{\partial\epsilon(x_{\text{cut}})}{\partial R_{\text{i}}} = -\frac{A_i}{(1+R_i)^2}\left[\frac{R_i}{2}\left(1-\text{erf}\left(\frac{\sigma_{1\,i}^2-\log(x_{\text{cut}}-((\mu_i-\Delta\mu_i)-1))}{\sqrt{2}\sigma_{1\,i}}\right)\right)\right. \tag{C.46}$$
$$\left.+\frac{1}{2}\left(1-\text{erf}\left(\frac{(\mu_i+\Delta\mu_i)-x_{\text{cut}}}{\sqrt{2}\sigma_{2\,i}}\right)\right)\right]$$
$$+\frac{A_i}{1+R_i}\frac{1}{2}\left(1-\text{erf}\left(\frac{\sigma_{1\,i}^2-\log(x_{\text{cut}}-((\mu_i-\Delta\mu_i)-1))}{\sqrt{2}\sigma_{1\,i}}\right)\right)$$

$$\frac{\partial\epsilon(x_{\text{cut}})}{\partial\mu_i} = \frac{A_i}{1+R_i}\left[-\frac{R_i}{\sqrt{2\pi}\sigma_{1\,i}}\exp\left[-\frac{(\sigma_{1\,i}^2-\log(x_{\text{cut}}-((\mu_i-\Delta\mu_i)-1)))^2}{2\sigma_{1\,i}^2}\right]\right. \tag{C.47}$$
$$\left.\cdot\frac{1}{x_{\text{cut}}-((\mu_i-\Delta\mu_i)-1)}-\frac{1}{\sqrt{2\pi}\sigma_{2\,i}}\exp\left[-\frac{((\mu_i+\Delta\mu_i)-x_{\text{cut}})^2}{2\sigma_{2\,i}^2}\right]\right]$$

$$\frac{\partial\epsilon(x_{\text{cut}})}{\partial\Delta\mu_i} = \frac{A_i}{1+R_i}\left[\frac{R_i}{\sqrt{2\pi}\sigma_{1\,i}}\exp\left[-\frac{(\sigma_{1\,i}^2-\log(x_{\text{cut}}-((\mu_i-\Delta\mu_i)-1)))^2}{2\sigma_{1\,i}^2}\right]\right. \tag{C.48}$$
$$\left.\cdot\frac{1}{x_{\text{cut}}-((\mu_i-\Delta\mu_i)-1)}-\frac{1}{\sqrt{2\pi}\sigma_{2\,i}}\exp\left[-\frac{((\mu_i+\Delta\mu_i)-x_{\text{cut}})^2}{2\sigma_{2\,i}^2}\right]\right]$$

with $i \in \{\text{H},\text{L}\}$ and $A_{\text{L}} = 1 - A_{\text{H}}$. For the relation between $\sigma_{1,2}$ and the $FWHM_{1,2}$, the relation from the loggauss and gauss model can be used, respectively.

References

[1] C. E. Aalseth et al. "CoGeNT: A Search for Low-Mass Dark Matter using p-type Point Contact Germanium Detectors." In: *Phys. Rev. D* 88 (2013), p. 012002. arXiv: 1208.5737 [astro-ph.CO].

[2] M. Agostini et al. "Characterization of 30^{76}Ge enriched Broad Energy Ge detectors for GERDA Phase II." In: *Eur. Phys. J. C* 79.11 (2019), p. 978. arXiv: 1901.06590 [physics.ins-det].

[3] Q. R. Ahmad et al. "Direct evidence for neutrino flavor transformation from neutral current interactions in the Sudbury Neutrino Observatory." In: *Phys. Rev. Lett.* 89 (2002), p. 011301. arXiv: nucl-ex/0204008.

[4] D. Akimov et al. "Observation of Coherent Elastic Neutrino-Nucleus Scattering." In: *Science* 357.6356 (2017), pp. 1123–1126. arXiv: 1708.01294 [nucl-ex].

[5] D.Y. Akimov et al. "First ground-level laboratory test of the two-phase xenon emission detector RED-100." In: 15.02 (2020), P02020–P02020.

[6] P. S. Amanik and G. C. McLaughlin. "Nuclear neutron form factor from neutrino nucleus coherent elastic scattering." In: *J. Phys. G* 36 (2009), p. 015105.

[7] M. Sajjad Athar et al. "Status and Perspectives of Neutrino Physics." In: (2021). arXiv: 2111.07586 [hep-ph].

[8] P. S. Barbeau, J. I. Collar, and O. Tench. "Large-Mass Ultra-Low Noise Germanium Detectors: Performance and Applications in Neutrino and Astroparticle Physics." In: *JCAP* 09 (2007), p. 009. arXiv: nucl-ex/0701012.

[9] M.-M. Bé et al. *Table of Radionuclides*. Vol. 5. Monographie BIPM-5. Pavillon de Breteuil, F-92310 Sèvres, France: Bureau International des Poids et Mesures, 2010.

[10] M.-M. Bé et al. *Table of Radionuclides*. Vol. 7. Monographie BIPM-5. Pavillon de Breteuil, F-92310 Sèvres, France: Bureau International des Poids et Mesures, 2013.

[11] M.-M. Bé et al. *Table of Radionuclides*. Vol. 8. Monographie BIPM-5. Pavillon de Breteuil, F-92310 Sèvres, France: Bureau International des Poids et Mesures, 2016.

[12] A. G. Beda et al. "Gemma experiment: The results of neutrino magnetic moment search." In: *Phys. Part. Nucl. Lett.* 10 (2013), pp. 139–143.

[13] V. Belov et al. "The GeN experiment at the Kalinin Nuclear Power Plant." In: 10.12 (2015), P12011–P12011.

[14] M.J. Berger et al. *XCOM: Photon Cross Section Database (version 1.5)*. URL: http://physics.nist.gov/xcom (visited on 10/09/2021).

[15] J Billard et al. "Coherent neutrino scattering with low temperature bolometers at Chooz reactor complex." In: 44.10 (2017), p. 105101.

[16] J. Billard, E. Figueroa-Feliciano, and L. Strigari. "Implication of neutrino backgrounds on the reach of next generation dark matter direct detection experiments." In: *Physical Review D* 89.2 (2014).

[17] H. Bonet et al. "Constraints on Elastic Neutrino Nucleus Scattering in the Fully Coherent Regime from the CONUS Experiment." In: *Physical Review Letters* 126.4 (2021).

[18] H. Bonet et al. *Full Background Decomposition of the CONUS Experiment.* in preparation.

[19] H. Bonet et al. "Large-size sub-keV sensitive germanium detectors for the CONUS experiment." In: *The European Physical Journal C* 81.3 (2021).

[20] Aurélie Bonhomme. *Detecting CEνNS and searching for new physics at reactor site with the CONUS experiment.* Conference Talk at 17th International Conference on Topics in Astroparticle and Underground Physics, Online. 2021.

[21] Rene Brun and Fons Rademakers. "ROOT — An object oriented data analysis framework." In: *Nuclear Instruments and Methods in Physics Research Section A: Accelerators, Spectrometers, Detectors and Associated Equipment* 389.1 (1997). New Computing Techniques in Physics Research V, pp. 81–86.

[22] Dušan Budjáš. *Germanium detector studies in the framework of the GERDA experiment.* eng. 2009, Online–Ressource.

[23] Dušan Budjáš et al. "Pulse shape discrimination studies with a Broad-Energy Germanium detector for signal identification and background suppression in the GERDA double beta decay experiment." In: *Journal of Instrumentation* 4.10 (2009), P10007–P10007.

[24] CAEN. *CoMPASS - Multiparametric DAQ Software for Physics Applications.* URL: https://www.caen.it/products/compass/ (visited on 11/14/2021).

[25] CAEN. *V1725 - 16/8 Channel 14-bit 250 MS/s Digitizer.* URL: https://www.caen.it/products/v1725/ (visited on 11/04/2021).

[26] CAEN. *V1782 - Octal 32K Digital Multi Channel Analyzer.* URL: https://www.caen.it/products/v1782/ (visited on 11/04/2021).

[27] Jae Jin Choi. "Neutrino Elastic-scattering Observation with NaI[Tl](NEON)." In: *PoS* NuFact2019 (2020), p. 047.

[28] J. Colaresi et al. "First results from a search for coherent elastic neutrino-nucleus scattering at a reactor site." In: *Physical Review D* 104.7 (2021).

[29] CONNIE Collaboration et al. *The CONNIE experiment.* 2016. arXiv: 1608.01565 [physics.ins-det].

[30] CONUS Collaboration et al. *Novel constraints on neutrino physics beyond the standard model from the CONUS experiment.* 2021. arXiv: 2110.02174 [hep-ph].

[31] MINER Collaboration et al. *Background Studies for the MINER Coherent Neutrino Scattering Reactor Experiment*. 2016. arXiv: 1609.02066 [physics.ins-det].

[32] C. L. Cowan et al. "Detection of the free neutrino: A Confirmation." In: *Science* 124 (1956), pp. 103–104.

[33] K. Deergha Rao and M. N. S. Swamy. *Digital signal processing. theory and practice*. Singapore: Springer Nature, 2018, 1 Online–Ressource (xxiv, 789 Seiten).

[34] Daniel Z. Freedman. "Coherent effects of a weak neutral current." In: *Phys. Rev. D* 9 (5 1974), pp. 1389–1392.

[35] Y. Fukuda et al. "Evidence for oscillation of atmospheric neutrinos." In: *Phys. Rev. Lett.* 81 (1998), pp. 1562–1567. arXiv: hep-ex/9807003.

[36] Gordon Gilmore. *Practical gamma-ray spectrometry*. eng. 2. ed. Chichester [u.a.]: Wiley, 2008, XVIII, 387 S.

[37] Preussen Elektra GmbH. *Kernkraftwerk Brokdorf*. URL: https://www.preussenelektra.de/de/unsere-kraftwerke/kraftwerkbrokdorf.html (visited on 11/04/2021).

[38] J. Hakenmüller et al. "Neutron-induced background in the CONUS experiment." In: *The European Physical Journal C* 79.8 (2019).

[39] Janina Hakenmüller. *Looking for coherent elastic neutrino nucleus scattering with the CONUS experiment*. eng. Heidelberg, 2020, 1 Online–Ressource (250 Seiten).

[40] Zhong He. "Review of the Shockley–Ramo theorem and its application in semiconductor gamma-ray detectors." In: *Nuclear Instruments and Methods in Physics Research Section A: Accelerators, Spectrometers, Detectors and Associated Equipment* 463.1 (2001), pp. 250–267.

[41] Gerd Heusser et al. "GIOVE - A new detector setup for high sensitivity germanium spectroscopy at shallow depth." In: *Eur. Phys. J. C* 75.11 (2015), p. 531. arXiv: 1507.03319 [astro-ph.IM].

[42] Valentin T. Jordanov and Glenn F. Knoll. "Digital synthesis of pulse shapes in real time for high resolution radiation spectroscopy." In: *Nuclear Instruments and Methods in Physics Research Section A: Accelerators, Spectrometers, Detectors and Associated Equipment* 345.2 (1994), pp. 337–345.

[43] Wolfgang Kamke. *Der Umgang mit experimentellen Daten, insbesondere Fehleranalyse. im Physikalischen Anfänger-Praktikum*. ger. 10. Aachen: Shaker Verlag GmbH, 2014.

[44] T.S. Kosmas et al. "Sensitivities to neutrino electromagnetic properties at the TEXONO experiment." In: *Physics Letters B* 750 (2015), pp. 459–465.

[45] Manfred Lindner, Werner Rodejohann, and Xun-Jie Xu. "Coherent Neutrino-Nucleus Scattering and new Neutrino Interactions." In: *JHEP* 03 (2017), p. 097. arXiv: 1612.04150 [hep-ph].

[46] P. N. Luke et al. In: *IEEE Trans. Nucl. Sci.* 36 (1989), p. 926.

[47] Donald B. Owen. “Tables for Computing Bivariate Normal Probabilities.” In: *The Annals of Mathematical Statistics* 27.4 (1956), pp. 1075–1090.

[48] W. Pauli. “Dear radioactive ladies and gentlemen.” In: *Phys. Today* 31N9 (1978), p. 27.

[49] Tobias Schierhuber. *Ultra-Low Background Germanium Spectroscopy: Commissioning an experimental shielding for a future neutrino experiment*. eng. Heidelberg, 2017.

[50] A. K. Soma et al. “Characterization and Performance of Germanium Detectors with sub-keV Sensitivities for Neutrino and Dark Matter Experiments.” In: *Nucl. Instrum. Meth. A* 836 (2016), pp. 67–82. arXiv: 1411.4802 [physics.ins-det].

[51] R. Strauss et al. “The ν-cleus experiment: a gram-scale fiducial-volume cryogenic detector for the first detection of coherent neutrino–nucleus scattering.” In: *The European Physical Journal C* 77.8 (2017).

[52] Tektronix. *Arbitrary/Function Generator AFG3000 Series*. URL: https://www.tek.com/datasheet/afg3000-series (visited on 11/02/2021).

[53] Mark Thomson. *Modern Particle Physics*. Cambridge University Press, 2013.

[54] H. T. Wong. “The TEXONO research program on neutrino and astroparticle physics.” In: *Mod. Phys. Lett. A* 19 (2004). Ed. by W. Y. Pauchy Hwang, Guey-Lin Lin, and J. H. P. Wu, pp. 1207–1214.

[55] L. T. Yang et al. “Bulk and Surface Event Identification in p-type Germanium Detectors.” In: *Nucl. Instrum. Meth. A* 886 (2018), pp. 13–23. arXiv: 1611.03357 [physics.ins-det].

[56] Eberhard Zeidler. *Springer-Taschenbuch der Mathematik. Begründet von I.N. Bronstein und K.A. Semendjaew Weitergeführt von G. Grosche, V. Ziegler und D. Ziegler Herausgegeben von E. Zeidler*. ger. 3., neu bearb. und erw. Aufl. 2013. Springer eBook Collection. Wiesbaden: Springer Vieweg, 2013, Online–Ressource (XX, 1310 S. 200 Abb, digital).

[57] P.A. Zyla et al. “Review of Particle Physics.” In: *PTEP* 2020.8 (2020), p. 083C01.

List of Figures

List of Tables

Acknowledgements

I would like to thank my supervisor, Prof. Dr. Dr. h.c. Manfred Lindner for the possibility of doing my thesis in his division and contributing to the CONUS experiment. Further, I would like to express gratitude to my co-supervisor, Dr. Aurélie Bonhomme for all the helpful discussions and her support. Additionally, I am grateful for the productive discussions with the members of the CONUS Collaboration and for the great company at the institute and during the shifts at the experiment. Special thanks go to Sarah Schuhegger, Dr. Werner Maneschg, Dr. Aurélie Bonhomme and Dr. Janina Hackenmüller for proof-reading. Finally, I want to thank my family for always supporting me.

Declaration of Authorship

I hereby certify that this thesis has been composed by me and is based on my own work, unless stated otherwise.

Ich versichere, dass ich diese Arbeit selbstständig verfasst habe und keine anderen als die angegebenen Quellen und Hilfsmittel benutzt habe.

Heidelberg, 15.12.2021 J. Heinrichs